

DISSERTATION

EXOTIC PHENOMENA IN RARE-EARTH BASED GEOMETRICALLY FRUSTRATED MAGNETS

Submitted by

Danielle Rose Yahne

Department of Physics

In partial fulfillment of the requirements

For the Degree of Doctor of Philosophy

Colorado State University

Fort Collins, Colorado

Spring 2022

Doctoral Committee:

Advisor: Kate A. Ross

Mark Bradley

Kristen Buchanan

Joe Zadrozny

Copyright by Danielle R. Yahne 2022

All Rights Reserved

ABSTRACT

EXOTIC PHENOMENA IN RARE-EARTH BASED GEOMETRICALLY FRUSTRATED MAGNETS

Rare-earth (RE) based frustrated magnets are ideal systems to explore quantum effects in materials, which are paramount for the development of quantum computers, MRAM, and other next-generation technology. RE based materials are of specific interest due to the strong spin-orbit coupling and crystal electric field effects, which split the degenerate $4f$ angular momentum states, often leading to an effective spin-1/2 doublet with anisotropic effective exchange models. For this reason, RE materials are paramount to investigating the effects of anisotropic exchange on exotic ground states or quantum phases. Exchange frustration refers to when a system cannot simultaneously satisfy competing interactions, which can lead to a macroscopic degeneracy in the ground state of the system. Materials with *geometric* frustration, where competing interactions occur due to the crystal geometry alone, have been shown to host a wealth of exotic phenomena, including spin ice phases, quasi-particle excitations, order-by-disorder, and the highly entangled quantum spin liquid (QSL) state, to name a few.

In this thesis, we will discuss three RE systems that exhibit geometric frustration in addition to exchange frustration: two RE pyrochlore oxides ($\text{RE}_2\text{TM}_2\text{O}_7$) and a 2D isosceles triangular lattice material $\text{K}_3\text{Er}(\text{VO}_4)_2$. Spin-1/2 antiferromagnetic (AFM) 2D triangular lattice magnets are an archetype of geometric frustration. While these materials are theorized to host a variety of different ground states and exotic phases depending on the anisotropies of the system, only a handful of RE material examples have been explored. We report the first deep dive into one such system, $\text{K}_3\text{Er}(\text{VO}_4)_2$. We have determined the ordered magnetic structure of $\text{K}_3\text{Er}(\text{VO}_4)_2$, finding an unusual structure with alternating layers comprised of AFM aligned and zero moment. We theorize this unique structure is due to the strong XY single-ion anisotropy, suggested from magnetometry measurements, which acts to suppress (to the point of vanishing completely) the out-of-plane pseudo-spin-1/2 magnetic moments.

Next, we explored the effects of phase competition in a well-studied effective spin-1/2 RE pyrochlore oxide, $\text{Er}_2\text{Sn}_2\text{O}_7$. Previous polycrystalline work has found $\text{Er}_2\text{Sn}_2\text{O}_7$ to possess a suppressed critical temperature and an AFM Palmer-Chalker ground state. The determined exchange and single-ion anisotropy of $\text{Er}_2\text{Sn}_2\text{O}_7$ find the ground state lies in close proximity to a competing AFM phase. Through extensive single crystal heat capacity measurements, we discovered a reentrant field vs. temperature phase diagram, where a system that has developed order returns to the original, less ordered (paramagnetic) state as some external parameter (field) is tuned continuously. We investigated the underlying mechanisms behind the reentrance by utilizing Monte Carlo simulations, mean field theory, and classical linear spin-wave calculations. This theory suggests that reentrance is linked to soft modes arising from phase competition, either from enhanced competition of the proximal AFM phase or from competing $T = 0$ field-evolved ground states, depending on the specific applied field direction. In both cases, the soft modes enhance thermal fluctuations which cause the specific ordered phase to be entropically stabilized, thus forming a reentrant phase diagram.

Finally, we report recent elastic neutron diffraction results on a RE pyrochlore oxide and candidate octupolar spin-ice, $\text{Ce}_2\text{Sn}_2\text{O}_7$. The pseudo-spin-1/2 moments in $\text{Ce}_2\text{Sn}_2\text{O}_7$ are known to possess dipolar-octupolar character and a large parameter space within the phase diagram is theorized to host novel QSL states. Previous powder neutron diffraction found diffuse scattering at high scattering vectors associated with magnetic octupoles. However, our undertaking of a similar measurement on nominally the same sample, found strikingly different results. Our neutron diffraction resulted in a broad, diffuse signal at low scattering vectors, reminiscent of a *dipolar* spin-ice. Neutron diffraction and atomic PDF measurements have not turned up obvious sample deformities or evidence of oxidation that could explain the differences in the diffuse signals. Further atomic studies and significant theory work is necessary to fully understand the results of this measurements, but the similarities to sister compound $\text{Ce}_2\text{Zr}_2\text{O}_7$ suggest that $\text{Ce}_2\text{Sn}_2\text{O}_7$ could lie on a phase boundary that is sensitive to minor distortions.

ACKNOWLEDGEMENTS

I have been blessed to have the greatest support network I could have asked for during my graduate career. First and foremost, I would like to thank my advisor, Kate Ross. I am constantly in awe of your brilliance and humility, and your encouragement and support has helped me blossom into a strong, independent, powerful woman scientist. I appreciate our open and honest conversations about, well, everything! Thank you for believing in me, it has been a privilege working with you. I would also like to thank my SCGSR mentor Stuart Calder for taking me under your wing, imparting your neutron diffraction knowledge on me, and encouraging me to try new experiments. Additionally, I would like to acknowledge the CSU Physics Department and support staff for creating a warm, encouraging, and inclusive environment for us to thrive in.

This work would not be possible without the support of all of Ross Lab, specifically Gavin Hester, Colin Sarkis, Steffen Säubert, Andrew Treglia, John Ringler, Daniel Shaw, Theo Wecker, and Tim DeLazzer. I am grateful to have gotten to work with great people as well as great scientists. I was never short of volunteers when I needed help with something, and my presentations were perfected from all of our practices and the constructive criticism you all gave. I would like to especially thank three of my closest coworkers and friends, Gavin, Colin, and Steffen. Colin, aka Chamsy, I am grateful for our friendship and the countless board game nights that kept me sane. Steffen, our coffee walk breaks were always what I needed, and surprisingly essential to figuring out research problems. I appreciate the nights watching trash TV, and cannot wait to see you and Suzan in Munich. Gavin, aka Gravel and co-creator of the board of shame, thank you for being my best bud, believing in and encouraging me, and bringing Nycole into my life. You continue to inspire me as a scientist and I look forward to our future collaborations.

On a personal note, I would like to thank my loved ones for all of their support. First and foremost, to my husband Kevin, thank you for being my biggest cheerleader, and supporting me as I moved us across the country to follow my passion for physics. Even when you had no

idea what I was talking about, you never listened any less intently as I repeated to you all of the questions on the test that I took and exactly how I answered them. Thank you for riding this insane roller-coaster with me. Next, to my mom, thank you for always giving me a role model of a resilient, brilliant woman and supporting my goals. I appreciate all the calls you've taken to help me with adulting, and encouraging me when I'm at my lowest. Finally, thank you to the rest of my family, Mike, Adam, Oma & Opa, Deb (we miss you every day), Grandma & Grandpa Kidder, Bethany & Trevor, Janelle, Amanda, and Beth, for being there for us (and visiting!) during this journey. Also, I want to thank my LimeLight family for keeping me sane, and Christina for helping me become a warrior and push through the hard times. I love you all!

DEDICATION

I would like to dedicate this dissertation to my husband, Kevin, and my family who supported and encouraged me throughout my entire physics career.

“You don’t have to be perfect to make important contributions.” - K. A. Ross

TABLE OF CONTENTS

ABSTRACT	ii
ACKNOWLEDGEMENTS	iv
DEDICATION	vi
LIST OF TABLES	viii
LIST OF FIGURES	ix
Chapter 1	Introduction 1
1.1	Rare-earth Magnetism 1
1.1.1	Magnetic interactions 1
1.1.2	Frustrated magnets 3
1.1.3	Spin-orbit coupling and crystal field effects 5
1.1.4	Rare-earth pyrochlore oxides, $A_2B_2O_7$ 8
1.1.5	Rare-earth triangular lattice materials 18
1.2	Experimental Techniques 21
1.2.1	Heat capacity 21
1.2.2	Magnetometry 28
1.2.3	Neutron scattering 32
1.3	Theoretical Techniques 45
1.3.1	Describing Magnetic Structures 45
Chapter 2	Pseudo-spin versus magnetic dipole moment ordering in the isosceles triangular lattice material $K_3Er(VO_4)_2$ 51
2.1	Context 51
2.2	Paper abstract 52
2.3	Research article 53
2.4	Supplemental material 64
2.5	Ongoing work 69
Chapter 3	Understanding reentrance in frustrated magnets: the case of the $Er_2Sn_2O_7$ pyrochlore 75
3.1	Context 75
3.2	Paper abstract 76
3.3	Research article 76
3.4	Supplemental material 86
3.5	Ongoing work 104
Chapter 4	Dipolar correlations found in candidate octupolar spin ice $Ce_2Sn_2O_7$ 108
4.1	Context 108
4.2	Research Article 109
4.3	Supplemental Material 116
Chapter 5	Conclusion 117

LIST OF TABLES

1.1	Properties of well-known XY pyrochlores in comparison to $\text{Er}_2\text{Sn}_2\text{O}_7$ showing the strong XY single-ion nature as well as the suppressed transition temperature.	14
1.2	The three irreducible representations of the permutation group $P(3)$. Γ_1 is the trivial group, and it is from these irreps that all reducible representations of $P(3)$ are composed of.	47
2.1	Irreducible representation and basis vector composition for space group $C2/c$ with $\mathbf{k}=(1,0,0)$ found using the SARA h Representational Analysis software. The atoms are defined according to $\mathbf{m}_1: (0.5, 0, 0.5)$ and $\mathbf{m}_2:(0.5, 0, 0)$	59
2.2	Crystallographic data of $\text{K}_3\text{Er}(\text{VO}_4)_2$ determined by single crystal X-ray diffraction.	64
3.1	Spin configurations for three of the six Palmer-Chalker states on the four sublattices $i = 0, 1, 2, 3$ of a tetrahedron. Each state lies within a plane in the global frame of reference (e.g. $\langle xy \rangle$ lies in the xy -plane). The remaining three Palmer-Chalker states are obtained by spin reversal. The convention for labeling the sublattices follows the one from Ref. [1].	86
4.1	Refined room temperature parameters for $\text{Ce}_2\text{Sn}_2\text{O}_7$ from neutron diffraction on HB-2A using the Fullprof Rietveld refinement.	116

LIST OF FIGURES

1.1	a) Canonical example of magnetic frustration, with AFM interacting Ising spins on a triangular lattice. Depending on the top spin direction, either the left or right interaction cannot be satisfied. b) The tetrahedron, a 3D analogue of the triangular lattice frustration. Schematics of various geometrically frustrated lattices: c) triangular lattice composed of edge sharing triangles, d) kagome lattice composed of corner sharing triangles, e) pyrochlore lattice composed of corner sharing tetrahedra, f) perovskite lattice composed of edge sharing tetrahedra.	5
1.2	The pyrochlore structure showing corner-sharing tetrahedra on both the a) <i>A</i> -site and the b) <i>B</i> -site, which interpenetrate each other. c) The oxygen cage surrounding a single <i>A</i> -site ion. The difference in <i>A-O'</i> and <i>A-O</i> is responsible for the single-ion anisotropy.	8
1.3	a) The sites of a single tetrahedron in the pyrochlore lattice. The bond-dependent interactions between magnetic ions are given by Eqn. (1.12). b) The local [111] axis, equivalent to the C_3 symmetry axis, is shown for two corner sharing tetrahedra on the pyrochlore lattice. c) All-in-all-out (AIAO) ordered magnetic structure. d) One possible spin-ice configuration on the pyrochlore lattice, which follows the ice-rule that two spins point into and two spins point out of the center of the tetrahedra.	11
1.4	Classical ground state phase diagram for effective spin-1/2 pyrochlores with $J_4 = 0$ and $J_3 < 0$. The spin configurations for each phase is shown, and various studied materials are also placed in the respective phases. Note: $\text{Yb}_2\text{Ge}_2\text{O}_7$ does <i>not</i> have a J_4 equal to zero, therefore the placement on the phase diagram is for qualitative purposes. Figure adapted from Refs. [1] and [2].	15
1.5	a) Visualization of the dipolar/octupolar nature of the DO pyrochlores, where the <i>x</i> and <i>z</i> components of the pseudo-spin transform as components of the magnetic dipole and the <i>y</i> component transforms as a component of the magnetic octupole. Image credit: Ref. [3]. b) The ground state phase diagram for DO pyrochlores using the XYZ model, parameterized such that $\tilde{J}_x = J \cos(\phi) \sin(\psi)$, $\tilde{J}_y = J \sin(\phi) \sin(\psi)$, and $\tilde{J}_z = J \cos(\psi)$, where <i>J</i> is an overall scale factor. Two ordered phases and four QSL phases are found within this phase diagram, with ~ 20% of the phase space corresponding to the QSL phase. Figure adapted from Ref. [4].	17
1.6	Schematics of a) 120° magnetic order, b) quantum spin liquid with fluid valence bonds (spin pairs), and c) stripe order on a 2D edge-sharing triangular lattice.	19
1.7	Illustrative graphical representations of the free energy, <i>F</i> , entropy, <i>S</i> , and heat capacity, <i>C</i> , for first and second order transitions near the critical temperature, T_c	24

1.8	Temperature with respect to time after a heat pulse during a (a) short pulse and (b) long pulse measurement. The heating and cooling parts of the measurements are shown with red and blue respectively. The jump between heating and cooling in the (a) short pulse measurement due to a τ_2 contribution is circled. (c) The extracted short pulse heat capacity with the specific fitted data point associated with the heat pulse in (a) highlighted in red. (d) The heat capacity extracted from a long pulse measurement, showing the continuous nature due to using the entire cooling curve. (e) The Quantum Design dilution refrigerator probe. Image credit: Ref. [5] (f) A crystal mounted on the sapphire sample stage which is suspended in vacuum.	27
1.9	Figure adapted from Ref. [6] showing the expected magnetic susceptibility signatures for a paramagnetic, ferromagnetic, and antiferromagnetic material. As temperature is decreased, the moments will align (or anti-align) more readily and follow a $1/T$ dependence. Magnetic order then breaks this trend and either saturates (ferromagnet) or decreases toward zero (antiferromagnet).	29
1.10	Schematic of the MPMS showing the sample moves through the pickup (detection) coils, creating a voltage signal that is amplified using a SQUID. Figure from Ref. [7].	32
1.11	a) Neutron scattering set-up. The incoming beam of neutrons has initial energy E_i and wavevector \mathbf{k}_i before interacting with sample. After interaction, the scattered neutron has energy E_f and wavevector \mathbf{k}_f , and is scattered into area $d\omega$ at an angle of 2θ . b) Coherent scattering length, b , as a function of atomic number, Z . The non-monotonic nature of the coherent scattering length allows for the study of light elements and discerning different isotopes of the same material not possible with x-ray scattering. Data extracted from Ref. [8].	34
1.12	Schematics of a) a triple axis and b) diffraction beamlines at a reactor source. In both cases, the neutron interacts with a monochromator crystal to pick out the incident energy before it interacts with the sample. The scattered neutron is then energy discriminated with an analyzer crystal before being detected in a triple axis experiment, while it is energy integrated when detected in a diffraction experiment. Both types of beamlines utilize either ^3He point detectors or 2D position sensitive detectors.	39
1.13	a) Simplified inelastic neutron scattering graphic which shows that a positive energy transfer corresponds to the neutron losing energy. b) The multi-blade design of a neutron velocity selector. Image credit: Ref. [9] c) A disk chopper from DCS at NIST, where the white is Gd_2O_3 , a strong neutron absorber. Image credit: nist.gov. d) A schematic of a Fermi chopper. Image adapted from Ref. [10].	41
1.14	A a) random and b) locally ordered system of vacancies. c) The corresponding powder diffraction pattern, which shows that the Bragg scattering is the same from a) and b), but the local order has diffuse scattering in addition. c) The PDF of both systems, where the locally ordered system has greater intensity on the nearest-neighbor bond distance peak. Image credit: Ref. [11]	43
1.15	Isomorphic groups: the permutation group, $P(3)$, which is a permutation of three numbers, and the symmetry group, D_3 , for an equilateral triangle.	47

2.1	a) Crystal structure of monoclinic $\text{K}_3\text{Er}(\text{VO}_4)_2$ (space group $C2/c$) showing layers of 2D isosceles triangular Er^{3+} lattices. b) The 2D isosceles triangular Er^{3+} lattice, with bond lengths and unit cell size shown (not shown, $c = 15.2050 \text{ \AA}$). c) Typical single crystals of $\text{K}_3\text{Er}(\text{VO}_4)_2$ which were co-aligned for magnetization and susceptibility measurements.	53
2.2	Single crystal heat capacity in zero magnetic field. The open circles represent the adiabatic measurements, while the solid line represents the large ΔT measurements. A sharp magnetic transition is observed at 155 mK, with the asymmetric shape on the high temperature side of the transition indicating a build-up of low dimensional short range correlations. (Inset) Entropy calculated from C_p vs. T with the $R \ln 2$ limit shown, indicating an isolated $S_{\text{eff}} = \frac{1}{2}$ system below 1 K.	57
2.3	a) Magnetic susceptibility of co-aligned single crystals with the field aligned perpendicular and parallel to the c -axis, showing $\chi_{\perp c}$ is larger than $\chi_{\parallel c}$ by a factor of ~ 10 . (Inset) Low temperature fit of inverse susceptibility used to find the $H \perp c$ Curie-Weiss temperature $\theta_{CW} \approx -3 \text{ K}$. b) Magnetization of co-aligned single crystals at 1.8 K. For $H \parallel c$, significant field-induced mixing of the next highest CEF level produces an enhanced moment in the field.	58
2.4	Visualizations of the basis vectors for space group $C2/c$ with $\mathbf{k}=(1,0,0)$: $\psi_{1,2,3}$ from Γ_1 and $\psi_{4,5,6}$ from Γ_3 . All basis vectors are antiferromagnetic in the ab -plane. Basis vectors $\psi_{1,3,5}$ are also antiferromagnetic along c , while basis vectors $\psi_{2,4,6}$ are ferromagnetic along c (each layer is identical).	60
2.5	a) Neutron diffraction pattern (black) taken on a 2.5 g powder sample on beamline HB-2A at HFIR (ORNL). Magnetic peaks were found from subtracting the 400 mK pattern from the 50 mK pattern to remove impurity signals. A coexistence of 2D and 3D order was found, and thus the Warren-like (100) peak was not included in the fit. The fit to the 3D order (red) and calculated difference (blue) is shown for the best fit using the Fullprof software, which was a linear combination of equal contributions of basis vectors ψ_2 (from Γ_1) and ψ_5 (from Γ_3). b) Temperature dependence of magnetic Bragg peaks below the transition temperature of 155 mK shows the onset of 2D and 3D order occurs at the same temperature. Magnetic impurity peaks were found between 10 K and 400 mK, denoted with a star. c) The magnetic structure found from neutron diffraction pattern shows layers of b -aligned moment alternating with layers of zero moment, proposed to be due to the strong XY nature of $\text{K}_3\text{Er}(\text{VO}_4)_2$ ($g_z \sim 0$). d) The proposed <i>pseudo-spin</i> structure, alternating between layers of b -aligned pseudo-spin and layers of c -aligned pseudo-spin.	61
2.6	Nuclear structure of $\text{K}_3\text{Er}(\text{VO}_4)_2$ found with neutron scattering at 10 K. The trigonal structure clearly does not describe the crystal structure in contrast to the monoclinic structure. The impurity is also seen in small peaks unable to be fit by either structure, denoted by stars.	66
2.7	a) Warren fit and quasi-Warren simulation compared with the 50 mK data (not background subtracted). The (hkl) and nuclear peaks were masked (grey boxes). The Warren fit overestimates the high-Q side of the asymmetric peak. b) Residual plot for varying combinations of correlation lengths along the ab and c directions. c) 2D visualization of simulation in the $h0l$ plane, where blue ellipses are the scattering intensities and the red circles are the integrated areas simulating the powder diffraction.	66

2.8	Examples of fits using a single irreducible representation. Both Γ_1 and Γ_3 fits give peaks not seen in the data, shown by arrows. Therefore, the best fit comes from a linear combination of Γ_1 and Γ_3 's basis vectors, ψ_2 and ψ_5 respectively.	68
2.9	Total moment as a function of temperature. Red line serves as an order parameter guide to the eye, note this is not a fit.	69
2.10	Crystal orientation for rotation magnetization measurements using a) a thin film mount to probe the magnetization within the ab-plane and b) a standard mount to probe the ac-plane. c) Rotation magnetization results, including a guide-to-the-eye for the ab-plane results due to a signal of unknown origin. We have also included the saturation magnetization values at 5 T found previously (Figure 2.3 b).	71
2.11	a) Powder neutron spectrum with an incident energy of 20 meV at 5 K. Crystal field excitations are clearly visible, including a low-lying level near 1.5 meV. b) Temperature dependent cut of INS data, with integration range shown in a) by the red box. c) Powder neutron spectrum with an incident energy of 80 meV at 5 K. No CEF transitions in the 40 meV range are seen. d) Temperature dependent cut of INS data, with integration range shown in c).	73
2.12	Energy vs. intensity cuts from a) 20 meV and b) 50 meV incident energy measurements. The red line indicates the CEF fit with the trigonal simplification. c) The difference in the oxygen cage around the Er^{3+} ion in the monoclinic and trigonal space groups that motivates the point group simplification.	74
3.1	Example of sixfold degenerate states: (a) Palmer-Chalker [12] and (b) ψ_2 and (c) ψ_3 basis states of Γ_5 [13]. The ψ_2 and ψ_3 states are connected by a rotation of the spins by an angle ϕ within their local easy planes (yellow circles): $\phi \equiv n\pi/3$ ($+\pi/6$) for $n = 0, \dots, 5$ correspond to ψ_2 (ψ_3) [14]. Panels (b) and (c) are for $\phi = 0$ and $\pi/2$, respectively. The manifold with $U(1)$ degeneracy, $\phi \in [0, 2\pi]$, forms the so-called Γ_5 states that appear in the [111] phase diagram. (d) Heat capacity, $C_p(T)$, vs temperature, T , of $\text{Er}_2\text{Sn}_2\text{O}_7$ with the magnetic field along [100], showing the reentrant nature of the transition. Curves at different fields are offset vertically for clarity. Similar data for the [110] and [111] field directions are included in the Appendix. (Inset) $C_p(T)$ $\text{Er}_2\text{Sn}_2\text{O}_7$ in zero field, with short and long pulse measurements on crystal samples overlaid. Powder data from Shirai <i>et al.</i> [15] is also overlaid to demonstrate agreement between sample types.	79
3.2	B - T phase diagrams of $\text{Er}_2\text{Sn}_2\text{O}_7$ in the (a) [100], (b) [110] and (c) [111] field directions, comparing experimental data with sharp (\square) and smooth (\blacksquare) heat-capacity peaks [Fig. 3.1(d)], to Monte Carlo results with first (\square) and second (\blacksquare) order transitions. Experiments and simulations are notably similar, showing the same (multiple) reentrance. The degeneracy Z_n found in simulations is given for each phase. The width of the red rectangles at 0 and 0.1 T represents the position of the double peaks. (d) In a [111] field, each of the six FEPC ground states has a Γ_5 contribution described by an angle ϕ [Figs. 3.1(b) and 3.1(c)], that can be computed exactly by minimizing the energy of one tetrahedron as a function of B	81

3.3	Classical spin-wave dispersions for $B = 0, 0.40, 0.82$, and 1.20 T along the $[100]$ direction, for a path in the FCC Brillouin zone. Note that $B_c = 0.82$ T is a critical field at $T = 0$, as shown in Fig. 3.2. The grey boxes indicate energy scales below $T_c(B = 0 \text{ T}) \approx 160$ mK from Monte Carlo simulations; when modes occur within this region they are considered “soft”. Note that the dispersions for <i>all</i> Palmer-Chalker states are plotted, but may overlap at high-symmetry points or due to their degeneracies in a field.	83
3.4	The six Palmer-Chalker states, labeled from left to right $\langle xz \rangle$, $\langle yz \rangle$, $\langle xy \rangle$ (first row) and $\langle \bar{x}\bar{z} \rangle$, $\langle \bar{y}\bar{z} \rangle$, $\langle \bar{x}\bar{y} \rangle$ (second row).	86
3.5	Raw zero field heat capacity data for the three crystals polished in each of the high symmetry directions. We find that all samples show a low temperature shoulder, but the pronouncement of the shoulder varies between samples. (Inset) Example of a typical crystal that was used in heat capacity measurements.	87
3.6	Raw long pulse heat capacity data for fields along the three cubic high symmetry directions, leading to the phase diagram shown in the main text. Note, all data at nonzero field have been shifted vertically for clarity.	87
3.7	(a) Elastic neutron scattering data (black) on SPINS. Data was taken at 50 mK, 110 mK, and 8 K, with 8 K data used for background subtraction. The fit to the PC phase is shown (red), as well as the difference between the data and fit (blue). (b) Calculated magnetic diffraction patterns for the Γ_5 and PC (Γ_7) configurations (nuclear contributions not shown). The Γ_5 pattern has been shifted vertically for clarity. . . .	88
3.8	Zero temperature representations of field-evolved Palmer-Chalker (FEPC) mergers ((a), (c), and (e)) and mean field B - T phase diagrams ((b), (d), and (f)) for the $[100]$, $[111]$, and $[110]$ field directions, respectively. In the FEPC merger diagrams, vertical grey lines represent critical fields of the merging transitions; the vertical blue line represents field-induced selection of the ψ_2 phase out of the accidentally-degenerate Γ_5 manifold; vertical red lines represent changes in the set of degenerate FEPC states. Solid lines denote the FEPC states that are degenerate and minimize the energy; dotted lines represent FEPC states that are excited and do not minimize the energy. In the mean field phase diagrams, filled black squares represent a phase transition to a phase of different discrete symmetry due to merging; open red squares represent a change in the set of degenerate FEPC states. In both sets of diagrams, \mathbb{Z}_n denotes the discrete symmetry of the phase, which has n distinct spin configurations out of the degenerate FEPC states. FP-PM denotes the field-polarized paramagnetic phase; PC denotes Palmer-Chalker order. Note that the zero temperature phases in the $[110]$ field direction differ from the finite temperature phases due to entropic effects, for reasons discussed further in Section 3.4. Note also that \mathbb{Z}_n labels for the mean-field phase diagrams may differ from those of the Monte Carlo phase diagrams shown in Fig. 2 of the main text due to thermal order-by-disorder selection (e.g. the low-field \mathbb{Z}_6 region of the mean-field $[100]$ phase diagram, versus the low-field \mathbb{Z}_4 region of the Monte Carlo $[100]$ phase diagram).	93

3.9	Classical spin-wave dispersions for all Palmer-Chalker states that are degenerate in their energy, for a given field direction and magnitude. The shaded grey box represents energy scales below the zero-field Monte Carlo critical temperature of $T_c \approx 160$ mK. The chosen wavevectors are taken from the Brillouin zone of the FCC lattice. Note that some curves may overlap at high-symmetry points or due to their degeneracies in a field (e.g. $\langle xy \rangle_h$ and $\langle \bar{x}\bar{y} \rangle_h$ for $B \geq 0.82$ T along the [100] direction).	97
3.10	Diagram denoting the discrete symmetry of each phase as a function of field H and temperature T within mean field theory, for the [110] field direction. Note that the free energies of each FEPC state is not considered here. Hence this is not a true phase diagram but merely represents the degeneracy and merging of FEPC spin configurations.	101
3.11	Differentiation between the ground and excited states in Monte Carlo simulations via the z -component of the Palmer-Chalker order parameter, m_{PCz} (a,b,c). m_{PCz} is finite for the two excited states, while it is zero for the four ground states. Here we show that as the system size is increased, m_{PCz} vanishes for $B = 0.1$ and 0.15 T, which means the FEPC excited states are not stable for $B \gtrsim 0.1$ T. For $B = 0.05$ T on the other hand, simulations are difficult to thermalize and the evolution with system size is not monotonic. As for the four FEPC ground states, they can be divided into two pairs. For $\langle \bar{x}\bar{z} \rangle_h$ and $\langle \bar{y}\bar{z} \rangle_h$, the x -component of the Palmer-Chalker order parameter is positive, $m_{PCx} > 0$. For $\langle xz \rangle_h$ and $\langle yz \rangle_h$, $m_{PCx} < 0$. As shown in panels (d,e,f), m_{PCx} always gets more positive for large system sizes, which means that the Z_2 states at low [110] field are $\langle \bar{x}\bar{z} \rangle_h$ and $\langle \bar{y}\bar{z} \rangle_h$. At very low temperatures, $T < 40$ mK, the data split into two groups because of the broken ergodicity in simulations between $\langle \bar{x}\bar{z} \rangle_h$ and $\langle \bar{y}\bar{z} \rangle_h$. All of these simulations were done for $t_m = 5 \cdot 10^7$ Monte-Carlo steps.	102
3.12	Here we reproduce the phase diagrams in a [111] field as signalled via the (a) Palmer-Chalker and (b) Γ_5 order parameters, as well as the quantity (c) $m_{6\phi}$ (defined above) to differentiate between ψ_2 and ψ_3 states.	103
3.13	Spin-wave scattering of $\text{Er}_2\text{Sn}_2\text{O}_7$ in the field polarized state with an applied field of 3 T (7 T background subtracted) and $T \approx 0.05$ K in the a) HH0 and b) HH $\bar{1}$ planes. Incident energy was 2 meV and the calculated spin-wave dispersions using the parameters from Ref. [16]. c) Co-aligned single crystals used for this study, with a total mass around 50 mg.	106
3.14	Field dependent energy vs. intensity cuts around the [002] zone centers, 5 T background subtracted. a) Cut along $[0, 0, 2 \pm 0.2]$ and b) $[0 \pm 0.2, 0 \pm 0.2, 2]$ showing the spin wave softens above 0.5 T. The elastic line (not background subtracted) at c) 0.5 T and d) 0.65 T shows an intervening $(\frac{1}{2} \frac{1}{2} \frac{1}{2})$ phase.	107
4.1	a) PDF analysis of $\text{Ce}_2\text{Sn}_2\text{O}_7$ from total neutron scattering data taken on the NOMAD beamline at room temperature. The Fourier transform and background subtraction was performed using the PDFgetN3 program, and Rietveld refinement utilized the PDFgui software. The fitted curve (red) shows good agreement with the data, indicating no local distortions in the sample. The slight disagreement at small neighbor distances is due to the asymmetric peak shape on NOMAD [17]. b) Room temperature powder neutron diffraction on beamline HB-2A, and refined parameters can be found in Table 4.1.	111

4.2	a) Single crystal heat capacity compared to previously published polycrystalline data by Ref. [18]. Power law extrapolations down to 0 K were utilized to achieve a reasonable estimate of the entropy. Please note that the data presented here is the total heat capacity (not lattice subtracted), while the Sibille <i>et. al</i> data is C_{mag} , however, the phonon contribution at low temperature is expected to be quite low and thus should not affect the conclusions of this work. b) The entropy recovered over the full temperature range, showing our work plateaus at $R\ln(2)$, expected for a well-isolated single-ion doublet. The Pauling spin ice entropy is also shown.	113
4.3	a) Diffuse neutron scattering from data taken on WAND ² at 300 mK. All data has been converted to absolute units, and high temperature data was used for background subtraction. We compare the $\text{Ce}_2\text{Sn}_2\text{O}_7$ diffuse scattering to that of known dipolar spin ice material $\text{Ho}_2\text{Ti}_2\text{O}_7$, as well as the $\text{Ce}_2\text{Sn}_2\text{O}_7$ high- Q diffuse scattering found by Sibille <i>et al.</i> [18]. b) High temperature subtracted diffuse scattering as a function of temperature. The intensity increase near $Q = 0.6 \text{ \AA}^{-1}$ is clearly seen and onsets around 1.5 K. c) A single crystal of $\text{Ce}_2\text{Sn}_2\text{O}_7$ used for heat capacity measurements and d) the polycrystalline sample used for powder heat capacity and neutron diffraction measurements.	115

Chapter 1

Introduction

1.1 Rare-earth Magnetism

Condensed matter physics is a diverse playground for exploring many-body phenomena. Within condensed matter, the magnetism caused by unpaired electrons has drawn immense interest for use in next generation technology. Magnetic materials that preclude order down to very low temperature enable the study of fundamental questions about many-body quantum physics.

1.1.1 Magnetic interactions

There are two main methods for unpaired electrons in an insulator to interact with each other, through either exchange interactions or dipolar interactions. Exchange is a quantum mechanical effect that comes about from the electron-electron interaction and Pauli exclusion principle. If the electron wave-functions overlap spatially, known as direct exchange, the Pauli exclusion principle states that when two electrons are exchanged, the wave-function for the two-electron system must be antisymmetric. As the wave-function is composed of a spin and spatial part, this requires the spin part to either be symmetric (ferromagnetic exchange) or antisymmetric (antiferromagnetic exchange) depending on the orbital symmetry. However, in many magnetic materials, these wave-functions do not overlap, and the exchange interaction is instead mediated through common non-magnetic neighbors, such as O^{2-} , called superexchange. Depending on the specifics of the system, superexchange can be larger than direct exchange, and this is the main exchange interaction that occurs in the rare-earth insulators studied here due to the localized nature of the $4f$ -electrons. For completeness, another form of exchange within rare-earth *metals* is the RKKY (Ruderman-Kittel-Kasuya-Yosida) interaction,

where the localized f -electrons are coupled with each other through conduction electrons. We can write the nearest-neighbor exchange interaction as

$$-J \sum_{i,j} \mathbf{S}_i \cdot \mathbf{S}_j, \quad (1.1)$$

where J is the exchange constant ($J > 0$ indicates ferromagnetic exchange and $J < 0$ indicates antiferromagnetic exchange), and the sum runs over each nearest-neighbor pair. The interactions depends only on the relative orientations of the two spins and the isotropic nature of J is called the Heisenberg interaction. More complex, anisotropic, or next-nearest neighbor interactions can be modeled simply by changing the nature of the J term.

If there does not exist an inversion center between neighboring atoms, an antisymmetric exchange can exist, called the DM (Dzyaloshinskii-Moriya) interaction. The DM interaction takes the form

$$H_{\text{DM}} = \sum_{i,j} \mathbf{D}_{i,j} \cdot (\mathbf{S}_i \times \mathbf{S}_j), \quad (1.2)$$

where $\mathbf{D}_{i,j}$ is the interaction *vector*. The orientation of $\mathbf{D}_{i,j}$ is constrained by the crystal symmetry, and in the case of magnetic interaction through superexchange, $\mathbf{D}_{i,j}$ will be perpendicular to the triangular plane formed by the three ions involved.

Dipolar interactions are due to the interaction of two magnetic dipoles. We can write this interaction between dipoles \mathbf{m}_1 and \mathbf{m}_2 as

$$U = \frac{1}{r^3} [\mathbf{m}_1 \cdot \mathbf{m}_2 - 3(\mathbf{m}_1 \cdot \hat{\mathbf{r}})(\mathbf{m}_2 \cdot \hat{\mathbf{r}})]. \quad (1.3)$$

The $1/r^3$ dependence means that the dipole interaction is relatively long-range, but can sometimes be ignored or limited to nearest-neighbors in the case of small magnetic moments and depending on the relative strength of other interactions.

Magnetic interactions are vital to magnetic order; without them, ordered magnets would not exist. At temperatures well-above the mean interactions felt by each spin, thermal fluctuations

dominate the magnetic interactions and cause the moments to point in random directions. This is known as the paramagnetic state where the magnetic structure is disordered and there exists no macroscopic magnetic moment. As the temperature is lowered below the mean interactions of the system, the system will try to minimize the energy of interactions by aligning the spins in such a way that does this. For a simple 1D chain of Ising spins (point up or down), this simply equates to aligning the moments parallel (ferromagnetic) or antiparallel (antiferromagnetic) to each other. In the case of ferromagnetic order, the aligned moments would form a spontaneous magnetization below the ordering temperature, and would show a macroscopic magnetization density. In contrast, antiferromagnetic order shows no spontaneous magnetization because the moments sum to zero. More complicated crystal structures and interactions lead to more elaborate or unconventional magnetic order than these simple examples, and in the case of frustrated magnets, order can be avoided all together.

1.1.2 Frustrated magnets

The presence of competing interactions is a common occurrence in many magnetic systems, even if only weakly. This competition is called frustration and can often preclude magnetic order, or suppress a magnetic ordering transition to sub-Kelvin temperatures. The more precise definition of frustration is that the energy of total system cannot be minimized by minimizing the interaction energy of the system constituents individually, i.e. the competing interactions cannot be simultaneously satisfied. This leads to many nearly-degenerate states at low energy and frustrated materials can often possess unconventional phases or other exotic physics.

This competition can originate through the exchange interactions of nearest-neighbors with further neighbors or anisotropic exchange, called exchange frustration, or it can come about from the spatial arrangement of the spins on a lattice, called geometric frustration. A simple picture for geometric frustration is antiferromagnetically (AFM) coupled Ising spins (point up or down) on the vertices of a 2D triangular lattice, where the three spins on a single triangle

cannot all be simultaneously AFM aligned (Figure 1.1 a). This model system, when tiled on a lattice, exhibits an infinitely degenerate ground state manifold due to these frustrated interactions. Other types of geometrically frustrated lattices include the Kagome lattice (corner-sharing triangles), the pyrochlore lattice (corner-sharing tetrahedra), and the perovskite lattice (edge-sharing tetrahedra), to name a few (Figure 1.1).

In real systems, there can be both geometric and exchange frustration, which allows us to explore the effects of both in various magnetic systems. Additionally, in realizable systems, frustration can be alleviated by weaker interactions to eventually order at some low temperature T_N while still possessing exotic ground states. The frustration of a system can be parameterized by the frustration parameter, f , given by

$$f = |\theta_{CW}|/T_N \tag{1.4}$$

where θ_{CW} is the Curie-Weiss temperature discussed in detail in Section 1.2.2. In essence, the CW temperature gives a mean scale of interaction strength, so the more suppressed the ordering temperature (T_N) is compared to those interactions, the more frustrated a system is considered to be. The suppression of magnetic order down to ultra-low temperature enables the study of various quantum effects, with a large effort towards the experimental realization of a Quantum Spin Liquid (QSL). A QSL is a long-ranged entangled quantum state (i.e. it cannot be written as a direct product state across the spins in the system) without conventional magnetic order that exhibits fractionalized excitations among other novel features. In contrast to a classical spin liquid, which possesses a residual entropy down to zero temperature due to the highly degenerate ground state, a QSL lacks a residual entropy as the ground state is a single superposition state that can quantum tunnel between the different configurations. Even when a QSL is not realized, unconventional physics and order can sometimes be found from proximity to a QSL state.

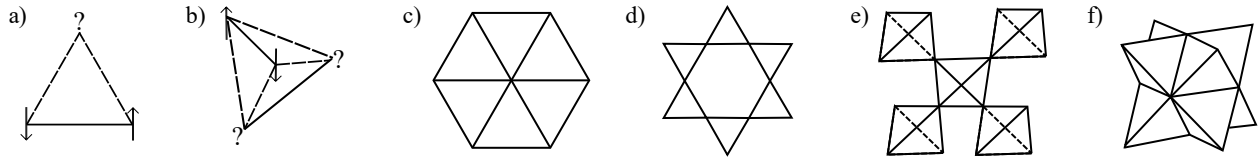


Figure 1.1: a) Canonical example of magnetic frustration, with AFM interacting Ising spins on a triangular lattice. Depending on the top spin direction, either the left or right interaction cannot be satisfied. b) The tetrahedron, a 3D analogue of the triangular lattice frustration. Schematics of various geometrically frustrated lattices: c) triangular lattice composed of edge sharing triangles, d) kagome lattice composed of corner sharing triangles, e) pyrochlore lattice composed of corner sharing tetrahedra, f) perovskite lattice composed of edge sharing tetrahedra.

1.1.3 Spin-orbit coupling and crystal field effects

The heavy nature of rare-earth ions typically causes the spin-orbit coupling to be sufficiently large such that the total angular momentum J is a good quantum number (determined from Hund's rules). The isolated single-ion ground state is then composed of $(2J + 1)$ degenerate energy levels. When embedded in a crystal, these degenerate levels are perturbed and thereby split by the Coulomb interaction with the surrounding crystalline environment which breaks the rotational symmetry of the single-ion ground state. In the $4f$ ions, the effects of the crystal field are typically small compared to the spin-orbit coupling due to shielding from the $5s^25p^6$ orbitals. Therefore, we can use standard perturbation theory to determine the effects of the crystal field, and the first step of this is to find the perturbing Hamiltonian and its matrix elements.

To start, we need to determine the electrostatic potential $V(r)$ on the unpaired electron from the surrounding environment. This potential is incredibly complicated to determine because the surrounding charges (ligands) are distributed in space and may overlap. The resulting theoretical framework of determining the potential due to these charge ligands is called ligand field theory. Due to the complexity, we instead approximate the ligands as static point charges in a simplified theory called crystal electric field (CEF) theory.

Using the CEF static charge approximation, we can write the electrostatic potential at a point r as

$$V(r) = \sum_j \frac{q_j}{|R_j - r|}, \quad (1.5)$$

where $\{q_j, R_j\}$ are the charge and location of the surrounding point charges, and the potential energy is then

$$H_{\text{CEF}} = \sum_i q_i V(x_i, y_i, z_i). \quad (1.6)$$

While this would be sufficient, it can be useful to rewrite Eqn. (1.5) in terms of spherical harmonics (see Ref. [19] for details) as

$$V(r, \theta, \phi) = \sum_n \sum_{m=-n}^n r^n \gamma_{nm} Y_n^m(\theta, \phi) \quad (1.7)$$

where

$$\gamma_{nm} = \sum_j \frac{q_j}{R_j^{n+1}} \frac{4\pi}{2n+1} (-1)^m Y_n^{-m}(\theta_j, \phi_j). \quad (1.8)$$

In 1952, Stevens showed, using an application of the Wigner-Eckart theorem, that the single-electron wavefunctions could be replaced by the coupled system wavefunctions by using an 'operator equivalent' (consisting of angular momentum operators) which acts on the angular part of the coupled system [19, 20]. Eqn. (1.6) is then written as

$$H_{\text{CEF}} = \sum_{n,m} B_n^m O_n^m, \quad (1.9)$$

where O_n^m are the Stevens' operators (linear combinations of angular momentum operators), and B_n^m are known as the Stevens' parameters. Time reversal symmetry constrains n to be even, and $-n \leq m \leq n$ [21]. Additionally, $n < 2l$, where l is the orbital quantum number of the single magnetic electrons, means the 4f rare-earth ions need to only go up to the 6th order at most.

Thinking about this phenomenologically, the surrounding atomic environment is shifting the relative energies of the magnetic ion's electron orbitals by the Coulomb interaction. As the

orbitals have a shape, and the crystallographic environment imposes certain spatial symmetry, it makes sense that the way in which energies are shifted will be effected by the symmetry of the surrounding system. More information on symmetry is given in Section 1.3, but for now, it suffices to say that the specific point group symmetry of the magnetic ion will limit the number of Stevens' parameters to be calculated or fit. Higher symmetries, like cubic or hexagonal, only require 2 to 8 parameters, while low symmetries, like monoclinic or triclinic, can require up to 26 parameters [22, 23, 24, 25].

The point charge calculations are a great place to start when one wants to estimate the energy levels expected, for example to help determine what neutron energies to use during a scattering experiment. However, the reverse calculation, determining the CEF Hamiltonian from experimental data, is significantly more challenging. Experimentally, not all single-ion energy levels can necessarily be resolved due to either low intensity or they could coincide with a phonon mode. Additionally, there can be many degenerate best fit solutions in the case of low symmetry systems where there are a large number of parameters to fit. This can be mitigated by initiating the experimental fits from the point charge calculations, but this is not always successful. Recently, an 'effective point charge model' has been put forward [22] where the charge on the surrounding point charges or ligand environment is fit to the data rather than the Steven's parameters. This greatly limits the number of fitting parameters to solely the surrounding ligands, and has been shown to be successful for a number of rare-earth pyrochlore materials (high symmetry) as well as for some Kagome materials (lower symmetry).

The nature of the CEF splitting is also dependent on the number of electrons the system contains by Kramers' theorem. This theorem states that an odd number of electrons (half-integer total angular momentum J) requires the single-ion energy eigenstates to be at least doubly degenerate and respect time reversal symmetry. Systems with an even number of electrons are time reversal even, so any degeneracy is coincidental and imposed by the crystal symmetry alone. In systems where the CEF splitting creates a large energy gap (Δ) between the ground and first-excited states (as is often the case in the rare-earth pyrochlores, for example), the ground

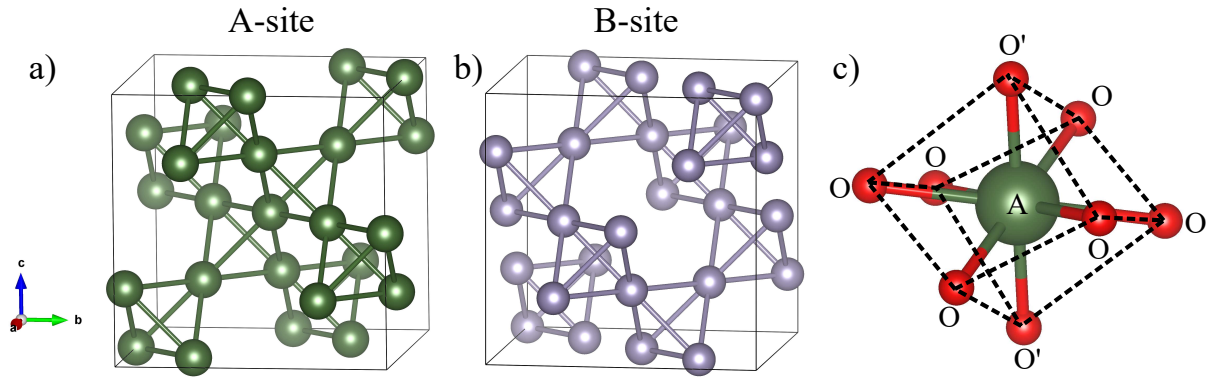


Figure 1.2: The pyrochlore structure showing corner-sharing tetrahedra on both the a) *A*-site and the b) *B*-site, which interpenetrate each other. c) The oxygen cage surrounding a single *A*-site ion. The difference in *A-O'* and *A-O* is responsible for the single-ion anisotropy.

state can be considered isolated at temperatures well below this ($k_B T \ll \Delta$). In this case, when the ground state is a doublet, we can project the system onto an “effective” spin-1/2 basis due to the two degrees of freedom. This is ideal for studying quantum effects and makes the rare-earth frustrated magnets an ideal model system for studying a wealth of phenomena.

1.1.4 Rare-earth pyrochlore oxides, $A_2B_2O_7$

The rare-earth (RE) pyrochlore oxides are some of the most well-studied $4f$ magnetically frustrated systems. The pyrochlore structure consists of a magnetic sublattice of corner-sharing tetrahedra (Figure 1.2 a and b), which, as discussed previously, is one of the archetypes of 3D frustrated geometries. With the general chemical formula $A_2B_2O_7$, where the *A*-site is often a magnetic trivalent rare-earth ion and the *B*-site is typically a tetravalent non-magnetic transition metal ion, one can see that there are a wide range of materials that can be studied within the RE pyrochlore oxides. The single-ion anisotropy, exchange anisotropy, and magnetic moment of the *A*-site can vary dramatically depending on the rare-earth ion used, and therefore we can explore how these influence the ground state. Similarly, we can use different *B*-site atoms to explore the effects of chemical pressure.

The ionic radius of the rare-earth series decreases systematically as the number of electrons increases, known as lanthanide contraction. The ratio of the A^{3+}/B^{4+} radii determines whether

the pyrochlore structure can be stabilized, albeit with a few exceptions [26]. A structure stability map was created in 1993 by Subramanian and Sleight [27] which showed that tin (Sn) is the only *B*-site ion that could form the entire rare-earth series in the pyrochlore structure. Polycrystalline synthesis is relatively straight forward for the RE pyrochlores using standard solid state synthesis, heating stoichiometric ratios of powder up to around 1400°C. For the tin-based pyrochlores, often the inclusion of extra SnO₂ during synthesis is required in order to form the structure due to the volatility of tin. For small *B*-site radii (ex: Ge), high pressure synthesis may be required [28, 29, 30, 31, 32]. Single crystal synthesis techniques are more diverse, utilizing techniques such as floating zone synthesis, vapor transport, and hydrothermal synthesis, depending on the desired system. Due to the similar radii of the *A*- and *B*-site, as well as the fact that some rare-earth ions have other stable oxidation states (ex: Ce³⁺ and Ce⁴⁺), site-mixing and defect formation is possible. The number of defects is often small and difficult to detect, but even low defect densities can have profound effects on the ground state and physics at play due to low interaction strengths and frustration, and is therefore an active area of research within this field.

The RE pyrochlores form in the cubic space group $Fd\bar{3}m$ (227) at room temperature. The oxygen cage surrounding a single *A*-site, shown in Figure 1.2 c), possesses D_{3d} (trigonal) point group symmetry and forms a distorted cube. The difference in bond length between *A-O'* and *A-O* is responsible for the single-ion anisotropy found in the RE pyrochlores, and can give a pronounced axial symmetry with respect to the local $\langle 111 \rangle$ axis (*O'-A-O*). We can quantify the single-ion anisotropy by exploring the CEF Hamiltonian,

$$H_{\text{CEF}} = B_2^0 \hat{O}_2^0 + B_4^0 \hat{O}_4^0 + B_4^3 \hat{O}_4^3 + B_6^0 \hat{O}_6^0 + B_6^3 \hat{O}_6^3 + B_6^6 \hat{O}_6^6, \quad (1.10)$$

where $l = 2, 4, 6$ and the non-zero terms are determined from the D_{3d} point group, discussed in Section 1.1.3. The sign of the first term in the CEF Hamiltonian, B_2^0 , coincides with the axial symmetry in such a way that $B_2^0 > 0$ ($A = \text{Sm, Er, Tm, Yb}$) corresponds to easy-plane anisotropy (perpendicular to $\langle 111 \rangle$), also known as XY-like) and $B_2^0 < 0$ corresponds to easy-axis anisotropy

(also known as Ising-like) [26]. This is also seen in the anisotropic g -tensor, where $g_{\perp} > g_{\parallel}$ indicates XY-like and $g_{\parallel} > g_{\perp}$ indicates Ising-like anisotropy [33].

The CEF splitting in RE pyrochlores of interest can often lead to an isolated doublet ground state, as discussed in Section 1.1.3. We can denote the isolated doublet as $|\pm\rangle$ with a pseudo-spin operator \mathbf{S} . A ground state doublet can then be classified by the point group symmetry to fall into the following categories: effective spin-1/2 doublet (Kramers' ion), "dipolar-octupolar" doublet (Kramers' ion), and non-Kramers' doublet. The effective-spin-1/2 doublet is the most familiar, where the pseudo-spin behaves identically to an $S = 1/2$ spin. The "dipolar-octupolar" (DO) doublet is deemed such because part of the pseudo-spin transforms as a magnetic dipole while the rest transforms as a magnetic octupole, and this occurs for $A = \text{Ce, Nd, and Sm}$ [4, 33, 34]. Finally, the non-Kramers' doublet transforms in part like a magnetic dipole, and in part like an electric quadrupole [33, 35].

We can describe the nearest-neighbor anisotropic exchange Hamiltonian for each of these cases individually. Starting with the effective spin-1/2 doublet, we have

$$H = \sum_{\langle ij \rangle} J_{ij}^{\mu\nu} S_i^{\mu} S_j^{\nu}, \quad (1.11)$$

where $J_{ij}^{\mu\nu}$ is the exchange matrix that allows anisotropic exchange between the spatial coordinates of each spin in the global coordinate (crystal) frame and $\mathbf{S}_i = (S_i^x, S_i^y, S_i^z)$ are the pseudo-spins-1/2 defined in the global basis (note, the Einstein summation convention is used for the implied sum over μ and ν). The global basis is defined by a single tetrahedra centered at the origin, and the four corners are defined as $r_0 = \frac{a}{8}(1, 1, 1)$, $r_1 = \frac{a}{8}(1, -1, -1)$, $r_2 = \frac{a}{8}(-1, 1, -1)$, and $r_3 = \frac{a}{8}(-1, -1, 1)$, where a is the lattice parameter for the conventional FCC lattice. The point group symmetry constrains this model to have only four unique nearest-neighbor couplings, labelled J_1, J_2, J_3 , and J_4 , which correspond approximately to XY-like, Ising-like, off-diagonal, and DM exchange, respectively [36]. The bond-dependent interaction matrices between two spins are given by

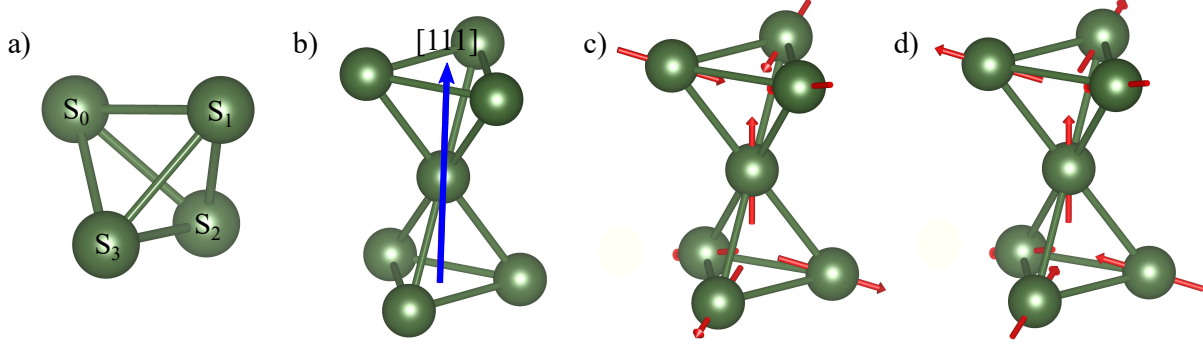


Figure 1.3: a) The sites of a single tetrahedron in the pyrochlore lattice. The bond-dependent interactions between magnetic ions are given by Eqn. (1.12). b) The local $[111]$ axis, equivalent to the C_3 symmetry axis, is shown for two corner sharing tetrahedra on the pyrochlore lattice. c) All-in-all-out (AIAO) ordered magnetic structure. d) One possible spin-ice configuration on the pyrochlore lattice, which follows the ice-rule that two spins point into and two spins point out of the center of the tetrahedra.

$$\begin{aligned}
 \mathbf{J}_{01} &= \begin{pmatrix} J_2 & J_4 & J_4 \\ -J_4 & J_1 & J_3 \\ -J_4 & J_3 & J_1 \end{pmatrix} & \mathbf{J}_{02} &= \begin{pmatrix} J_1 & -J_4 & J_3 \\ J_4 & J_2 & J_4 \\ J_3 & -J_4 & J_1 \end{pmatrix} & \mathbf{J}_{03} &= \begin{pmatrix} J_1 & J_3 & -J_4 \\ J_3 & J_1 & -J_4 \\ J_4 & J_4 & J_2 \end{pmatrix} \\
 \mathbf{J}_{12} &= \begin{pmatrix} J_1 & -J_3 & J_4 \\ -J_3 & J_1 & -J_4 \\ -J_4 & J_4 & J_2 \end{pmatrix} & \mathbf{J}_{13} &= \begin{pmatrix} J_1 & J_4 & -J_3 \\ -J_4 & J_2 & J_4 \\ -J_3 & -J_4 & J_1 \end{pmatrix} & \mathbf{J}_{23} &= \begin{pmatrix} J_2 & -J_4 & J_4 \\ J_4 & J_1 & -J_3 \\ -J_4 & -J_3 & J_1 \end{pmatrix}
 \end{aligned} \tag{1.12}$$

where \mathbf{J}_{01} is the interaction between the spins located at r_0 and r_1 , for example, and these are all related to each other through cubic rotations. [1, 37].

We can recast this Hamiltonian in the global frame to a local frame, where $\mathbf{z}_i^{\text{local}}$ is the local C_3 symmetry axis of the crystal field on site i , also known as the local $\langle 111 \rangle$ (Figure 1.3 b). This leads to

$$\begin{aligned}
 H^{\text{local}} &= \sum_{\langle ij \rangle} [J_{zz} S_i^z S_j^z - J_{\pm} (S_i^+ S_j^- + S_j^- S_i^+) + J_{\pm\pm} (\gamma_{ij} S_i^+ S_j^+ + \gamma_{ij}^* S_i^- S_j^-) \\
 &\quad + J_{z\pm} (S_i^z (\zeta_{ij} S_j^+ + \zeta_{ij}^* S_j^-) + i \leftrightarrow j)],
 \end{aligned} \tag{1.13}$$

where

$$\zeta = \begin{pmatrix} 0 & -1 & e^{i\frac{\pi}{3}} & e^{-i\frac{\pi}{3}} \\ -1 & 0 & e^{-i\frac{\pi}{3}} & e^{i\frac{\pi}{3}} \\ e^{i\frac{\pi}{3}} & e^{-i\frac{\pi}{3}} & 0 & -1 \\ e^{-i\frac{\pi}{3}} & e^{i\frac{\pi}{3}} & -1 & 0 \end{pmatrix}, \quad \gamma = -\zeta^* \quad (1.14)$$

and $J_{zz} = -\frac{1}{3}(2J_1 - J_2 + 2J_3 + 4J_4)$, $J_{\pm} = \frac{1}{6}(2J_1 - J_2 - J_3 - 2J_4)$, $J_{\pm\pm} = \frac{1}{6}(J_1 + J_2 - 2J_3 + 2J_4)$, $J_{z\pm} = \frac{1}{3\sqrt{2}}(J_1 + J_2 + J_3 - J_4)$. The spin S_i^μ is now defined in the local single-ion basis with z being the easy axis. More explicitly, we define the local basis as

$$\begin{aligned} \hat{\mathbf{e}}_0 &= \frac{1}{\sqrt{3}}(1, 1, 1), & \hat{\mathbf{a}}_0 &= \frac{1}{\sqrt{6}}(-2, 1, 1) \\ \hat{\mathbf{e}}_1 &= \frac{1}{\sqrt{3}}(1, -1, -1), & \hat{\mathbf{a}}_1 &= \frac{1}{\sqrt{6}}(-2, -1, -1) \\ \hat{\mathbf{e}}_2 &= \frac{1}{\sqrt{3}}(-1, 1, -1), & \hat{\mathbf{a}}_2 &= \frac{1}{\sqrt{6}}(2, 1, -1) \\ \hat{\mathbf{e}}_3 &= \frac{1}{\sqrt{3}}(-1, -1, 1), & \hat{\mathbf{a}}_3 &= \frac{1}{\sqrt{6}}(2, -1, 1) \end{aligned} \quad (1.15)$$

where $\hat{\mathbf{b}}_i = \hat{\mathbf{e}}_i \times \hat{\mathbf{a}}_i$. This also allows us to easily write the Hamiltonian associated with the non-Kramers' doublet, as the time reversal symmetry even property leads to $J_{z\pm} = 0$, otherwise the equation is unchanged. The Hamiltonian for the DO pyrochlores is also a simplification of Eqn. (1.13), where $\zeta_{ij} = \gamma_{ij} = 1$. This gives

$$H = \sum_{\langle ij \rangle} J_{xx} S_i^x S_j^x + J_{yy} S_i^y S_j^y + J_{zz} S_i^z S_j^z + J_{xz} (S_i^x S_j^z + S_i^z S_j^x), \quad (1.16)$$

where $J_{xx} = 2(J_{\pm\pm} - J_{\pm})$, $J_{yy} = -2(J_{\pm\pm} + J_{\pm})$, and $J_{xz} = 2J_{z\pm}$. The final term in Eqn. (1.16) can be removed by a careful transformation, resulting in a 'simple' XYZ Hamiltonian [4, 33].

Much theoretical work has gone into determining the various and sometimes exotic magnetic ground states that result from these different Hamiltonians. It is found that the ordered magnetic states typically have a $q = 0$ structure, which means the magnetic unit cell and crystallographic unit cell are the same. This allows the magnetically ordered phases to be organized by the transformation properties under the point group symmetry. For the effective spin-1/2

case, five ordered phases occur within the D_{3d} point group: A_{2g} (Γ_3), E_g (Γ_5), T_{1g} and T'_{1g} (Γ_9), and T_{2g} (Γ_7). The Γ_3 phase is known as the all-in-all-out (AIAO) phase (Figure 1.3 c), where all spins point either into or out of the center of the tetrahedra (along $\mathbf{z}^{\text{local}}$). Γ_9 contains both the spin-ice ordered magnetic structure, which follows the “ice rule” that two spins point into the tetrahedra and two spins point out (Figure 1.3 d), as well as the splayed ferromagnetic state. Γ_7 is known as the Palmer-Chalker (PC) state, which will be described in detail in the following section. Finally, the Γ_5 state is unique in that it possesses an accidental U(1) degeneracy where the spins can rotate continuously in the local XY plane (perpendicular to $\mathbf{z}^{\text{local}}$) without changing the energy of the system at the mean field level. The DO pyrochlores have four ordered phases: A_{1g} (Γ_1) and A_{2g} (Γ_3) are octupolar and dipolar AIAO phases, respectively, while T_{1g} (Γ_9) and T_{2g} (Γ_7) are dipolar and octupolar spin-ice phases, respectively [33].

Quantum fluctuations, disorder, or phase competition can destabilize these ordered magnetic phases and lead to a plethora of exotic collective behavior. As there are a large number of studied pyrochlores, we will not go in to the specifics of all of them and will instead focus on the pyrochlores relevant to this thesis. However, we would like to guide the interested reader to two useful review articles, Ref. [26] and Ref. [33].

Er₂Sn₂O₇

Er₂Sn₂O₇ has been an enigma of the rare-earth pyrochlores since it’s physical properties were first measured. The tin-based pyrochlores are notoriously difficult to synthesize as single crystals due to the volatility of tin-oxide, therefore the previous work on Er₂Sn₂O₇ has been performed on polycrystalline samples. Any evidence of a magnetic ordering transition in Er₂Sn₂O₇ avoided detection [38, 39, 40] until 2017 when a second-order antiferromagnetic transition was discovered at $T_N \sim 100$ mK through neutron diffraction, magnetic susceptibility, and heat capacity measurements [15, 16]. The crystal field Hamiltonian was explored using inelastic neutron scattering [38] and found excited multiplets at $E = 5.1, 7.6,$ and 17.2 meV. Using Eqn. (1.10), the authors of Ref. [38] determined the Steven’s parameters which allowed the characterization of the single-ion g -tensor. This showed that Er₂Sn₂O₇ possesses a strong XY (easy plane)

Table 1.1: Properties of well-known XY pyrochlores in comparison to $\text{Er}_2\text{Sn}_2\text{O}_7$ showing the strong XY single-ion nature as well as the suppressed transition temperature.

	$\text{Er}_2\text{Sn}_2\text{O}_7$	$\text{Er}_2\text{Ti}_2\text{O}_7$	$\text{Yb}_2\text{Ti}_2\text{O}_7$	$\text{Yb}_2\text{Ge}_2\text{O}_7$
g_{\perp}	7.52	6.8	4.2	4.2
g_{\parallel}	0.054	2.6	1.8	1.9
T_N (K)	0.01	1.2	0.25	0.57
Ordered state	Γ_7 (PC), AFM	$\Gamma_5(\psi_2)$, AFM	Γ_9 , FM	$\Gamma_5(\psi_3)$, AFM

single-ion anisotropy. The g -values in comparison to other well-known pyrochlores are shown in Table 1.1.

Magnetic Bragg peaks emerged in the elastic neutron scattering (ENS) signal below the ordering transition on top of nuclear Bragg peaks, indicating the magnetic and crystallographic unit cell are the same and $\text{Er}_2\text{Sn}_2\text{O}_7$ therefore possesses a $\mathbf{k} = 0$ ordering wavevector. Utilizing representational analysis (Section 1.3.1), the authors of Ref. [16, 38] found $\text{Er}_2\text{Sn}_2\text{O}_7$ orders into the Γ_7 Palmer-Chalker AFM phase. The gradual increase in ordered moment as temperature is decreased past T_N indicates the transition is second order and the ordered Er^{3+} moment at the lowest measured temperature is $3.1\mu_B$, greatly lowered from the single-ion value of $\sim 9\mu_B$.

Inelastic neutron scattering (INS) in the field polarized regime (above ~ 1.5 T) allowed the estimation of the anisotropic interaction tensor from Eqn. (1.11) using linear spin wave theory (LSWT). Typically single crystal samples are ideal for the LSWT analysis because they provide more information about the anisotropic nature of the sample. However, as previously mentioned, only polycrystalline samples were available, therefore the applied field direction is averaged over all crystallographic directions. Consequently, the authors performed a quasi-powder-average by averaging over the high symmetry directions in the LSWT calculations. Placing the additional constraint $J_4 = 0$, as the DM interaction is typically small in these materials, authors found the full interaction tensor, which placed $\text{Er}_2\text{Sn}_2\text{O}_7$ within the Γ_7 PC phase, in agreement with the ENS conclusions.

Classical Monte Carlo simulations were performed, similarly using the constraint $J_4 = 0$ and the additional constraint $J_3 < 0$ motivated by the estimated parameters of $\text{Yb}_2\text{Ti}_2\text{O}_7$, $\text{Er}_2\text{Ti}_2\text{O}_7$, and $\text{Er}_2\text{Sn}_2\text{O}_7$, to investigate the $T = 0$ ground state phase diagram of the family of XY frustrated

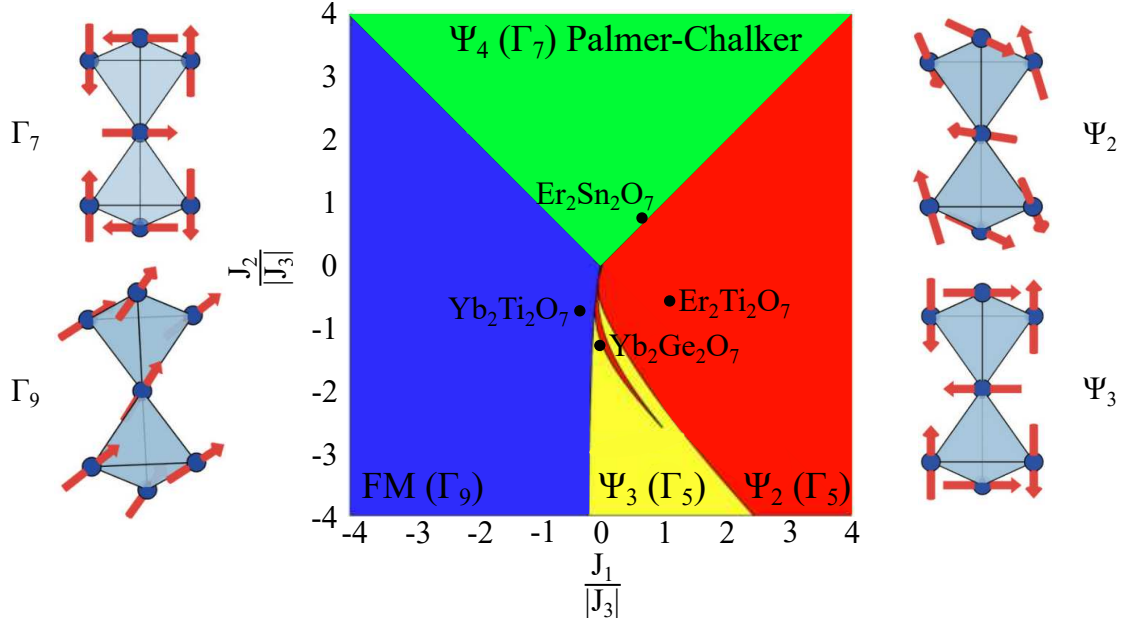


Figure 1.4: Classical ground state phase diagram for effective spin-1/2 pyrochlores with $J_4 = 0$ and $J_3 < 0$. The spin configurations for each phase is shown, and various studied materials are also placed in the respective phases. Note: $\text{Yb}_2\text{Ge}_2\text{O}_7$ does *not* have a J_4 equal to zero, therefore the placement on the phase diagram is for qualitative purposes. Figure adapted from Refs. [1] and [2].

magnets [1], which is shown in Figure 1.4. With the anisotropic interaction parameters determined, $\text{Er}_2\text{Sn}_2\text{O}_7$ along with other XY pyrochlores can be placed on the phase diagram. Interestingly, many of these systems lie in proximity to one or more phase boundaries and show unique behavior. $\text{Yb}_2\text{Ti}_2\text{O}_7$, for example, lies near the ψ_2 and ψ_3 (basis vectors of the Γ_5 phase, see Section 1.3.1) phase boundary and shows rods of diffuse scattering in neutron scattering measurements. Note, $\text{Yb}_2\text{Ge}_2\text{O}_7$ has a non-negligible J_4 value and therefore cannot technically be placed on this diagram, however, we placed a qualitative point to illustrate the proximity of the $\text{Yb}_2\text{Ge}_2\text{O}_7$ ground state to the Γ_9 , ψ_2 , and ψ_3 phase boundaries.

$\text{Er}_2\text{Sn}_2\text{O}_7$ can be seen to lie on the border between the PC phase and the ψ_2 phase, likely tuned by chemical pressure from $\text{Er}_2\text{Ti}_2\text{O}_7$. As discussed, competition can hinder magnetic ordering, whether due to the frustrated magnetic moments *or* due to proximal ground state phases. This is illustrated by the transition temperature. Classical Monte Carlo calculations predict a first-order transition at $T_N^{MC} \sim 200$ mK, meaning phase competition or quantum fluctuations not accounted for by the classical model are likely suppressing the magnetic order to

lower temperatures. In addition to the ψ_2 phase, $\text{Er}_2\text{Sn}_2\text{O}_7$ is in proximity to a disordered region and a $\mathbf{k} = (\frac{1}{2}, \frac{1}{2}, \frac{1}{2})$ state [16, 41]. For these reasons, $\text{Er}_2\text{Sn}_2\text{O}_7$ is an ideal model for studying the effects of phase competition, for example in an applied magnetic field (which would require the use of single crystal samples).

$\text{Ce}_2\text{Sn}_2\text{O}_7$ and $\text{Ce}_2\text{Zr}_2\text{O}_7$

The DO pyrochlores have received recent attention due to the discovery of potential QSL candidates $\text{Ce}_2\text{Sn}_2\text{O}_7$ and $\text{Ce}_2\text{Zr}_2\text{O}_7$. Unlike other QSL candidates, the Hamiltonian of the DO pyrochlores is described by a simple XYZ Hamiltonian, allowing the full parameter space of the phase diagram to be explored, as was done by Ref. [4]. The authors start by rewriting Eqn. (1.16) as

$$H = \sum_{\langle ij \rangle} \left[\left(\sum_{\alpha=x,y,z} J_{\alpha} \tau_i^{\alpha} \tau_j^{\alpha} \right) + J_{xz} \left(\tau_i^x \tau_j^z + \tau_i^z \tau_j^x \right) \right], \quad (1.17)$$

where pseudo-spin- $\frac{1}{2}$ operators τ_i^x and τ_i^z transform like components of the magnetic dipole oriented along the C_3 symmetry axis (local $\langle 111 \rangle$), and τ_i^y transforms as a component of the magnetic octupole (Figure 1.5 a) [3]. A global transformation such that $\tau_i^{\alpha} \rightarrow \tilde{\tau}_i^{\tilde{\alpha}}$ then reduces the problem to

$$H = \sum_{\langle ij \rangle} \sum_{\alpha=\tilde{x},\tilde{y},\tilde{z}} \tilde{J}_{\alpha} \tilde{\tau}_i^{\alpha} \tilde{\tau}_j^{\alpha}. \quad (1.18)$$

The global phase diagram was explored through cluster mean field theory and exact diagonalization and is shown in Figure 1.5 b, adapted from Ref. [4]. There were found to be four U(1) QSL phases, and two ordered phases. The QSL phases are the dipolar or octupolar U(1)₀ or U(1) _{π} , where the 0 or π indicate the U(1) flux penetrating the hexagonal plaquette inherent to the pyrochlore structure. These QSL phases make up approximately 20% of the global phase diagram, exemplifying why the DO pyrochlores are excellent candidates for the experimental realization of a QSL.

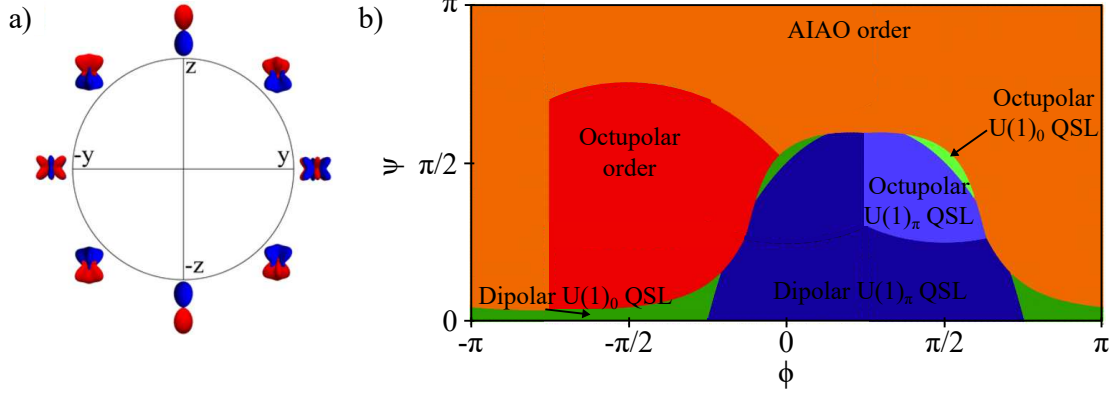


Figure 1.5: a) Visualization of the dipolar/octupolar nature of the DO pyrochlores, where the x and z components of the pseudo-spin transform as components of the magnetic dipole and the y component transforms as a component of the magnetic octupole. Image credit: Ref. [3]. b) The ground state phase diagram for DO pyrochlores using the XYZ model, parameterized such that $\tilde{J}_x = J \cos(\phi) \sin(\psi)$, $\tilde{J}_y = J \sin(\phi) \sin(\psi)$, and $\tilde{J}_z = J \cos(\psi)$, where J is an overall scale factor. Two ordered phases and four QSL phases are found within this phase diagram, with $\sim 20\%$ of the phase space corresponding to the QSL phase. Figure adapted from Ref. [4].

Understanding the disorder in these materials is crucial to understand how it effects the ground state. This is especially challenging in the Ce-based DO pyrochlores, as the $3 + 1/4+$ oxidation states are stable, therefore disorder in these materials is highly probable. Oxidation effects are readily apparent in $\text{Ce}_2\text{Zr}_2\text{O}_7$, where stoichiometric powders are seen to degrade in air on the order of minutes to hours [42]. Single crystal samples are more air-stable due to less surface area exposure. Lattice parameter studies are able to quantify the level of oxidation present [43], as well as thermogravimetric [44] and atomic PDF measurements [18]. $\text{Ce}_2\text{Sn}_2\text{O}_7$ suffers the same single crystal synthesis challenge as $\text{Er}_2\text{Sn}_2\text{O}_7$, but surprisingly, $\text{Ce}_2\text{Sn}_2\text{O}_7$ powders seem to be less susceptible to oxidation compared to $\text{Ce}_2\text{Zr}_2\text{O}_7$. Previous powder studies find $\text{Ce}_2\text{Sn}_2\text{O}_7$ samples are air-stable for years [18].

Both $\text{Ce}_2\text{Sn}_2\text{O}_7$ and $\text{Ce}_2\text{Zr}_2\text{O}_7$ do not show any evidence of ordering at the lowest temperatures measured (~ 50 mK) in heat capacity and neutron scattering measurements [3, 18, 42, 45, 46]. The single-ion properties were explored through INS crystal field measurements, and the crystal field splitting was found to be very similar between the two compounds. The ground state is well separated by $\Delta E \sim 50$ meV (~ 5 K) from the first excited state and in both cases

the ground state doublet wave-function is a linear combination of the $|m_{J_z} = \pm 3/2\rangle$ states, as expected for the DO pyrochlores.

An essential puzzle piece is to determine the interaction parameters that would allow the DO pyrochlores to be placed in the phase diagram of Figure 1.5. A dipolar QSL is found when the easy axis is along the dipolar component (i.e. $|J_{\hat{x}}| > |J_{\hat{y}}|$ or $|J_{\hat{z}}| > |J_{\hat{y}}|$), while an octupolar QSL is found when the easy axis is along the octupolar component (i.e. $|J_{\hat{y}}| > |J_{\hat{x}}|, |J_{\hat{z}}|$). Assuming no dipolar interactions, due to the small moment of Ce^{3+} ($\sim 1.2\mu_B$), Ref. [3] determined the interaction parameters of $\text{Ce}_2\text{Zr}_2\text{O}_7$ using numerical linked cluster calculation fits to the heat capacity and susceptibility experimental measurements. These calculations constrained the ground state to lie within the dipolar $U(1)_\pi$ QSL state, on the boundary between dipolar and octupolar phases. The spin-flip channel of polarized neutron scattering measurements are well-reproduced with the determined interaction parameters, however, the poor agreement with the non-spin-flip channel suggests further neighbor or dipolar interactions may be important.

In contrast, $\text{Ce}_2\text{Sn}_2\text{O}_7$ shows no evidence of magnetic dipole scattering and instead was found to possess diffuse neutron scattering at high momentum transfer (peaked around $Q = 8 \text{ \AA}^{-1}$), attributed to the scattering by magnetic *octupoles* [18]. Mean field calculations using Eqn. (1.16), with the simplification $J_{xx} = J_{xz} = 0$, found two sets of J_{yy} and J_{zz} best fit the measured field dependent heat capacity, magnetization, and effective magnetic moment $\mu_{\text{eff}} \propto (\chi \times T)^{1/2}$. One of these sets places $\text{Ce}_2\text{Sn}_2\text{O}_7$ in an all-in-all-out octupolar ordered regime with “hidden” order, which was ruled out based on the absence of an ordering transition. The second set of parameters places $\text{Ce}_2\text{Sn}_2\text{O}_7$ in the octupolar ice configuration. A similar analysis to $\text{Ce}_2\text{Zr}_2\text{O}_7$ would be beneficial to determine the exact ground state utilizing all allowed interaction parameters.

1.1.5 Rare-earth triangular lattice materials

Within frustrated materials, edge-sharing triangular lattices with Ising AFM coupled spins are the canonical example of geometric frustration. While transition metal triangular lattice

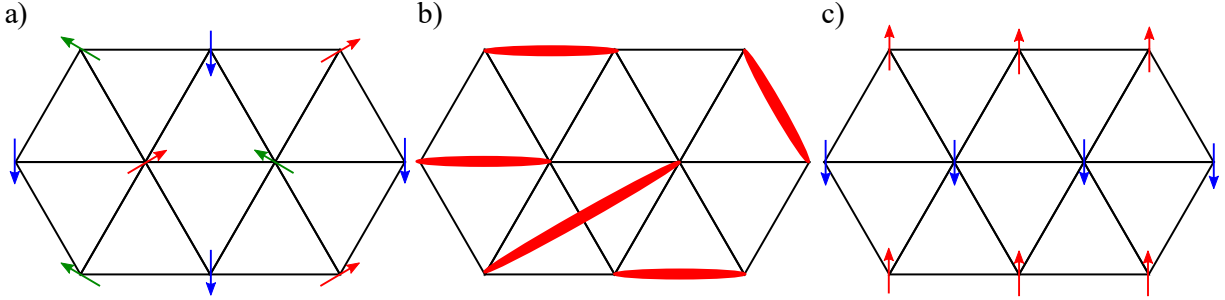


Figure 1.6: Schematics of a) 120° magnetic order, b) quantum spin liquid with fluid valence bonds (spin pairs), and c) stripe order on a 2D edge-sharing triangular lattice.

materials have been well-studied, there has been a surprising lack of rare-earth based triangular lattice materials and thus a significant gap in our knowledge of the role of exchange and single-ion anisotropy in these systems. These materials gained theoretical popularity in 1973 after P.W. Anderson introduced his theory of resonating valence bonds forming a quantum liquid on the triangular layer lattice, where the ground state is a fluid of mobile valence bonds (spin pairs) [47]. Since then, theoretical work has focused on elucidating the ground state phase diagram associated with the spin-1/2 Heisenberg Hamiltonian on the triangular lattice. The authors of Ref. [48] used density matrix renormalization group calculations and first- and second-neighbor Heisenberg interactions (J_1 and J_2 , respectively) on a triangular layer lattice to find two ground state magnetic orders. For small J_2 (compared to J_1), a 120° order is stabilized, and for large J_2 , the ground state forms a striped order (Figure 1.6 a and c, respectively). However, for an intermediate region within this model, a spin liquid state could be realized (Figure 1.6 b) [48].

In real materials, subtle deviations can have significant impacts on the eventually realized ground state of a system. For example, triangular lattice materials can often show symmetry lowering transitions at low temperature where the lattice deviates from perfect equilateral triangles. Additionally, further neighbor interactions can act to stabilize an ordered phase, for example, the out-of-plane interactions in layered materials (depending on the inter-layer to intra-layer distance ratios). For large inter-layer distances, the system can often be treated as an effective-2D lattice where the out-of-plane interactions are effectively ignored.

The most famous example of a rare-earth frustrated triangular lattice is that of YbMgGaO_4 . Unlike the sister compounds, YbCuGaO_4 , $\text{Lu}(\text{Cu}/\text{Co})\text{GaO}_4$, and $\text{Lu}(\text{Zn}/\text{Cu})\text{FeO}_4$, which all show a spin glass state, YbMgGaO_4 does not show evidence of ordering or spin freezing down to 50 mK [49, 50, 51]. Integrated heat capacity measurements showed the entropy plateaus at $R\ln(2)$, suggesting a well-separated effective spin-1/2 ground state. This was corroborated by inelastic neutron scattering (INS) crystal field investigations, which found the first excited state to be separated by 38 meV from the ground state, although the CEF transitions were broader than the instrument resolution, likely due to the presence of Mg/Ga site disorder [49]. Elastic scattering found no Bragg peaks down to the lowest measured temperatures, and, most importantly, INS found broad continuous excitations originally proposed to be associated with spinons from a QSL state [49, 50]. The candidate QSL state was contested from further DMRG calculations that extend the phase diagram by including anisotropic exchange (specifically XXZ anisotropy that is found in YbMgGaO_4) [52]. This work placed YbMgGaO_4 in a striped phase rather than QSL phase, and suggested the striped phase is susceptible to orientational disorder from the Mg/Ga site randomization. This was argued to cause YbMgGaO_4 to “mimic” a spin-liquid-like state, and that in actuality YbMgGaO_4 is likely composed to short-ranged stripe-like domains.

Although it remains controversial, YbMgGaO_4 seemed to reinvigorate rare-earth triangular lattice investigations. In the last few years, many materials in the alkali metal rare-earth chalcogenide family, ARECh_2 ($A^+ = \text{Na, K, Cs, and Li}$, $\text{RE}^{3+} = \text{rare-earth ions, mostly Yb, Er, and Ce}$, and $\text{Ch}^{2-} = \text{O, S, Se, and Te}$), have been receiving recent attention [53, 54, 55, 56, 57, 58, 59, 60, 61, 62, 63, 64, 65, 66, 67, 68, 69, 70, 71, 72, 73]. The materials not containing oxygen are typically found to have small single-ion separations between the ground and first excited states, and therefore the CEF scheme often needs to be investigated. Recently NaYbO_2 has been highlighted as a QSL candidate, as it possesses no magnetic order down to 50 mK investigated through ENS and heat capacity, and does possess non-negligible inter-layer exchange (inter- to intra-layer ratio is 1.6, in contrast to YbMgGaO_4 with a ratio of 2.5). There is still plenty of work

to do to fully investigate this family of materials (as well as other triangular lattice materials) with potential for more QSL or exotic states.

1.2 Experimental Techniques

1.2.1 Heat capacity

Heat capacity is an essential measurement in condensed matter physics for material characterization. While the textbook definition of heat capacity is simply the amount of heat required to raise the temperature of the material by 1 K, the utility of such measurement is much greater than the definition suggests. Low temperature heat capacity specifically can be used to study phase transitions (crystallographic or magnetic) and magnetic properties. We will first discuss the theoretical signatures [6, 74, 75] we expect to see during a heat capacity measurement, then we will discuss the instrument specific considerations [5, 76, 77] for performing a heat capacity experiment.

Theoretical considerations

The mathematical definition of heat capacity at constant volume is given by

$$C_v = \left(\frac{\partial U}{\partial T} \right)_v, \quad (1.19)$$

where U is the internal energy of the system. Typical heat capacity signatures that we measure can fall into one of three categories which I will discuss separately: phonon contributions, Schottky anomalies, and phase transitions.

First, we will explore the effects of phonons. In a static lattice, the specific heat of a metal was theorized in the Sommerfeld theory of metals to be proportional to temperature (T) due to the free electron degrees of freedom (d.o.f.). This would mean that the heat capacity of insulators should not deviate much from the $T = 0$ value, however, this was not seen experimentally. This is because the lattice d.o.f. contribute to the heat capacity as well. We call these quantized

lattice vibrational modes “phonons”. At low temperatures compared to the optical phonon frequencies, we can approximate the heat capacity as

$$C_v \sim \frac{2\pi^2}{5} k_B \left(\frac{k_B T}{\hbar c} \right)^3 \quad (1.20)$$

due to the linear dispersion of acoustic phonons in three dimensions. We often see this characteristic T^3 behavior when measuring heat capacity in the $T > 1$ K range. In our work, we are interested in the magnetic behavior rather than the lattice behavior, so it is sometimes necessary to remove the phonon contribution. The easiest way to do this is to perform a similar measurement with a non-magnetic analogue, as it should have a nearly identical lattice (and thus lattice vibrations) but will not contribute any magnetic signal.

Next, we will discuss the heat capacity from a two level system, called a “Schottky anomaly.” For a two-level system with discrete energy levels at $\varepsilon_1 = 0$ and $\varepsilon_2 = \Delta$, we can write the partition function as

$$\begin{aligned} Z &= \sum_i e^{-\beta \varepsilon_i} \\ &= 1 + e^{-\beta \Delta}, \end{aligned} \quad (1.21)$$

where $\beta = \frac{1}{k_B T}$. Given the definition of internal energy for N particles as $U = -N \frac{\partial}{\partial \beta} \ln Z$, we find

$$\begin{aligned} U &= N \frac{\Delta e^{-\beta \Delta}}{1 + e^{-\beta \Delta}} \\ &= N \frac{\Delta}{e^{\beta \Delta} + 1} \end{aligned} \quad (1.22)$$

To find the heat capacity related to this internal energy, we can begin by rewriting Eqn. (1.19) as

$$\begin{aligned} C &= \left(\frac{\partial U}{\partial T} \right) \\ &= \left(\frac{\partial \beta}{\partial T} \right) \left(\frac{\partial}{\partial \beta} \right) U \\ &= \frac{-1}{k_B T^2} \left(\frac{\partial U}{\partial \beta} \right) \end{aligned} \quad (1.23)$$

and inserting Eqn. (1.22) into Eqn. (1.23) we find

$$\begin{aligned}
C &= -N \frac{\Delta}{k_B T^2} \frac{\partial}{\partial \beta} \left(\frac{1}{e^{\beta\Delta} + 1} \right) \\
&= N \frac{\Delta^2}{k_B T^2} \frac{e^{\beta\Delta}}{(e^{\beta\Delta} + 1)^2} \\
&= N k_B \left(\frac{\Delta}{k_B T} \right)^2 \frac{e^{\Delta/k_B T}}{(e^{\Delta/k_B T} + 1)^2}.
\end{aligned} \tag{1.24}$$

One can plot this result as a function of temperature to find that a broad peak appears in the heat capacity with a maximum at $k_B T \sim 0.417\Delta$ (which can be rewritten as $\Delta \sim (0.21 \text{ meV/K}) T$).

Thinking about this on a more qualitative level, at low-enough temperature we expect only the ground state to be populated and there is little change in the internal energy with respect to temperature. As temperature is increased, the excited level begins to be populated and the internal energy increases dramatically, hence the heat capacity will increase. With a further increase in temperature, eventually both states will be equally populated and the internal energy will fall back, thus creating the anomalous peak in the heat capacity. This same process can be applied for any finite level system with discrete energy levels.

Experimentally, we can utilize the signature of a Schottky anomaly to estimate the energy level separation in our system. As discussed in Section 1.1.3, the frustrated rare-earth magnets we study typically have well-separated single-ion energy levels, on the order of 50 – 100 K (5 – 10 meV) between the ground and first excited state, and thus we would be unlikely to see a Schottky anomaly during a low-temperature ($< 4\text{K}$) measurement. However, as is found in Chapter 2, low-lying single-ion energy levels can exist and it can be necessary to characterize them in order to separate out features of interest from the Schottky anomaly.

The final, and perhaps most important, heat capacity signature that we are interested in is due to phase transitions (specifically magnetic ordering). In a magnetic crystal lattice, a phase transition occurs when there is a sudden rearrangement in the system, whether that be the atom positions or the magnetic spin directions. For example, as temperature is lowered in a system, it can be energetically favorable for atoms to be slightly displaced from their higher symmetry

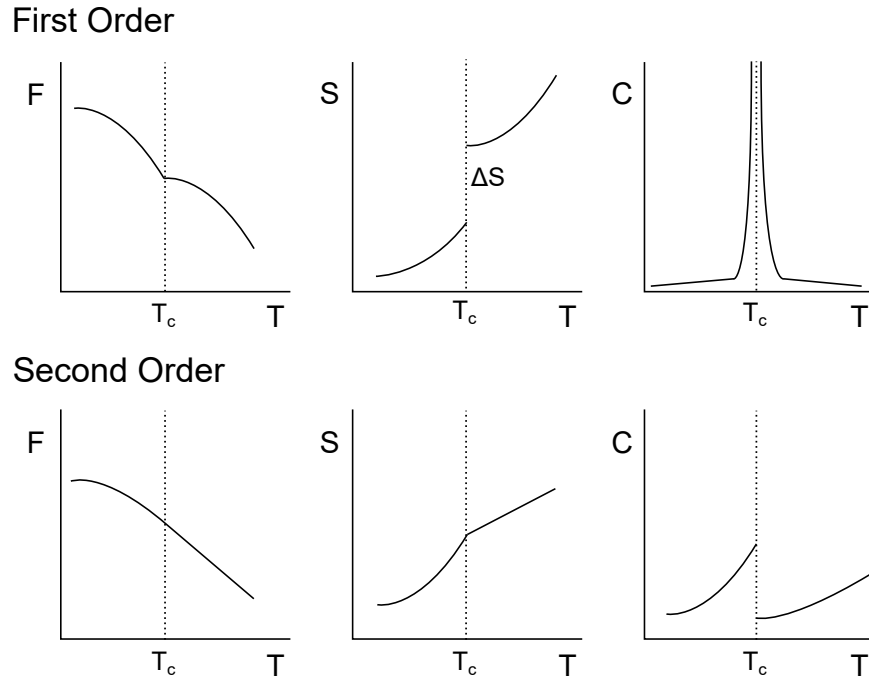


Figure 1.7: Illustrative graphical representations of the free energy, F , entropy, S , and heat capacity, C , for first and second order transitions near the critical temperature, T_c .

positions. This is called a symmetry lowering transition. The same is true for a transition from a paramagnet, where all of the magnetic spins point in random orientations, to a ferro- or antiferromagnet. A paramagnet has spherical spin symmetry, while an ordered magnet will have some lower symmetry (the specific symmetry depends on the system of study).

In order to discuss the experimental heat capacity signature of a phase transitions, we first need to introduce the distinction between a first- and second-order phase transition. A transition is considered first-order when the state changes suddenly, or discontinuously, between two states (i.e. there is a phase coexistence). In contrast, a second-order transition is a continuous, gradual change in the state, and there is no phase coexistence because there is only one phase. In both cases, if the symmetry changes, it does so discontinuously, but the gradual change required for a second-order transition dictates that the lowered symmetry must be a subgroup of the symmetry prior to the transition. During a first-order transition, there is an associated latent heat, so the free energy will have a kink at the critical temperature (T_c) and the entropy will have a discontinuity, ΔS . As the heat capacity is related to the entropy by a derivative, it

will exhibit a vertical asymptote at T_c , experimentally realized as a sharp, λ -looking, peak. See Figure 1.7 for a graphical summary of first- and second-order transitions. How we differentiate these transitions experimentally will be discussed later.

Experimental considerations

To more easily relate the heat capacity to experimental measurements, we can rewrite Eqn. (1.19) as

$$C_p = \left(\frac{\Delta Q}{\Delta T} \right)_p, \quad (1.25)$$

where ΔQ is the amount of heat added to the system and we have changed to a constant pressure measurement as this is more experimentally feasible. This heat is typically added experimentally by a heating coil, and thus can be measured as $\Delta Q = I^2 R \Delta t$, where I and R are the current through and resistance of the coil, and Δt is the amount of time the heater is on. Typically the sample is also suspended in a vacuum and connected to a cold finger through weak thermal contact to minimize heat lost to the sample environment.

We employ the use of a Quantum Design Physical Properties Measurement System (PPMS) with a dilution refrigerator (DR) insert to reach temperatures as low as 50 mK. The DR takes advantage of the entropy of mixing to reach these ultra-low temperatures (schematic shown in Figure 1.8 e). A mixture of liquid ^3He and ^4He separate in the mixing chamber into a “dilute” phase (mostly ^4He) and pure ^3He phase. A turbo pump reduces the concentration of ^3He within the dilute phase. This is replaced by atoms from the concentrated ^3He phase, but in order to cross the boundary between the phases, the ^3He atom must absorb some energy (and therefore heat), cooling the system. Then, the pumped ^3He gas is recondensed and recombined into the pure phase, forming a contained cycle. This allows the DR system to remain at ultra-low temperatures for long time periods and without the loss of helium.

For PPMS heat capacity measurements, a sample is mounted using low-temperature grease on a sapphire platform, suspended in vacuum by kapton tubes (Figure 1.8 f). A heater and

thermometer are connected by wires and gold leads to the electronics and thermal bath, with thermal conductivity K_{wire} . We employ two measurement techniques, the conventional quasi-adiabatic thermal relaxation technique (hereafter called “short pulse”), and a large ΔT thermal relaxation technique (hereafter called “long pulse”).

The short pulse technique is the conventional measurement and analysis used by the Quantum Design Multivu data acquisition programming. In this case, the heater applies a 1 – 2% temperature increase heat pulse and the temperature is tracked upon heating and cooling (Figure 1.8 a). When the crystal is perfectly thermally connected to the sample stage, the temperature change follows

$$C_{\text{total}} \left(\frac{dT}{dt} \right) = -K_{\text{wire}}(T - T_{\text{bath}}) + P(t), \quad (1.26)$$

where C_{total} is the heat capacity from the sample and stage with grease, T_{bath} is the temperature of the bath, and $P(t)$ is the heater power which is a step-wise function (P_0 when the heater is on, 0 when the heater is off after time t_0) [76]. Solving this differential equation for $T(t)$, we find

$$T(t) = \begin{cases} P_0 \tau_1 (1 - e^{-t/\tau_1}) / C_{\text{total}} + T_{\text{bath}} & 0 \leq t \leq t_0 \\ P_0 \tau_1 (1 - e^{-t_0/\tau_1}) e^{-(t-t_0)/\tau_1} / C_{\text{total}} + T_{\text{bath}} & t > t_0 \end{cases} \quad (1.27)$$

where $\tau_1 = C_{\text{total}}/K_{\text{wire}}$ (called the characteristic time constant). This is then used to fit the temperature vs. time curve and extract $C_{\text{total}}(T)$. This process is then repeated at many temperature set-points to map out $C(T)$ and find ordering transitions (Figure 1.8 c). In the situation where there is poor thermal contact between the sample and stage, Eqn. (1.26) and (1.27) are no longer valid because the sample and stage are can no longer be assumed to be the same temperature. In this case, there will be two characteristic times, τ_1 and τ_2 , to fit the slight jump that occurs in the data after the heater turns off (Figure 1.8 a), due to the heat capacity of the grease holding on the sample.

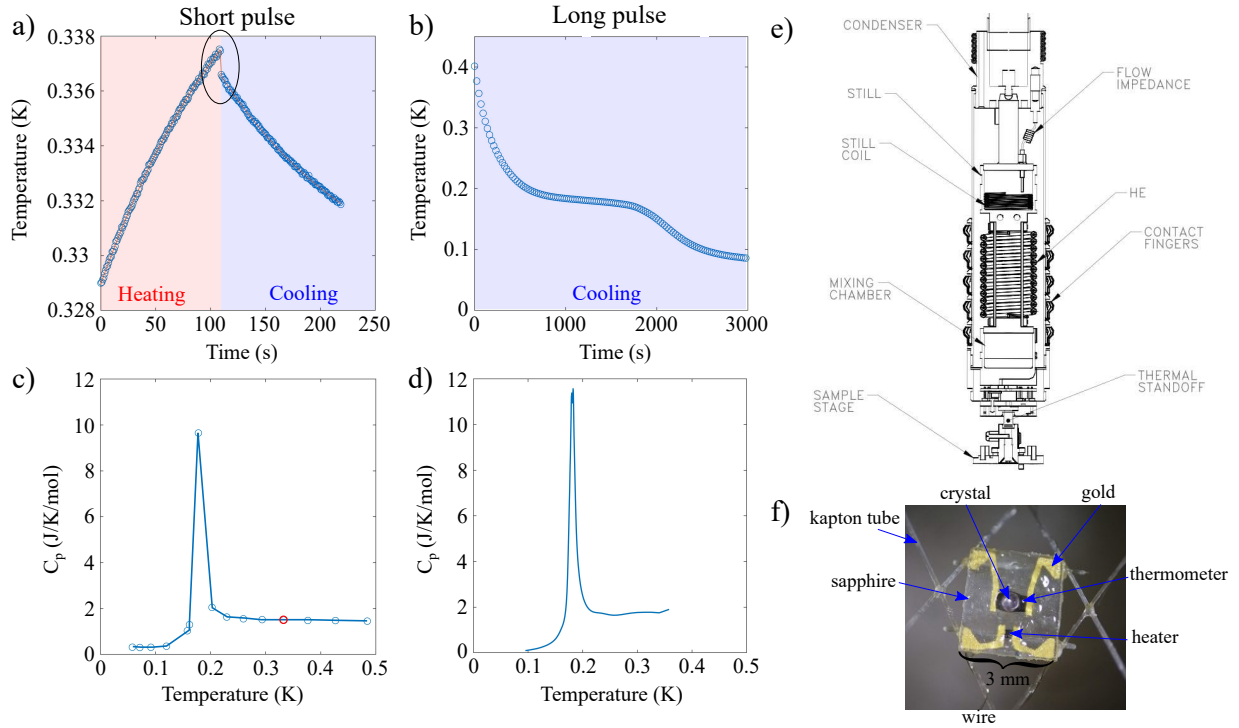


Figure 1.8: Temperature with respect to time after a heat pulse during a (a) short pulse and (b) long pulse measurement. The heating and cooling parts of the measurements are shown with red and blue respectively. The jump between heating and cooling in the (a) short pulse measurement due to a τ_2 contribution is circled. (c) The extracted short pulse heat capacity with the specific fitted data point associated with the heat pulse in (a) highlighted in red. (d) The heat capacity extracted from a long pulse measurement, showing the continuous nature due to using the entire cooling curve. (e) The Quantum Design dilution refrigerator probe. Image credit: Ref. [5] (f) A crystal mounted on the sapphire sample stage which is suspended in vacuum.

The long pulse technique is similar to the short pulse technique in that they both apply heat pulses and measure the relaxation of the temperature with respect to time. However, a long pulse applies a significantly larger temperature increase of up to 300% and are designed such that the sample will be heated through a phase transition (Figure 1.8 b). The resulting heat capacity is then related to the temperature vs. time cooling curve through a derivative. Rewriting Eqn. (1.26) slightly,

$$C = \left(\frac{dT}{dt} \right)^{-1} [Q - P(t)] \quad (1.28)$$

and

$$Q = \int_{T_{\text{bath}}}^{T_{\text{sample}}} [K_{\text{wire}}(T) + K_{\text{offset}}] dT \quad (1.29)$$

is the heat flow through the wire, including some losses from the surrounding environment via a thermal conductance “ K_{offset} ”. The term dT/dt can be explicitly calculated from the measured cooling curve, and $K_{\text{wire}}(T)$ is found during puck calibrations during the PPMS heat capacity option installation. These calculations are done with the LongHCPulse python code and details of the data treatment can be found in Ref. [77]. Because the heat capacity is extracted for the entire cooling curve, this gives a much more comprehensive measurement (Figure 1.8 d) that more accurately maps out phase transitions. As can be seen in Figure 1.8 b, the other added benefit of long pulse measurements are that they give insights into the nature of the transition, whether it is first- or second-order due to the observed (or absent) latent heat as well as whether the peak is sharp or broad from better peak point coverage. The long-pulse heat capacity method was essential for mapping out the field vs. temperature phase diagram that we will introduce in Chapter 3.

1.2.2 Magnetometry

Magnetometry is another essential characterization technique for magnetic systems. The response of a material to an external magnetic field can give insights into the underlying magnetic Hamiltonian. The output of a system under an applied magnetic field (\mathbf{H}) is the magnetization (\mathbf{M}), or magnetic moment per unit volume, and the response function is called the susceptibility, χ . The measurement of these as a function of applied field and temperature can allow us to determine the ordering transition temperature, type of magnetic order, g-tensor, effective magnetic moment, and more.

Theoretical considerations

We can write the magnetization as

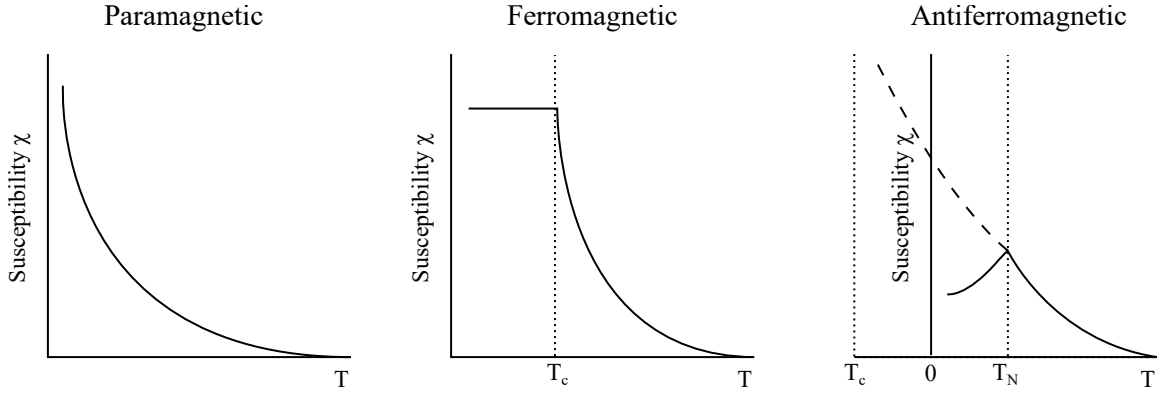


Figure 1.9: Figure adapted from Ref. [6] showing the expected magnetic susceptibility signatures for a paramagnetic, ferromagnetic, and antiferromagnetic material. As temperature is decreased, the moments will align (or anti-align) more readily and follow a $1/T$ dependence. Magnetic order then breaks this trend and either saturates (ferromagnet) or decreases toward zero (antiferromagnet).

$$\mathbf{M} = \chi(T)\mathbf{H} \quad (1.30)$$

where we assume \mathbf{M} is linear in \mathbf{H} (otherwise $\chi(T) = \partial\mathbf{M}/\partial\mathbf{H}$). It can be seen from Eqn. (1.30) that when the magnetic moments align with the field, $\chi > 0$, which known as a paramagnet, and when they align antiparallel with field, $\chi < 0$, which known as a diamagnet.

Assuming a linear response to the field, which is the case at low fields compared to the magnetic interaction strength, we can track the susceptibility as a function of temperature (at constant applied field \mathbf{H}), as high temperature acts to destroy magnetic order through thermal fluctuations. As temperature is decreased, we expect the moments to align (or anti-align) more readily with the field, and thus the susceptibility would increase (Figure 1.9 a), following Curie's law

$$\chi = \frac{C_W}{T}, \quad (1.31)$$

where C_W is Curie's constant. However, the spontaneous magnetic order will deviate from this as the magnetic moments rotate into the most energetically favorable orientation. In the case of a simple ferromagnet, mean field theory was used to implement a correction to the susceptibility to account for the transition, called the Curie-Weiss law,

$$\chi = \frac{C_{CW}}{T - T_{CW}} \quad (1.32)$$

where T_{CW} is the critical (Curie-Weiss, CW) temperature (also sometimes denoted as θ_c). This mean field model is highly idealized and paints a poor picture near the critical region, and therefore is only accurate as long as $T \gg T_{CW}$. Below the idealized FM ordering transition T_c , the magnetic moment should remain constant at the ordered value, and thus the susceptibility should remain constant (Figure 1.9 b). For an AFM, the Curie-Weiss law still holds, however, the CW temperature is negative. The ordering temperature is called the Néel temperature (T_N), and it is at this point that the susceptibility has a cusp as we expect the average magnetic moment (magnetization) to be (or tend to) zero for an antiferromagnet (Figure 1.9 c). We can therefore use these signatures in the χ vs. T measurements to infer the type of magnetic order in our materials.

Additionally, the CW temperature gives insights into the approximate strength of magnetic interactions in the system, with the FM mean field theory definition given by

$$T_{CW} = \frac{S(S+1)}{3k_B} J_0, \quad (1.33)$$

where S is the spin quantum number, k_B is the Boltzmann constant, and J_0 is the mean interaction strength. In frustrated magnetic systems, we can relate this to how frustrated a system is based on how much the ordering transition is suppressed compared to the CW temperature. This “frustration parameter” is $f = \frac{\theta_c}{T_N}$, therefore a small ordering transition temperature compared to CW temperature means the system is more frustrated.

We can also explore the non-linear response of a material at a constant temperature to a changing applied magnetic field. For a simple paramagnet with angular momentum quantum number J , we expect the magnetization to follow

$$M = Ng\mu_B J B_J(x), \quad (1.34)$$

where

$$B_J(x) = \frac{2J+1}{2J} \coth\left(\frac{(2J+1)x}{2J}\right) - \frac{1}{2J} \coth\left(\frac{x}{2J}\right) \quad (1.35)$$

is the Brillouin function, $x = gJ\mu_B B/k_B T$, N is the number of atoms in the system, and μ_B is the Bohr magneton ($\mu_B = \frac{e\hbar}{2m_e} \approx 0.0578$ meV/T). The saturation magnetization (when the applied field is large) can give us information on the g -tensor (and therefore magnetic anisotropy) of the studied material, as

$$M_{\text{sat}} = Ng\mu_B J. \quad (1.36)$$

Experimental considerations

All susceptibility and magnetization measurements were performed on a Quantum Design Magnetic Properties Measurement System (MPMS) XL and MPMS3 with a base temperature of 1.8 K. The MPMS uses a SQUID (superconducting quantum interference device) to perform extremely sensitive magnetic measurements on the order of 10^{-8} emu. We employ a DC scan, where the sample is moved at a constant speed through detection coils, and the change in flux through those coils produces an electronic signal through Faraday's Law (Figure 1.10). This electronic signal is amplified through the SQUID, and a voltage vs. position function can be fit to extract the magnetic moment, assuming a dipole response.

Measurements can be performed on crystals or powder, but the important aspect is that they should not move. This requires the use of eicosane (non-magnetic wax) that can be melted with powder samples to hold the grains in place when a magnetic field is applied. Crystals are typically mounted on a plastic or quartz plate with GE-varnish or crystal bond and inserted into the sample holder. Rotation measurements were also employed with the MPMS3 and are described in Section 2.5.

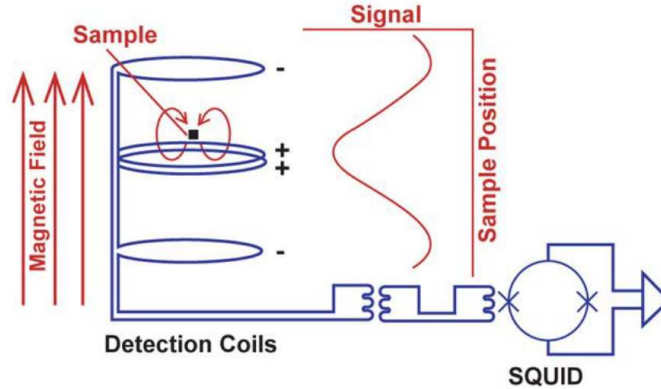


Figure 1.10: Schematic of the MPMS showing the sample moves through the pickup (detection) coils, creating a voltage signal that is amplified using a SQUID. Figure from Ref. [7].

1.2.3 Neutron scattering

One of the most instrumental techniques for studying complex magnetism and magnetic dynamics is neutron scattering. The fundamental properties of thermal neutrons coincide with the energy (~ 25 meV) and wavelength (~ 1.8 Å) of typical excitations and atomic distances in condensed matter systems, making it the perfect probe of such phenomena. Unlike x-rays and protons, the neutral charge of the neutron limits the nuclear interaction with atoms to the strong force. The short-range nature of the strong force restricts nuclear interactions to be infrequent and the neutron therefore penetrates deeply into a material, making it a bulk probe that allows for various sample environments (magnetic field, low or high temperature, pressure, to name a few). Additionally, because the neutron is interacting with the nucleus, it is privy to some light elements, like Hydrogen and Oxygen, which are difficult to detect via x-ray scattering. The scattering length (to be discussed later) is found to be independent of Z and thus neutron scattering can be used to differentiate isotopes. Most importantly for our work, we can take advantage of the fact that a neutron possesses a magnetic moment and will therefore scatter due to unpaired electrons in the material. Because of the versatility of the neutron, there is also a versatility among the instruments used to prepare, scatter, and measure neutrons based upon the phenomena they are intended to probe. In this section, we will introduce the basics

of neutron scattering theory [10, 78, 79, 80, 81, 82, 83] before discussing instrument specific considerations.

Theoretical considerations

An incoming neutron can be described by its incident energy and momentum (wave-vector) as

$$E_i = \frac{|\mathbf{p}_i|^2}{2m} = \frac{\hbar^2 |\mathbf{k}_i|^2}{2m}. \quad (1.37)$$

The quantity that is actually measured during this scattering is the number of neutrons that have been scattered into a detector with solid angle $d\Omega$ and have a final energy between E_f and $E_f + dE_f$ (Figure 1.11 a). This is known as the double differential cross-section and is given by

$$\frac{d^2\sigma}{d\Omega dE_f} = \frac{|\mathbf{k}_f|}{|\mathbf{k}_i|} \sum_{\lambda_i, \lambda_f} p_{\lambda_i} |\langle \mathbf{k}_f \lambda_f | V | \mathbf{k}_i \lambda_i \rangle|^2 \delta(\hbar\omega - (E_i - E_f)), \quad (1.38)$$

where $\mathbf{k}_{\{i,f\}}$ is the incoming and outgoing wavevector of the neutron, p_{λ_i} is a probability, $\lambda_{i,f}$ is the initial and final states of the system of study, V is the scattering potential, and $\hbar\omega$ is the energy transfer of the neutron to the system. While I will not derive Eqn. (1.38) (detailed derivations can be found in Refs. [78, 83, 84]), I will motivate the individual terms. First, the δ -function is required due to conservation of energy, such that the energy lost by the neutron is the energy imparted to the system. The term $|\langle \mathbf{k}_f \lambda_f | V | \mathbf{k}_i \lambda_i \rangle|^2$ is the result of Fermi's golden rule, which states that the probability of changing states from \mathbf{k}_i to \mathbf{k}_f (neutron) and λ_i to λ_f (scattering system) after interacting with a scattering potential V is proportional to the coupling between the initial and final states. p_{λ_i} is the probability that the system is in an initial quantum state λ_i , where the exact form depends on the system of study.

We will discuss two forms of the interaction potential from the two main types of scattering we are concerned with: nuclear (crystal structure, specifically) and magnetic. As discussed, the neutron interacts with the nucleus of atoms via the strong force, which is a short-range

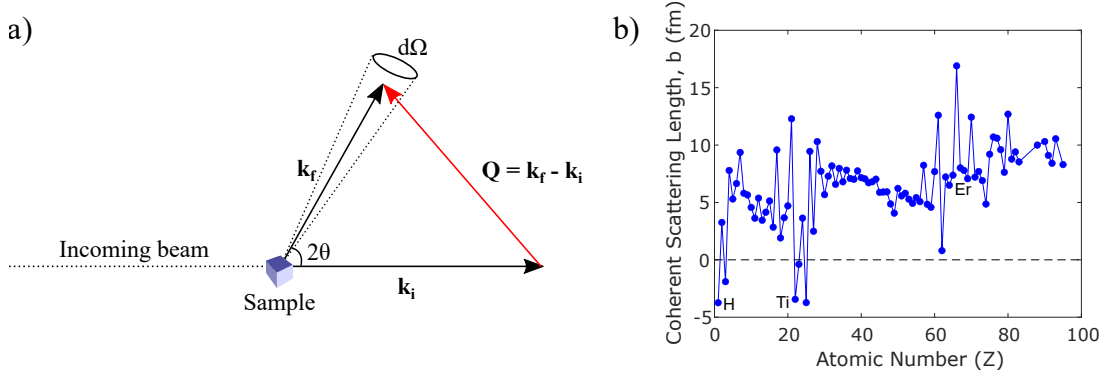


Figure 1.11: a) Neutron scattering set-up. The incoming beam of neutrons has initial energy E_i and wavevector \mathbf{k}_i before interacting with sample. After interaction, the scattered neutron has energy E_f and wavevector \mathbf{k}_f , and is scattered into area $d\omega$ at an angle of 2θ . b) Coherent scattering length, b , as a function of atomic number, Z . The non-monotonic nature of the coherent scattering length allows for the study of light elements and discerning different isotopes of the same material not possible with x-ray scattering. Data extracted from Ref. [8].

interaction (on the order of femtometers). We can therefore treat the nuclear interaction potential as a δ -function, which takes the form

$$V(\mathbf{r}) = b\delta(\mathbf{r} - \mathbf{R}) \quad (1.39)$$

for a single, fixed nucleus at \mathbf{R} , where b is the scattering length (a non-monotonic phenomenological value describing the nuclear scattering process). One of the great benefits of neutron scattering can be seen in Figure 1.11 b) where the scattering length as a function of atomic number, Z , is seen to be non-monotonic. This complex behavior is contrasted to x-ray scattering in which the scattering length is directly proportional to Z , and this allows some light elements, such as hydrogen, to be studied through neutron scattering.

Eqn. (1.39) is known as the “Fermi pseudo-potential” and can be rewritten for the case of multiple fixed scatterers (a lattice) as

$$V(\mathbf{r}) = \sum_n b_n \sigma(\mathbf{r} - \mathbf{n}), \quad (1.40)$$

where \mathbf{n} are lattice sites, and b_n is the scattering length of the atom at the specific lattice site. It can be shown that inserting this in to the double differential cross-section, Eqn. (1.38), one obtains

$$\begin{aligned} \frac{d^2\sigma}{d\Omega dE_f} &= \frac{1}{2\pi\hbar} \frac{|\mathbf{k}_f|}{|\mathbf{k}_i|} \sum_{i,j} \overline{b_i b_j} \int \langle e^{-i\mathbf{Q}\cdot\mathbf{R}_i(0)} e^{-i\mathbf{Q}\cdot\mathbf{R}_j(t)} \rangle e^{-i\omega t} dt \\ &= \frac{1}{8\pi^2\hbar} \frac{|\mathbf{k}_f|}{|\mathbf{k}_i|} \left(\sigma_c \sum_{i,j} \int \langle e^{-i\mathbf{Q}\cdot\mathbf{R}_i(0)} e^{-i\mathbf{Q}\cdot\mathbf{R}_j(t)} \rangle e^{-i\omega t} dt \right. \\ &\quad \left. + \sigma_i \sum_j \int \langle e^{-i\mathbf{Q}\cdot\mathbf{R}_j(0)} e^{-i\mathbf{Q}\cdot\mathbf{R}_j(t)} \rangle e^{-i\omega t} dt \right), \end{aligned} \quad (1.41)$$

where $\mathbf{Q} = \mathbf{k}_f - \mathbf{k}_i$ is the scattering vector, and \mathbf{R} is the position of the nucleus. $\sigma_c = 4\pi\overline{b}^2$ and $\sigma_i = 4\pi(\overline{b^2} - \overline{b}^2)$ are the total coherent and incoherent cross-sections (integrated over all directions), respectively. As we can see from Eqn. (1.41), the coherent part of the equation gives the correlations between different nuclei (i, j) and collective excitations (e.g. Bragg scattering), while the incoherent is related to correlations from a single nuclei (j) and single-particle excitations (e.g. diffusion, crystal field excitations).

We can further simplify the double differential cross-section by introducing correlation functions. The dynamic structure factor is given by

$$S(\mathbf{Q}, \hbar\omega) = \frac{1}{2\pi\hbar} \int I(\mathbf{Q}, t) e^{-i\omega t} dt, \quad (1.42)$$

which is the Fourier transform with respect to time of the intermediate scattering function, $I(\mathbf{Q}, t)$. The intermediate scattering function is then given by

$$I(\mathbf{Q}, t) = \int G(\mathbf{r}, t) e^{i\mathbf{Q}\cdot\mathbf{r}} d\mathbf{r}, \quad (1.43)$$

which is the space-Fourier transform of the space-time correlation function

$$G(\mathbf{r}, t) = \frac{1}{N} \sum_{i,j} \langle \delta(\mathbf{r} + \mathbf{R}_i(0) - \mathbf{R}_j(t)) \rangle. \quad (1.44)$$

The space-time correlation function describes the position of the nuclei in space and time. The introduction of correlation functions in 1954 by van Hove allowed the separation of the scattering problem into the interactions of the neutrons with the sample and the response of the sample system to the neutron. This focus on the response of the system led to a more intuitive understanding of the neutron scattering results and is more readily theoretically calculable.

The magnetic scattering potential is significantly more complicated than the nuclear scattering potential. To describe this interaction potential, we first need to define the neutron and electron magnetic dipole moment. The neutron magnetic moment is given by

$$\boldsymbol{\mu}_n = -\gamma\mu_N\boldsymbol{\sigma}, \quad (1.45)$$

where $\gamma = 1.913$, $\mu_N = \frac{e\hbar}{2m_p}$ is the nuclear magneton (m_p is the proton mass), and $\boldsymbol{\sigma}$ is the Pauli spin-1/2 operator. The electron magnetic dipole moment is given by

$$\boldsymbol{\mu}_e = -2\mu_B\mathbf{s}, \quad (1.46)$$

where $\mu_B = \frac{e\hbar}{2m_e}$ is the Bohr magneton, and \mathbf{s} is the spin angular momentum operator of an electron. The neutron moment interacts with both the spin of the electron forming a magnetic field, as well as the magnetic field created from the orbit of the moving electron. The field at a point in space, \mathbf{R} , due to an electron with momentum, \mathbf{p} , can be written as

$$\begin{aligned} \mathbf{B} &= \mathbf{B}_s + \mathbf{B}_L \\ &= \frac{\mu_0}{4\pi} \left[\nabla \times \left(-2\mu_B \frac{\mathbf{s} \times \hat{\mathbf{R}}}{|\mathbf{R}|^2} \right) + \frac{2\mu_B}{\hbar} \frac{\mathbf{p} \times \hat{\mathbf{R}}}{|\mathbf{R}|^2} \right]. \end{aligned} \quad (1.47)$$

Therefore, the magnetic potential is given by

$$\begin{aligned} V_{\text{mag}} &= \boldsymbol{\mu}_n \cdot \mathbf{B} \\ &= \frac{\mu_0}{4\pi} \gamma\mu_N 2\mu_B \boldsymbol{\sigma} \cdot \left[\nabla \times \left(\frac{\mathbf{s} \times \hat{\mathbf{R}}}{|\mathbf{R}|^2} \right) + \frac{1}{\hbar} \frac{\mathbf{p} \times \hat{\mathbf{R}}}{|\mathbf{R}|^2} \right]. \end{aligned} \quad (1.48)$$

Plugging this in to the double differential cross-section (Eqn. (1.38)) and simplifying, we obtain

$$\frac{d^2\sigma}{d\Omega dE_f} = \frac{|\mathbf{k}_f|}{|\mathbf{k}_i|} \sum_{\lambda_i, \lambda_f} (4\pi)^2 p_{\lambda_i} |\langle \mathbf{k}_f \lambda_f | \boldsymbol{\sigma} \cdot \mathbf{Q}_\perp | \mathbf{k}_i \lambda_i \rangle|^2 \delta(\hbar\omega - (E_i - E_f)), \quad (1.49)$$

where

$$\mathbf{Q}_\perp = \sum_i e^{-i\mathbf{Q}\cdot\mathbf{r}_i} \left[\hat{\mathbf{Q}} \times (\mathbf{s}_i \times \hat{\mathbf{Q}}) + \frac{i}{\hbar|\mathbf{Q}|} (\mathbf{p}_i \times \hat{\mathbf{Q}}) \right]. \quad (1.50)$$

The sum over i is the sum over the individual electrons with position r_i and spin s_i . This is fairly complicated to compute as magnetic interactions are long-range, but it is significantly simplified for magnetically ordered crystals. One important point to note is that \mathbf{Q}_\perp is related to the Fourier transform of magnetization, but specifically probes the component of the magnetization perpendicular to the momentum transfer ($\mathbf{Q} = \mathbf{k}_f - \mathbf{k}_i$).

In practice, we fit the momentum (\mathbf{Q}) and energy (E) dependence of the magnetic structure and excitations through streamlined fitting programs, such as Fullprof and SpinW, respectively. As these require in-depth theoretical algorithms or simplifications, the discussion of such fitting will be presented in Section 1.3.

Experimental considerations

Before discussing different neutron scattering instruments and their experimental considerations, it would benefit to discuss the sources of neutrons. There are two main sources for neutron scattering with the same goal; to extract neutrons from some nuclei and direct them to the different beamlines. One way to do this is in a nuclear reactor through fission, where slow neutrons are absorbed by meta-stable ^{235}U , which then decays with many decay products, most importantly neutrons. The high energy (on the order of MeV) neutrons that are liberated need to be slowed down to both continue the reaction and to do science with. Typical condensed matter experiments are performed at meV levels to match typical interaction strengths and excitations in studied materials. At the High Flux Isotope Reactor (HFIR) at Oak Ridge National Laboratory (ORNL), this is done with a heavy water moderator through inelastic collisions. The temperature of the moderator determines the energy (and therefore wavelength) of the neutrons

described by the Boltzmann distribution. Neutrons moderated through heavy water are known as thermal neutrons ($E \sim 5 - 100$ meV), but there are also cold neutrons ($E \sim 0.1 - 10$ meV), moderated through liquid hydrogen, and hot neutrons ($E \sim 100 - 500$ meV), moderated through hot graphite. As the fission process is constantly occurring, this method of neutron production is called a continuous or steady-state source. Other steady state sources include the Institut Laue-Langevin (ILL) in France, and FRM-II in Germany.

In contrast, the spallation method produces a pulsed source. At the Spallation Neutron Source (SNS) at ORNL, an ion source produces H⁻ ions that are accelerated to ~ 1 GeV. These ions are then guided to an accumulation ring where the ion beam is bunched and intensified before being sent through a stripper foil to remove the electrons. The result is a high energy proton beam pulse that is extracted to hit a target (liquid Hg at SNS, but other heavy metals can be used), releasing 20 – 30 neutrons per target atom. Similarly to the reactor source, these neutrons are then slowed through a moderator before being guided to the different beamlines. Other spallation sources include the ISIS Neutron & Muon source in the UK, and the J-SNS in Japan.

Our neutron scattering signals can be broken into the elastic and inelastic signals. Elastic signals are that where the energy transfer of the neutron is zero ($\hbar\omega = 0$), which occurs when the neutron interacts with a static structure like the crystal lattice or a magnetically ordered lattice, called Bragg scattering. Inelastic signals ($\hbar\omega \neq 0$, schematic shown in Figure 1.13 a) explore the dynamics of a system, such as spin-wave or phonon modes in a material. One important point is that a positive energy transfer, $\hbar\omega > 0$, means that the neutron has lost energy to the system. This is defined this way because, at low temperatures, the lattice has less energy to give to the neutron, so the negative energy transfer is related to the positive energy transfer by

$$S(Q, -\omega) = e^{\frac{-\hbar\omega}{k_B T}} S(Q, \omega). \quad (1.51)$$

This is the method of detailed balance, where $e^{\frac{-\hbar\omega}{k_B T}}$ is the Boltzmann factor which acts as an intensity envelope for the negative energy transfer. One can take advantage of this relationship

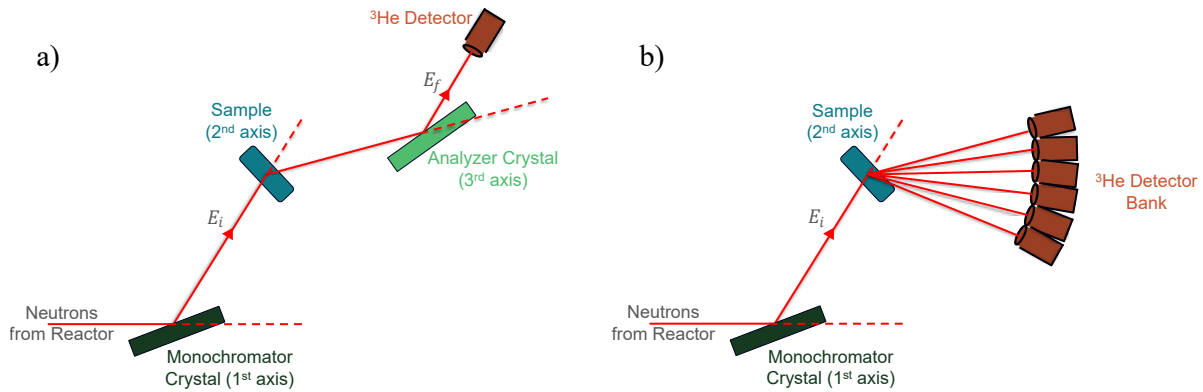


Figure 1.12: Schematics of a) a triple axis and b) diffraction beamlines at a reactor source. In both cases, the neutron interacts with a monochromator crystal to pick out the incident energy before it interacts with the sample. The scattered neutron is then energy discriminated with an analyzer crystal before being detected in a triple axis experiment, while it is energy integrated when detected in a diffraction experiment. Both types of beamlines utilize either ^3He point detectors or 2D position sensitive detectors.

to determine the effective temperature of the system, which can be useful at these ultra-low temperatures (assuming the energy resolution is good enough).

One of the first neutron scattering instruments developed was the triple-axis, aptly named for the three tuneable rotation axes it possesses. A schematic of a triple-axis instrument is shown in Figure 1.12 a). The first tuneable axis is the monochromator, a crystal with well-defined Bragg scattering such that $n\lambda = 2d \sin\theta$ determines the incoming neutron wavelength and energy incident on the experimental sample. The second axis is the sample, typically a single crystal, rotated to define the Bragg peak or point in reciprocal space being probed. Finally, the third axis is the analyzer crystal, which works in the same way as the monochromator to pick the final energy to be measured. The scattered neutrons with the desired final energy are then measured by a detector, typically ^3He gas-filled tubes which act as point detectors, although 2D position-sensitive detectors may also be utilized. Triple-axis experiments probe a specific point in (\mathbf{Q}, ω) space at a time and are therefore not ideal for broad survey-type measurements. However, triple-axis experiments are advantageous for parametric scans where an external parameter is tuned, such as temperature, field, or pressure. For example, a triple-axis spectrometer can determine the magnetic ordering temperature very accurately by measuring a specific magnetic Bragg peak as a function of temperature.

Time-of-flight (TOF) measurements, on the other hand, are more suitable for broad survey experiments. TOF takes advantage of the pulsed nature of a spallation source (or a continuous source that employs choppers), by timing how long a neutron takes to reach the detector after interacting with the sample. Assuming non-relativistic neutrons and a monochromatic incoming pulse with energy E_i and a well-known distance between the sample and detectors (L), the neutron energy transfer is

$$\hbar\omega = E_i - \frac{1}{2}m\left(\frac{L^2}{t^2}\right). \quad (1.52)$$

The scattered neutrons are detected by a 2D array of detectors surrounding the sample and the tagged time will inform about the neutron energy transfer. This method gives significantly more information per incoming neutron pulse, making it ideal for broad survey measurements, such as crystal field excitation measurements or spin-wave exploration. These measurements still require long counting times and many crystal rotations to map out a wide Q-space, and are therefore not always ideal for parametric scans.

Monochromating a pulsed beam is less trivial than using a monochromating crystal, but it can also take advantage of the pulsed nature of the beam. A velocity selector of length L is composed of twisted neutron absorbing sheets (Figure 1.13 b). It rotates at some angular speed ω_a , such that neutrons with velocity $v = L/t$ pass through according to

$$\begin{aligned} v &= \frac{\omega_a L}{\gamma}, \text{ or} \\ \lambda &= \frac{h\gamma}{mL\omega_a}, \end{aligned} \quad (1.53)$$

where γ is the twist angle. A disk chopper works similarly, where a disk is wrapped in a neutron absorbing material with small openings that allow neutrons through (Figure 1.13 c). Since the initial pulse of neutrons is a white beam, the pulse will spread in space, and as the disk chopper rotates, only the desired neutron velocity will be allowed through. Finally, a Fermi chopper

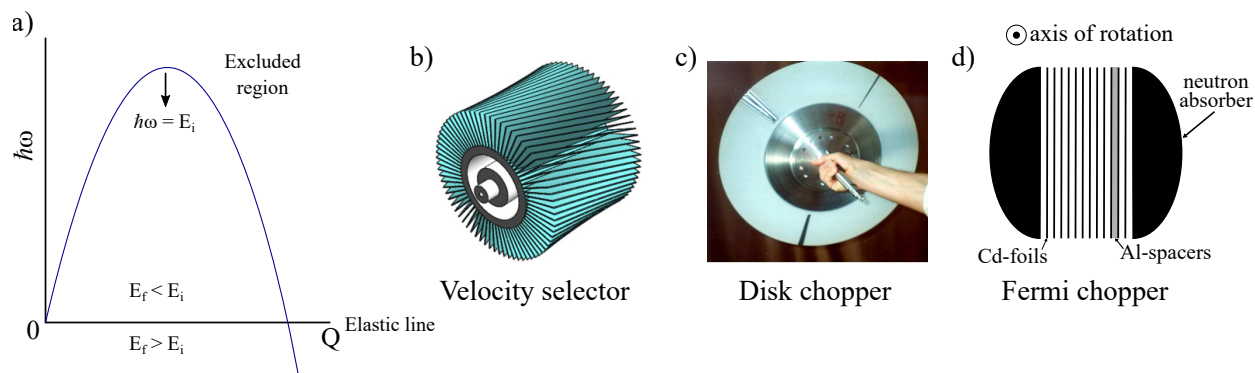


Figure 1.13: a) Simplified inelastic neutron scattering graphic which shows that a positive energy transfer corresponds to the neutron losing energy. b) The multi-blade design of a neutron velocity selector. Image credit: Ref. [9] c) A disk chopper from DCS at NIST, where the white is Gd_2O_3 , a strong neutron absorber. Image credit: nist.gov. d) A schematic of a Fermi chopper. Image adapted from Ref. [10].

may be used, which chops via a rotating collimator (axis of rotation perpendicular to the beam) surrounded by neutron absorbing material (Figure 1.13 d).

There are two types of TOF beamlines, direct geometry and indirect geometry. A direct geometry instrument requires a monochromated incoming neutron pulse and uses the time to discern the final energy of the neutron. Indirect geometry, in contrast, has an incoming white beam pulse and utilizes an analyzer to select the final neutron energy detected and is advantageous for obtaining higher energy resolution at large energy transfers. Examples of direct geometry spectrometers are the Cold Neutron Chopper Spectrometer (CNCS) at ORNL, which is optimized for low incident energies ($\sim 2 - 50$ meV) to explore quantum magnetism and excitations, and SEQUOIA at ORNL, which is optimized for a broad incident energy range ($\sim 8 - 2000$ meV) and high resolution to investigate magnetic excitations and lattice vibrations. An example of an indirect geometry spectrometer is BASIS at ORNL, which quotes an energy resolution as low as $3.5 \mu\text{eV}$ at the elastic line and is optimized to study quasi-elastic scattering to probe diffusion.

Neutron diffraction is another essential technique within neutron scattering. The set-up of diffraction experiments is the same as a triple-axis experiment, however, the analyzer is removed such that all energies contribute to the final intensity. This is an efficient way to measure Bragg peaks as the elastic scattering typically dominates the total scattering signal. Additionally, an array of detectors is typically utilized to cover a large area of Q-space at once. A schematic

of this is shown in Figure 1.12 b. In the case of the powder diffractometer POWDER (HB-2A) at ORNL, point detectors are used and the detector array must be rotated around the sample to obtain a full scattering pattern. On beamline WAND² at ORNL, a 2D position sensitive detector is utilized which provides the full Q-space pattern at once and enables faster data acquisition at the cost of resolution. As neutron diffraction integrates over the neutron energy transfer, these measurements are dominated by the elastic (static) signal and are therefore ideal for performing structure (magnetic or crystal lattice) determination measurements.

Total scattering is experimentally identical to neutron diffraction in that the final energy of the scattered neutrons is integrated over, however the analysis and application are different. Total scattering relies on performing a Fourier transform of the neutron diffraction data, taking what was once broad signals in reciprocal space (known as diffuse scattering) and turning them into sharp signals in real space. As neutron diffraction peaks result from bulk (or long-range) order, broad signals result from short-range order. In taking the Fourier transform, we can instead analyze the real space correlations. In the case of crystal structure scattering, the real space correlations can be thought of as a histogram of atomic distances, and this is called atomic pair distribution function (PDF) analysis. Total scattering is often used in nanoscale-ordered structural studies, but it has recently also been utilized for short-range *magnetic* order using a magnetic PDF (mPDF) technique. In this technique, the sign of the PDF peaks depends on the sign of the magnetic interaction (positive for FM, negative for AFM). An illustrative example of the PDF technique is shown in Figure 1.14, where two structurally disordered models are shown, but one exhibits local, short-range order. The neutron diffraction pattern shown in Figure 1.14 c) is almost identical between the two, however the local ordered structure possesses a diffuse background signal. This leads to a larger peak at the nearest-neighbor distance in the real space PDF pattern, indicative of the preference toward this short-range order. While PDF could be performed at a reactor source, the Fourier transform relies on large Q-space coverage which can only be achieved with very low-wavelength neutrons that are readily available at spallation sources.

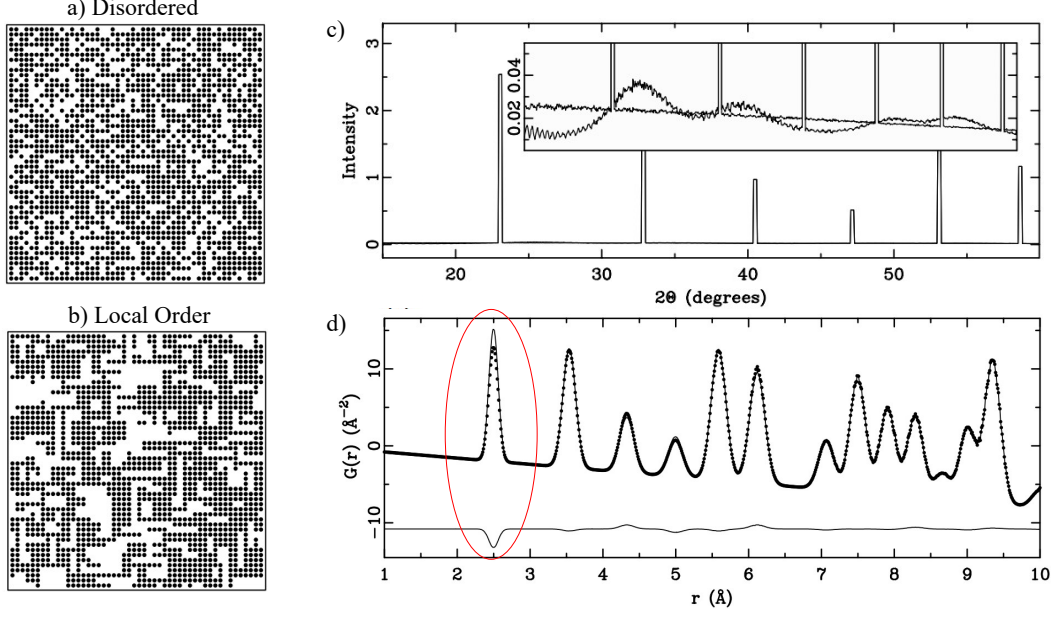


Figure 1.14: A a) random and b) locally ordered system of vacancies. c) The corresponding powder diffraction pattern, which shows that the Bragg scattering is the same from a) and b), but the local order has diffuse scattering in addition. c) The PDF of both systems, where the locally ordered system has greater intensity on the nearest-neighbor bond distance peak. Image credit: Ref. [11]

Finally, neutron spin polarization techniques are incredibly powerful in neutron scattering, but are quite challenging and complex. In our work, we utilized half-polarization analysis, so this discussion will be limited to this technique. In the 1960's, Blume and Maleyev determined the scattered neutron intensity from a polarized neutron beam to be given by

$$I = N^* N + \mathbf{M}_\perp \cdot \mathbf{M}_\perp^* + \mathbf{P} \cdot (N \mathbf{M}_\perp^* + N^* \mathbf{M}_\perp) + i \mathbf{P} \cdot (\mathbf{M}_\perp \times \mathbf{M}_\perp^*) + I_{SI}, \quad (1.54)$$

where N is the nuclear structure factor, \mathbf{M} is the magnetic structure factor, and \mathbf{P} is the neutron polarization. The first and second terms compose the nuclear and magnetic scattering, respectively, followed by interference, chiral magnetic scattering, and incoherent nuclear spin terms, respectively. In the case that the polarization is out of the scattering plane ($\mathbf{P} \parallel \hat{\mathbf{z}}$), we can write the intensity of Eqn. (1.54) in terms of the direction of incoming and outgoing polarization (where the negative polarization, \bar{z} , is achieved using a flipper) denoted with the incoming and outgoing polarization as the first and second subscripts, respectively:

$$\begin{aligned}
I_{zz} &= N^* N + M_{\perp z} M_{\perp z}^* + N M_{\perp z}^* + N^* M_{\perp z} + \frac{1}{3} I_{\text{SI}} \\
I_{\bar{z}\bar{z}} &= N^* N + M_{\perp z} M_{\perp z}^* - N M_{\perp z}^* - N^* M_{\perp z} + \frac{1}{3} I_{\text{SI}} \\
I_{z\bar{z}} &= M_{\perp x} M_{\perp x}^* + M_{\perp y} M_{\perp y}^* + i(M_{\perp x} M_{\perp y}^* - M_{\perp y} M_{\perp x}^*) + \frac{2}{3} I_{\text{SI}} \\
I_{\bar{z}z} &= M_{\perp x} M_{\perp x}^* + M_{\perp y} M_{\perp y}^* - i(M_{\perp x} M_{\perp y}^* - M_{\perp y} M_{\perp x}^*) + \frac{2}{3} I_{\text{SI}}.
\end{aligned} \tag{1.55}$$

Half-polarization occurs when the incoming beam is polarized, but the polarization of the scattered beam is not discerned (or vice versa). Therefore, we can sum together intensity of the scattered up and down neutron polarizations, to obtain

$$\begin{aligned}
I_z \text{ (or } I_+) &= I_{zz} + I_{z\bar{z}} \\
&= N^* N + \mathbf{M}_{\perp} \cdot \mathbf{M}_{\perp}^* + N M_{\perp z}^* + N^* M_{\perp z} + i(M_{\perp x} M_{\perp y}^* - M_{\perp y} M_{\perp x}^*) + I_{\text{SI}} \\
I_{\bar{z}} \text{ (or } I_-) &= I_{\bar{z}\bar{z}} + I_{\bar{z}z} \\
&= N^* N + \mathbf{M}_{\perp} \cdot \mathbf{M}_{\perp}^* - N M_{\perp z}^* - N^* M_{\perp z} - i(M_{\perp x} M_{\perp y}^* - M_{\perp y} M_{\perp x}^*) + I_{\text{SI}}
\end{aligned} \tag{1.56}$$

The utility of Eqn. (1.56) comes from taking the sum and difference of the half-polarized measurements, which either cancel the nuclear and magnetic structure terms or the interference and chiral terms. For field-polarized paramagnet, ferro- or ferri-magnets, where $\mathbf{m} \parallel \mathbf{P} \parallel \hat{\mathbf{z}}$, Eqn. (1.56) is simplified further to

$$\begin{aligned}
I_{\pm} &= N^* N + M_{\perp} M_{\perp}^* \pm P_0(N M_{\perp}^* + N^* M_{\perp}) + I_{\text{SI}} \\
&\approx (N \pm M)^2
\end{aligned} \tag{1.57}$$

Therefore, for effective ferromagnetic materials with small magnetic signal, half-polarized neutron scattering can be beneficial to increase the magnetic intensity (compared to unpolarized scattering in which $I \approx N^2 + M^2$).

1.3 Theoretical Techniques

1.3.1 Describing Magnetic Structures

All materials in nature possess some kind of symmetry. The repeating lattice in a crystal by definition means it possesses discrete (i.e. breaks continuous) translational symmetry. To determine the structure of a type of magnetic order, it is useful to mathematically describe the structure in terms of the symmetry it obeys. There are two commonly utilized methods to do this, through either magnetic space groups [85, 86, 87] or through irreducible representations [75, 86, 88, 89, 90], both of which will be presented individually. Before discussing these, it is beneficial to discuss the basics of symmetry.

A symmetry operation maps a point from an initial location to a new location. There are four primary symmetry operations: translation, rotation, reflection, and inversion. A mirror (reflection) is a 2D plane which inverts one Cartesian coordinate, rotation is with respect to a 1D axis which acts to change two Cartesian coordinates, and an inversion occurs about a point (0D) that will change all three Cartesian coordinates. Within a perfect lattice, there are four types of rotational symmetry that is consistent with a repeating lattice. Those are 2-, 3-, 4-, and 6-fold rotations (180° , 120° , 90° , and 60° , respectively).

When symmetry operations are combined together, they can form a set of self-consistent symmetry elements, known as a group (G). The requirements to form a group are that 1) there exists an identity element (E) such that for all $g_i \in G$, $g_i E = g_i$, 2) for each element $g_i \in G$ there exists an inverse element $g'_j \in G$ such that $g_i g'_j = E$, 3) the group is closed under multiplication, so $g_i g_j = g_k$, where $g_i, g_j, g_k \in G$, and finally 4) the group follows the associative law of multiplication, i.e. for $g_i, g_j, g_k \in G$, $g_i (g_j g_k) = (g_i g_j) g_k$. In crystallography, the minimal self-consistent symmetry groups that leave the crystal unchained are known as *point groups* when translation is not included, and *space groups* when translation is included. There are 32 point groups, and 230 space groups, that fall into seven categories (from lowest to highest symmetry): triclinic, monoclinic, orthorhombic, trigonal, tetragonal, hexagonal, and cubic.

Magnetic Space Groups

Assume the magnetic structure can be defined by an axial vector (or pseudo-vector), $\mathbf{S}(r)$, which contains each magnetic atom in the crystal. After applying a symmetry operation, g , $\mathbf{S}(r)$ has transformed either to $\mathbf{S}'(r)$ or remains unchanged. The approach using magnetic symmetry defines the set of symmetry operations, G , that leave $\mathbf{S}(r)$ invariant.

From the 230 paramagnetic (crystallographic, or “parent”) space groups, the magnetic space groups split this further by the introduction of time reversal symmetry. Time reversal is a non-spatial symmetry operation, unlike those listed previously, and acts to reverse the current flow of the electrons and therefore reverse the magnetic dipole direction. This addition forms a total of 112 magnetic point groups and 1651 magnetic space groups. This is clearly too many to sort through by hand to find the magnetic symmetry that best fits your data. For this reason, we utilize the Bilbao Crystallographic Server and specifically the program MAXMAGN [91, 92, 93, 94]. This tool has the user input the parent space group and propagation vector, \mathbf{k} , found from neutron diffraction, and MAXMAGN will find all possible magnetic space groups with maximal symmetry consistent with this propagation vector. This typically limits the number of magnetic structures to sort through to only a handful. Furthermore, if none of the models reasonably fit the diffraction data, the program can explore lower symmetry structures that could be caused by subtle structural distortions.

While this approach is intuitive and straightforward, the biggest drawback is that it only applies to commensurate magnetic structures, where the magnetic cell is a rational multiple of the crystallographic unit cell. For incommensurate magnetic structures, one needs to use magnetic superspace groups [86]. Additionally, the magnetic space group method can be challenging for the initial determination of the magnetic structure (especially when the structure is “unconventional”, see Chapter 2) and better suited for classification once the structure is known.

Representation theory

Representation analysis is a much less intuitive but more general method of determining a material’s magnetic structure. A representation is simply a matrix group (set of square matrices)

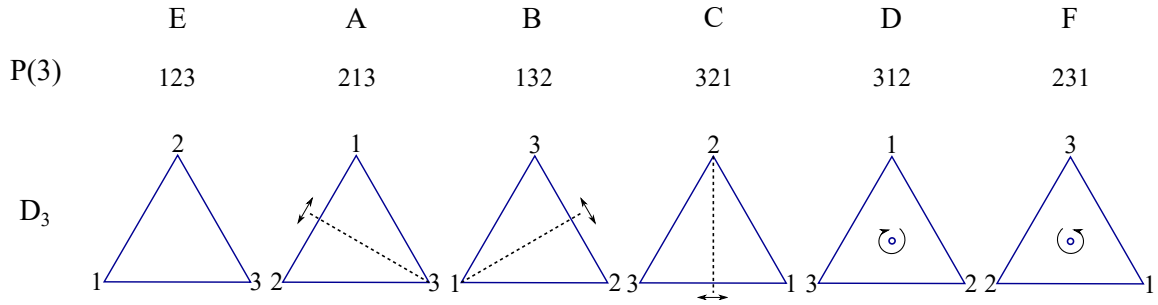


Figure 1.15: Isomorphic groups: the permutation group, $P(3)$, which is a permutation of three numbers, and the symmetry group, D_3 , for an equilateral triangle.

Table 1.2: The three irreducible representations of the permutation group $P(3)$. Γ_1 is the trivial group, and it is from these irreps that all reducible representations of $P(3)$ are composed of.

	E	A	B	C	D	F
Γ_1	(1)	(1)	(1)	(1)	(1)	(1)
$\Gamma_{1'}$	(1)	(1)	(1)	(-1)	(-1)	(-1)
Γ_2	$\begin{pmatrix} 1 & 0 \\ 0 & 1 \end{pmatrix}$	$\begin{pmatrix} 1 & 0 \\ 0 & -1 \end{pmatrix}$	$\begin{pmatrix} -\frac{1}{2} & \frac{\sqrt{3}}{2} \\ \frac{\sqrt{3}}{2} & \frac{1}{2} \end{pmatrix}$	$\begin{pmatrix} -\frac{1}{2} & -\frac{\sqrt{3}}{2} \\ -\frac{\sqrt{3}}{2} & \frac{1}{2} \end{pmatrix}$	$\begin{pmatrix} -\frac{1}{2} & \frac{\sqrt{3}}{2} \\ -\frac{\sqrt{3}}{2} & -\frac{1}{2} \end{pmatrix}$	$\begin{pmatrix} -\frac{1}{2} & -\frac{\sqrt{3}}{2} \\ \frac{\sqrt{3}}{2} & -\frac{1}{2} \end{pmatrix}$

of symmetry operations, such that, when acting on a point, it will transform that point according to the symmetry it follows. More explicitly: assume g is a symmetry operation in the space group G and it operates on a spin \mathbf{S}_j where $j = (1, 2 \dots 3n)$ to include the x, y, z directions as well as n symmetry equivalent points. We can write this symmetry operation as

$$g\mathbf{S}_j = \sum_k D(g)_{kj} \cdot \mathbf{S}_k, \quad (1.58)$$

where $D(g)$ is the matrix transpose of the transformation matrix of the spins. We call $D(g)$ a $3n \times 3n$ representation of G and it is usually reducible, meaning it can be written in block formation composed of multiple irreducible representations (*irreps*). A simple example of the concept of representations is the symmetry group of an equilateral triangle. First, we define “isomorphic” as having a correspondence between two groups, so an equilateral triangle symmetry group (D_3) is isomorphic to the permutation group of three numbers ($P(3)$) as is shown in Figure 1.15. The matrix representations form a group which is also isomorphic to the symmetry or permutation group (see Table 1.2).

We can use matrices to represent the different space group symmetry operations in crystallography by

$$g = \{h|t\} = \begin{bmatrix} h_{11} & h_{12} & h_{13} & t_1 \\ h_{21} & h_{22} & h_{23} & t_2 \\ h_{31} & h_{32} & h_{33} & t_3 \\ 0 & 0 & 0 & \pm 1 \end{bmatrix} \quad (1.59)$$

where h is a symmetry operator, t is a translation vector, and the ± 1 indicates the handedness of the symmetry operation. For a magnetic structure with propagation vector \mathbf{k} , the group G_k (with parent group G) is composed of all symmetry operators $g_k \in G$ that leave \mathbf{k} invariant. Next, the operations of all symmetry elements $g_k \in G_k$ on a spin can be described by a matrix, Γ_{mag} (like $D(g)$ above). The magnetic representation Γ_{mag} is composed of irreps Γ_ν , where

$$\Gamma_{\text{mag}} = \sum_{\nu} n_{\nu} \Gamma_{\nu}, \quad (1.60)$$

which describe the transformation properties. We find n_{ν} through

$$n_{\nu} = \frac{1}{n(G_k)} \sum_{g_k \in G_k} \chi_{\Gamma_{\text{mag}}}(g_k) \chi_{\Gamma_{\nu}}(g_k) \quad (1.61)$$

where χ is called the character, and is the trace of the matrix representation for the specific symmetry operation. To actually find the decomposition of Γ_{mag} into the irreps, we utilize a character table and these useful properties:

- The number of irreps is equal to the number of classes (classes are the groupings of similar symmetry operations, e.g. rotations of π).
- $\sum_{\nu} l_{\nu}^2 = m$, where l is the dimension of Γ_{ν} and m is the order (number of symmetry elements) of the group. When this is combined with the previous point, it is *usually* possible to uniquely determine the dimensions of the irreps.

- The trivial (identity) representation is a full row of 1's in the character table.
- The first column of the character table is the trace of the identity matrix for each representation and is therefore the dimension of the irrep.
- $\sum_k N_k \chi^{\Gamma_\nu}(g_k) = 0$, where N_k is the number of elements in the class, can be utilized to determine the trace of all symmetry elements for a single representation.
- There exist orthogonality theorems between the rows and columns in a character table that can be taken advantage of to fill out the remainder of the character table.

The goal of representational analysis is to form the magnetic configurations from linear combinations of basis functions that transform according to the irreducible representation of G_k . Now that the magnetic representation is determined, we need to find the basis vectors associated with the irreps through

$$\psi_\nu^{j\lambda} = \sum_{g_k \in G_k} \Gamma_\nu^\lambda(g_k) e^{i\mathbf{k}\mathbf{a}_{g_k j}} \det(h) h_{\alpha\alpha'} \delta_{j',g_k j} \phi_\alpha \quad (1.62)$$

where $\lambda = 1 \dots d$ and d is the dimension of the irrep, j runs through equivalent positions in the unit cell, $\alpha = x, y, z$, the ϕ_α are test functions, δ is a Kronecker delta function that is 1 if g_k transforms j to j' and is 0 otherwise, and finally $e^{i\mathbf{k}\mathbf{a}_{g_k j}}$ is a phase factor included in case the symmetry operator translates outside the unit cell (\mathbf{a} is known as a “returning vector”). Once these are determined, we find the magnetic structure by a linear combination,

$$S_{k_j} = \sum_{\lambda n} c_\nu^{\lambda n} \psi_\nu^{\lambda n}, \quad (1.63)$$

and the coefficients c can be fit to the neutron diffraction data. In the case of a second order transition, Landau theory states that the lower symmetry group must be a sub-group of the higher symmetry group and only one irrep can contribute to the magnetic structure, which greatly limits the number of basis vector coefficients to fit.

Similarly to the magnetic space group method, we rarely do these calculations by hand and instead utilize one of the many computational programs designed for the representational analysis method. Some examples of these tools are KAREP, SARA_h, MODY, BasIreps, and ISOTROPY, to name a few. For our work in Chapter 2, we used SARA_h [88, 95] to find the irreps and basis vectors applicable to $\text{K}_3\text{Er}(\text{VO}_4)_2$ by inputting the propagation vector, space group, and magnetic atom position.

Chapter 2

Pseudo-spin versus magnetic dipole moment ordering in the isosceles triangular lattice material

$K_3Er(VO_4)_2$

2.1 Context

This chapter consists of the paper *Pseudo-spin versus magnetic dipole moment ordering on the isosceles triangular lattice material $K_3Er(VO_4)_2$* , which was published in Physical Review B in 2020. The full reference is:

D. R. Yahne, L. D. Sanjeeva, A. S. Sefat, B. S. Stadelman, J. W. Kolis, S. Calder, and K. A. Ross, Phys. Rev. B **102**, 104423 (2020)¹.

The supplemental information and ongoing (unpublished) work are shown in sections 2.4 and 2.5 respectively. This work aimed to fully characterize the newly synthesized isosceles triangular lattice magnet $K_3Er(VO_4)_2$, and discovered an unexpected magnetic order with alternating magnetic dipole-active and magnetic dipole-silent layers. We put forward the hypothesis that the unique order may be due to suppressed out-of-plane pseudo-spin order from the strongly XY nature of $K_3Er(VO_4)_2$. The ongoing work aims to test this hypothesis.

Contributions

Single crystal samples were grown by L. D. Sanjeeva under supervision of A. S. Sefat. Crystals used for powder diffraction were grown by B. S. Stadelman with assistance from L. D. Sanjeeva and J. W. Kolis. Heat capacity, susceptibility, magnetization, and powder x-ray diffraction

¹Copyright by 2020 American Physical Society

measurements were performed by D. R. Yahne with support from K. A. Ross. Powder neutron scattering was performed by D. R. Yahne and K. A. Ross with assistance from beamline scientist S. Calder. Subsequent analysis of scattering data was analyzed and simulated by D. R. Yahne with support from K. A. Ross and S. Calder. The paper was written by D. R. Yahne and K. A. Ross.

2.2 Paper abstract

Spin- $\frac{1}{2}$ antiferromagnetic triangular lattice models are paradigms of geometrical frustration, revealing very different ground states and quantum effects depending on the nature of anisotropies in the model. Due to strong spin orbit coupling and crystal field effects, rare-earth ions can form pseudo-spin- $\frac{1}{2}$ magnetic moments with anisotropic single-ion and exchange properties. Thus, rare-earth based triangular lattices enable the exploration of this interplay between frustration and anisotropy. Here we study one such case, the rare-earth double vanadate glaserite material $\text{K}_3\text{Er}(\text{VO}_4)_2$, which is a quasi-2D isosceles triangular antiferromagnet. Our specific heat and neutron powder diffraction data from $\text{K}_3\text{Er}(\text{VO}_4)_2$ reveal a transition to long range magnetic order at 155 ± 5 mK which accounts for all $R \ln 2$ entropy. We observe what appears to be a coexistence of 3D and quasi-2D order below T_N . The quasi-2D order leads to an anisotropic Warren-like peak profile for $(hk0)$ reflections, while the 3D order is best-described by layers of antiferromagnetic b -aligned moments alternating with layers of zero moment. Our magnetic susceptibility data reveal that Er^{3+} takes on a strong XY single-ion anisotropy in $\text{K}_3\text{Er}(\text{VO}_4)_2$, leading to vanishing moments when *pseudo-spins* are oriented along c . Thus, the magnetic structure, when considered from the pseudo-spin point of view could comprise of alternating layers of b -axis and c -axis aligned antiferromagnetism.

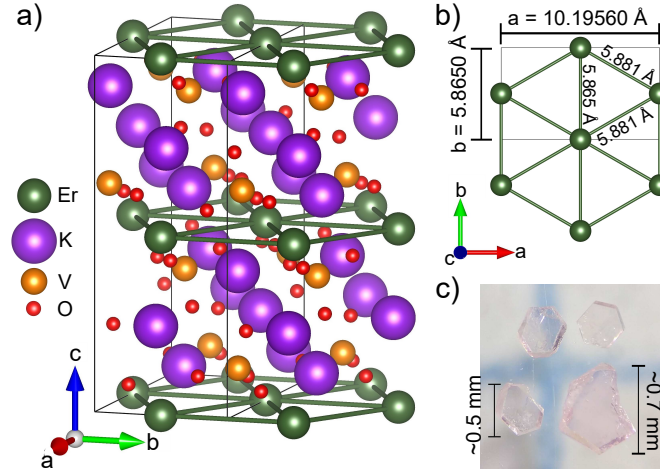


Figure 2.1: a) Crystal structure of monoclinic $\text{K}_3\text{Er}(\text{VO}_4)_2$ (space group $C2/c$) showing layers of 2D isosceles triangular Er^{3+} lattices. b) The 2D isosceles triangular Er^{3+} lattice, with bond lengths and unit cell size shown (not shown, $c = 15.2050 \text{ \AA}$). c) Typical single crystals of $\text{K}_3\text{Er}(\text{VO}_4)_2$ which were co-aligned for magnetization and susceptibility measurements.

2.3 Research article

Introduction

Magnetic frustration has been of interest in condensed matter physics due to the presence of competing interactions which often leads to exotic properties. A two-dimensional (2D) triangular lattice with antiferromagnetically (AFM) interacting Ising spins is the simplest example of geometrical frustration. Wannier found in 1950 that this model has a macroscopically degenerate ground state and the frustration suppresses order down to zero temperature [96]. A Quantum Spin Liquid (QSL) state, which exhibits quantum entanglement and fractionalized excitations, was first envisioned by Anderson to exist on a 2D triangular Heisenberg AFM (HAFM) [47]. It is now understood that interactions on the 2D triangular HAFM model leads to 120° order [97, 98, 99], but exchange interaction anisotropies or lattice distortions can lead to other interesting phenomena. For example, the isosceles triangular AFM Cs_2CuCl_4 was found to be a 1D spin chain and is an example of "dimensional reduction" induced by frustration [100, 101], and anisotropic exchange models on the triangular lattice have been proposed to host QSL phases [52, 56, 102, 103, 104].

Rare-earth based frustrated materials have become of interest due to strong spin orbit coupling and crystal electric field (CEF) effects which can lead to $S_{\text{eff}} = \frac{1}{2}$ doublets (pseudo-spin- $\frac{1}{2}$) and anisotropic effective exchange models based on these pseudo-spin- $\frac{1}{2}$ moments. This makes them ideal to study quantum phases arising from anisotropic exchange. The relationship between the observed magnetic dipole moments (μ_i) and the pseudo-spin- $\frac{1}{2}$ operators (S_i) is given by the g -tensor: $\mu_i = g_{ii} S_i$ ². Depending on the details of the CEF Hamiltonian, the ground state doublet forming the pseudo-spins can have certain g components become vanishingly small (or in some cases, identically zero due to the symmetry) and thus no appreciable magnetic dipole moment associated with that pseudo-spin direction [33]. In the case where the symmetry prevents any dipole moment, these pseudo-spin directions are associated with higher multipoles, such as quadrupoles [106, 107] or octupoles[34, 108, 109, 110].

In terms of the search for quantum magnetic phases based on rare earth ions, Yb^{3+} has received the most attention. For instance, $\text{Yb}_2\text{Ti}_2\text{O}_7$, was proposed as a quantum spin ice material [37, 111, 112, 113] but was later shown to be an unusual ferromagnet with continuum-like scattering [114, 115, 116] that appears to arise from phase competition and non-linear spin wave effects [117, 118, 119]. Meanwhile the triangular lattice YbMgGaO_4 was proposed as a QSL but may instead exhibit a random valence bond state due to Mg/Ga site disorder [49, 50, 51, 52, 120, 121, 122]. Frustrated Er^{3+} materials are also of interest, and the pyrochlores ($\text{Er}_2\text{B}_2\text{O}_7$, B = Ti, Sn, Ge, Pt, etc.) [14, 16, 38, 123, 124, 125, 126, 127, 128, 129] have enjoyed the most attention, but other frustrated geometries realized by Er^{3+} are just beginning to be explored [130, 131]. Here we study the isosceles triangular material $\text{K}_3\text{Er}(\text{VO}_4)_2$ and show that it has strong XY single ion anisotropy with an unconventional magnetic ground state described by alternating ordered layers of antiferromagnetic "magnetic dipole active" and "magnetic dipole silent" pseudo-spins.

²This assumes the g_{ii} values are those obtained from the square root of the eigenvalues of the G tensor [105], so the moment directions defined here by i are along the eigenvectors of that tensor

$\text{K}_3\text{Er}(\text{VO}_4)_2$ is a member of the rare-earth double vanadate glaserite family, $\text{K}_3\text{RE}(\text{VO}_4)_2$, where RE = (Sc, Y, Dy, Ho, Er, Yb, Lu, or Tm). Previous studies on rare-earth double *phosphate* glaserites ($\text{K}_3\text{RE}(\text{PO}_4)_2$) have shown that there can exist structural transitions between trigonal and lower symmetry structures of these compounds (i.e. monoclinic) [132, 133]. While previous reports of $\text{K}_3\text{Er}(\text{VO}_4)_2$ describe it in terms of a trigonal space group ($P\bar{3}m1$) at room temperature [134], we have found from powder and single crystal x-ray diffraction, as well as low temperature neutron diffraction, that a monoclinic structure (space group $C2/c$), shown in Figure 2.1 (a) & (b), is appropriate for our samples at all measured temperatures, similar but not identical to $\text{K}_3\text{Er}(\text{PO}_4)_2$ (which forms in space group $P2_1/m$).

Experimental methods and results

The crystal growth of monoclinic $\text{K}_3\text{Er}(\text{VO}_4)_2$ phase involved two steps. First, powder targeting a stoichiometric product of $\text{K}_3\text{Er}(\text{VO}_4)_2$ was performed using K_2CO_3 , Er_2O_3 and $(\text{NH}_4)\text{VO}_3$. A total of 3 g of components were mixed in a stoichiometric ratio of 3:1:4 and ground well using an Agate motor and pestle. The powder mixture was then pressed into pellets and heated to 750°C for 80 hours. After the reaction period, the resulted pellets were crushed, ground and checked the purity using powder X-ray diffraction (PXRD). According the PXRD, majority phase was matched with the $\text{K}_3\text{Er}(\text{VO}_4)_2$ (PDF No. 00-51-0095) with impurities of K_3VO_4 and ErVO_4 . In the second step, the resulted $\text{K}_3\text{Er}(\text{VO}_4)_2$ powder was treated hydrothermally to obtain single crystals.

Hydrothermal synthesis was performed using 2.75-inch long silver tubing that had an inner diameter of 0.375 inches. After silver tubes were welded shut on one side, the reactants and the mineralizer were added. Next, the silver ampules were welded shut and placed in a Tuttle-seal autoclave that was filled with water in order to provide appropriate counter pressure. The autoclaves were then heated to 600°C for 14 days, reaching an average pressure of 1.7 kbar, utilizing ceramic band heaters. After the reaction period, the heaters were turned off and the autoclave cooled to room temperature. Crystals were recovered by washing with de-ionized

water. In a typical reaction 0.4 g of $\text{K}_3\text{Er}(\text{VO}_4)_2$ powder was mixed with a mineralizer solution of 0.8 mL of 10 M K_2CO_3 .

Crystals of $\text{K}_3\text{Er}(\text{VO}_4)_2$, used for magnetism and heat capacity measurements, were physically examined and selected under an optical microscope equipped with a polarizing attachment. Room temperature single crystal structures were characterized using a Bruker D8 Venture diffractometer Mo $K\alpha$ radiation ($\lambda = 0.71073 \text{ \AA}$) and a Photon 100 CMOS detector. The Bruker Apex3 software package with SAINT and SADABS routines were used to collect, process, and correct the data for absorption effects. The structures were solved by intrinsic phasing and subsequently refined on F^2 using full-matrix least squares techniques by the SHELXTL software package[135]. All atoms were refined anisotropically.

We performed heat capacity measurements from 8 K down to 50 mK (Figure 2.2) on a 0.41 ± 0.05 mg single crystal sample (examples shown in Figure 2.1 (c)) using a Quantum Design PPMS with dilution refrigerator insert. We employed two measurement techniques, a typical quasi-adiabatic thermal relaxation measurement with temperature rise $\Delta T/T$ of 2%, as well as “long pulse” measurements where $\Delta T/T$ can be as large as 400%, as described in Ref. [77]. We find a sharp transition at $T_N = 155 \pm 5$ mK, much lower than the Curie-Weiss temperature (discussed later), indicating that this system is frustrated as expected, with a frustration parameter of $f = \theta_{CW}/T_N \approx 20$. The total $C_p(T)$ (not lattice subtracted) reveals a broad peak around 10 K, the shape of which cannot be purely attributed to a power law contribution from acoustic phonon modes, as well as a gradual release of entropy on cooling from 1 K down to 155 mK, at which temperature a sharp anomaly is observed. The high temperature peak near 10 K is indicative of a low-lying excited CEF multiplet with energy of about 2 meV. The entropy change between 50 mK to 2 K accounts for all the entropy expected from a Kramers CEF ground state doublet ($R \ln 2$ per mole Er^{3+} , see inset of Figure 2.2). Less than 30% of this entropy is released via the sharp anomaly, indicating that short range correlations develop over a broad temperature range above the ordering transition. This is commonly found in low dimensional and frustrated magnets, where ordering is suppressed but is eventually triggered by some subleading energy scale in the

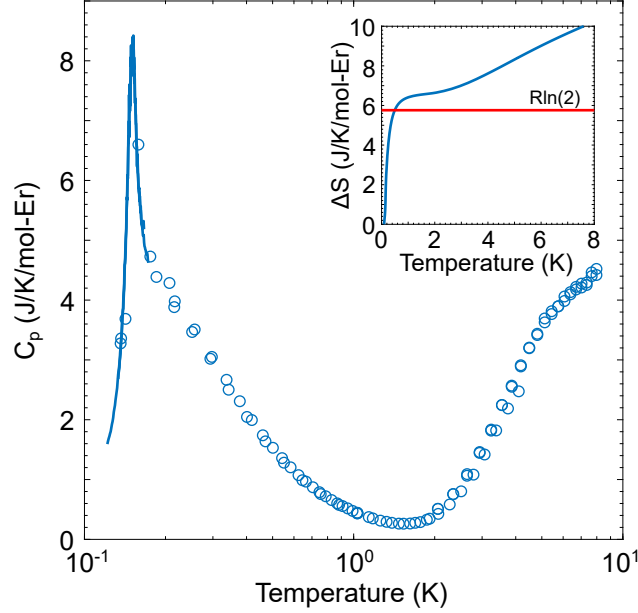


Figure 2.2: Single crystal heat capacity in zero magnetic field. The open circles represent the adiabatic measurements, while the solid line represents the large ΔT measurements. A sharp magnetic transition is observed at 155 mK, with the asymmetric shape on the high temperature side of the transition indicating a build-up of low dimensional short range correlations. (Inset) Entropy calculated from C_p vs. T with the $R \ln 2$ limit shown, indicating an isolated $S_{\text{eff}} = \frac{1}{2}$ system below 1 K.

Hamiltonian (such as inter-layer interactions in the case of quasi-2D systems) [136]. The quasi-2D nature of the magnetism in $\text{K}_3\text{Er}(\text{VO}_4)_2$ is also confirmed by neutron powder diffraction to coexist with 3D order below T_N , as discussed later.

The temperature dependent magnetic susceptibility of $\text{K}_3\text{Er}(\text{VO}_4)_2$ was measured down to 1.8 K in a 100 Oe field (Figure 2.3 (a)) using the MPMS XL Quantum Design SQUID magnetometer on 1.60 ± 0.05 mg and 1.04 ± 0.10 mg of co-aligned single crystals, aligned in the $H \perp c$ and $H \parallel c$ directions respectively. For magnetic fields $H \perp c$, we find net antiferromagnetic interactions shown by the negative Curie-Weiss temperature $\theta_{CW} \approx -3$ K obtained by fitting between 2 and 10 K (although this value is highly dependent on the exact fitting range used due to crystal field effects), similar to YbMgGaO_4 with $\theta_{CW} \approx -4$ K. The magnetic susceptibility $\chi_{\parallel c}$ is an order of magnitude less than $\chi_{\perp c}$, indicating a strong XY nature of the g -tensor of Er^{3+} in this material. Magnetization measurements (Figure 2.3 (b)), taken at 1.8 K in a magnetic field up to 5 T, corroborate that $\text{K}_3\text{Er}(\text{VO}_4)_2$ is a strongly XY system due to the large saturation magnetization

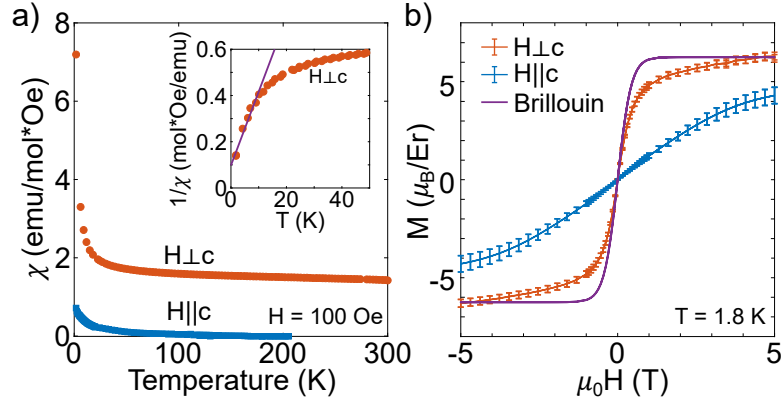


Figure 2.3: a) Magnetic susceptibility of co-aligned single crystals with the field aligned perpendicular and parallel to the c -axis, showing $\chi_{\perp c}$ is larger than $\chi_{\parallel c}$ by a factor of ~ 10 . (Inset) Low temperature fit of inverse susceptibility used to find the $H_{\perp c}$ Curie-Weiss temperature $\theta_{CW} \approx -3$ K. b) Magnetization of co-aligned single crystals at 1.8 K. For $H_{\parallel c}$, significant field-induced mixing of the next highest CEF level produces an enhanced moment in the field.

for $M_{\perp c}$. Neither $M_{\perp c}$ nor $M_{\parallel c}$ follow a Brillouin function expected for a simple paramagnet, suggesting that there is significant mixing of the higher CEF states causing the response to be non-paramagnetic. Due to field induced mixing of the excited CEF levels, the saturation magnetization is not a good indicator of the zero-field g -tensor for either direction. Regardless of the CEF mixing, the magnetization $M_{\parallel c}$ starts with a low g -value near zero field, consistent with a small g -value in the c -axis.

Neutron powder diffraction was performed on the HB-2A beamline at Oak Ridge National Laboratory's (ORNL) High Flux Isotope Reactor (HFIR). Approximately 2.5 g of crystals were ground into a fine powder, placed into a copper sample can and filled with 10 atm of He gas at room temperature, a technique shown to enable sample thermalization of loose powders below 1 K [137]. Diffraction patterns were obtained from 10 K down to 50 mK, with collimator settings open-open-12', and a Ge(113) monochromator provided an incident wavelength of $\lambda = 2.41$ Å. The patterns were collected over a Q -range of $0.18 \text{ \AA}^{-1} < Q < 4.64 \text{ \AA}^{-1}$ ($4^\circ < 2\theta < 126^\circ$) with count times of 2 hours per scan.

Analysis of the powder diffraction data was performed using the FullProf software suite which implements the Rietveld refinement method [138]. The 10 K data was used to refine

Table 2.1: Irreducible representation and basis vector composition for space group $C2/c$ with $k=(1,0,0)$ found using the *SARAh* Representational Analysis software. The atoms are defined according to $m_1:(0.5,0,0.5)$ and $m_2:(0.5,0,0)$.

IR	BV	Basis Vector Components					
		m_{1a}	m_{1b}	m_{1c}	m_{2a}	m_{2b}	m_{2c}
Γ_1	ψ_1	2	0	0	-2	0	0
	ψ_2	0	2	0	0	2	0
	ψ_3	0	0	2	0	0	-2
Γ_3	ψ_4	2	0	0	2	0	0
	ψ_5	0	2	0	0	-2	0
	ψ_6	0	0	2	0	0	2

the nuclear structure with contributions from the copper cell and aluminum windows masked. Magnetic peaks which could not be indexed within the $K_3Er(VO_4)_2$ unit cell emerged between 10 K and 400 mK, indicating the presence of magnetic impurities in the sample, which were unable to be identified. These impurities are likely to be from by-products produced during the crystal synthesis, which are easy to avoid for single crystals measurements, but is impractical to completely remove for the large sample mass needed for neutron powder measurements. To remove the impurity signal from the magnetic structure analysis, we subtracted the 400 mK data from the 50 mK data, leaving only contributions from $K_3Er(VO_4)_2$ magnetic Bragg peaks (Figure 2.5 (a)). The magnetic peaks indexed gave an ordering wavevector of $k=(1,0,0)$, for which the decomposition of the magnetic representation into irreducible representations (IR's) is $\Gamma_{mag} = 3\Gamma_1^{(1)} + 0\Gamma_2^{(1)} + 3\Gamma_3^{(1)} + 0\Gamma_4^{(1)}$ for a magnetic atom at site (0.5, 0, 0.5) found using the *SARAh* Representational Analysis software[95] (Kovalev tables). Γ_1 is composed of basis vectors $\psi_{1,2,3}$, and Γ_3 is composed of basis vectors $\psi_{4,5,6}$. Basis vectors $\psi_{2,4,6}$ have antiferromagnetic (AFM) spin arrangements in the ab plane which are ferromagnetically (FM) correlated along the c -axis (i.e. every layer is identical), with moments pointing along the b , a , and c axes, respectively. $\psi_{1,3,5}$ are AFM in the ab plane as well as along the c -axis, with moments pointing along the a , c , and b axes, respectively. The summary of these basis vectors and their components for each site is in Table 2.1 and shown in Figure 2.4.

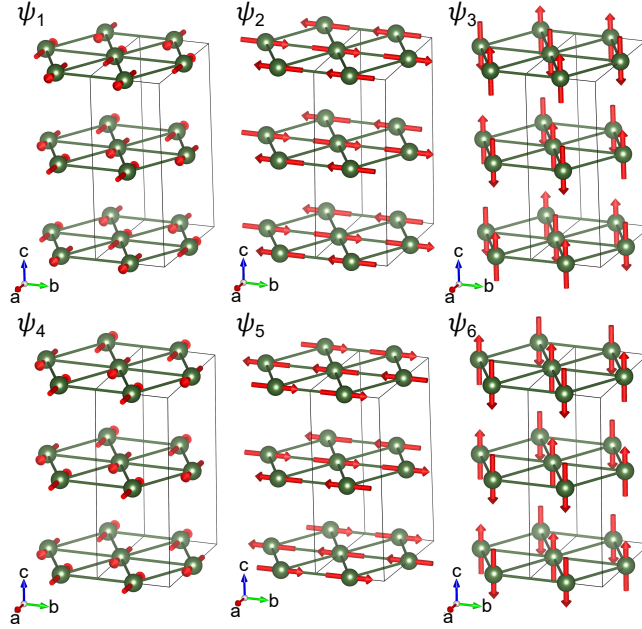


Figure 2.4: Visualizations of the basis vectors for space group $C2/c$ with $k=(1,0,0)$: $\psi_{1,2,3}$ from Γ_1 and $\psi_{4,5,6}$ from Γ_3 . All basis vectors are antiferromagnetic in the ab -plane. Basis vectors $\psi_{1,3,5}$ are also antiferromagnetic along c , while basis vectors $\psi_{2,4,6}$ are ferromagnetic along c (each layer is identical).

We attempted to fit the magnetic scattering within a single IR, which would be expected for a second order phase transition [89], however, no linear combination of the basis vectors restricted to a single IR came close to reproducing the observed magnetic structure (Appendix 2.4). It should also be noted that all fits lacked perfect agreement with the intensity of all of the magnetic peaks simultaneously, specifically with respect to the (100) reflection. The shape of the (100) peak does not follow the typical pseudo-Voigt peak shape, and is instead reminiscent of the Warren line-shape for random 2D layered lattices [139], having an asymmetric base that extends further to high Q . In a 2D random layer lattice, where no correlations exist between layers, the structure factor for (hkl) zone centers is expected to be zero [139], in contrast to the $(hk0)$ zone centers, which are non-zero and will have this asymmetric shape. For *quasi-random* 2D layers with some short range correlations between planes, intensity is expected at (hkl) reflections, but peaks will have suppressed intensities and will in principle be broadened compared to a peak arising from long range 3D order [140, 141, 142].

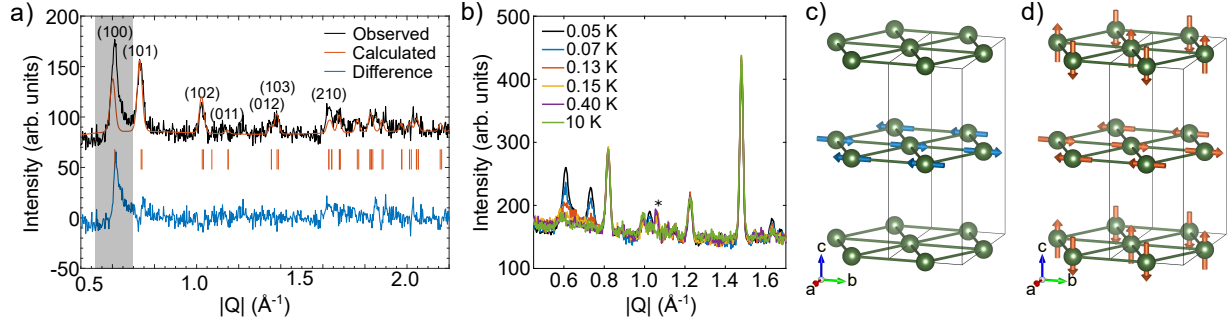


Figure 2.5: a) Neutron diffraction pattern (black) taken on a 2.5 g powder sample on beamline HB-2A at HFIR (ORNL). Magnetic peaks were found from subtracting the 400 mK pattern from the 50 mK pattern to remove impurity signals. A coexistence of 2D and 3D order was found, and thus the Warren-like (100) peak was not included in the fit. The fit to the 3D order (red) and calculated difference (blue) is shown for the best fit using the Fullprof software, which was a linear combination of equal contributions of basis vectors ψ_2 (from Γ_1) and ψ_5 (from Γ_3). b) Temperature dependence of magnetic Bragg peaks below the transition temperature of 155 mK shows the onset of 2D and 3D order occurs at the same temperature. Magnetic impurity peaks were found between 10 K and 400 mK, denoted with a star. c) The magnetic structure found from neutron diffraction pattern shows layers of b -aligned moment alternating with layers of zero moment, proposed to be due to the strong XY nature of $\text{K}_3\text{Er}(\text{VO}_4)_2$ ($g_z \sim 0$). d) The proposed *pseudo-spin* structure, alternating between layers of b -aligned pseudo-spin and layers of c -aligned pseudo-spin.

As a pure Warren line-shape did not accurately reproduce the (100) reflection, we explored the 2D nature of this material by performing a numerical simulation for the (100) reflection to determine the in-plane and out-of-plane correlation lengths (see Appendix 2.4 for details). The simulation of the (100) peak produces an out-of-plane correlation length that is inconsistent with the (hkl) magnetic Bragg peaks, which are almost resolution-limited, indicating there is instead a coexistence of 2D and 3D order in $\text{K}_3\text{Er}(\text{VO}_4)_2$. The origin of this coexistence is unknown, but similar effects have been observed in other materials and is speculated to be caused by structural inhomogeneities [143, 144]. However, as shown in Figure 2.5(b), the 2D and 3D peaks have similar temperature dependence, which indicates that even if there are inhomogeneous regions of 3D and quasi-2D order, they onset at the same temperature.

Due to the contributions from 2D and 3D correlations to the (100) peak, it was excluded from the fit of the 3D magnetic structure. Our refined magnetic structure is given by equal contributions from basis vectors ψ_2 (from Γ_1) and ψ_5 (from Γ_3), with basis vector coefficients 0.90(2). This leads to moments along b that add together in one layer and cancel in the other

layer due to the FM and AFM spin correlations along the c -axis (Figure 2.5 (c)). It should be noted that less prominent contributions of basis vector ψ_6 , which adds small c -aligned moment to the layers, could be included without affecting the fit drastically. From the susceptibility data though, little to no moment is expected out-of-plane, so the ψ_6 contribution is expected to be small or zero. Comparing the calculated diffraction pattern to the data (Figure 2.5 (a)), it is clear that the $(hk0)$ peaks are under-estimated. This is as expected, since the $(hk0)$ peaks contain significant contributions from the 2D correlations in the material that are not captured by the model.

Discussion

The refined magnetic structure, in conjunction with the heat capacity, which produces the full $R \ln 2$ entropy change upon integrating C_p/T from 50 mK to 1 K, suggests that $\text{K}_3\text{Er}(\text{VO}_4)_2$ is in a fully ordered state, yet the refined structure implies the absence of ordered moments every other layer. Quantum fluctuations could in principle produce a reduced or zero moment on some layers, however, a simpler explanation seems to be possible by considering the inferred g -tensor and the likely pseudo-spin order. We suggest that the likely *pseudo-spin* ordering structure involves the 2D triangular layers alternating between AFM ordered layers with moment along \vec{b} and \vec{c} (Figure 2.5 (d))³. Such a spin structure is not likely to be obtained from purely XY exchange interactions. Yet, because of the strong XY *single-ion* nature of this material ($g_z \sim 0$), the layers with the pseudo-spins pointing along the c -axis would carry approximately zero dipole moment and thus appear to be disordered (or strongly reduced) according to probes that are sensitive only to dipole magnetic moments, such as neutron scattering. This result emphasizes a subtle point which is sometimes misunderstood; the g -tensor anisotropy of pseudo-spin- $\frac{1}{2}$ systems does not need to be the same as the exchange anisotropy.

Similar effects are at play in some rare earth pyrochlores, where the the XY part of the pseudo-spin carries a quadrupolar [106, 107] or octupolar [34, 108, 109, 110] moment but no

³this *pseudo-spin* state can be visualized using a combination of $\Psi_{2,5,6}$ and $-\Psi_3$ (Figure 2.4)

dipole moment. However, even “conventional” Kramers’ doublets which transform as dipoles in all directions can have very small g -values in certain directions, which is the case for Er^{3+} in $\text{Er}_2\text{Sn}_2\text{O}_7$ [38]. Due to the low point symmetry at the Er^{3+} site (triclinic) of $\text{K}_3\text{Er}(\text{VO}_4)_2$, the ground state CEF doublet is most likely to be a conventional Kramers’ doublet. This could in principle be investigated by an analysis of the CEF levels in the material, however we note that the point symmetry for Er^{3+} in $\text{K}_3\text{Er}(\text{VO}_4)_2$ is triclinic, leading to 15 symmetry-allowed Steven’s parameters which are unlikely to be determined uniquely by experiment or calculation.

Conclusions

We have performed an extensive study of the magnetic properties of a member of the rare-earth double vanadate glaserite materials, which form 2D isosceles (or equilateral, in the case of the trigonal polymorphs) triangular lattices. We found an antiferromagnetic transition in $\text{K}_3\text{Er}(\text{VO}_4)_2$ at 155 mK despite a relatively strong AFM interaction of 3 K inferred from Curie-Weiss analysis (frustration parameter $f \sim 20$). Susceptibility measurements reveal this material to have strong XY g -tensor anisotropy, although field-induced coupling to a low-lying CEF level near ~ 2 meV (inferred from $C_p(T)$) hinders a quantitative estimate of the g -tensor via magnetization. The magnetic structure is likely comprised of large AFM magnetic dipole moments ordering along the b axis direction in every other layer, and magnetic dipole suppressed pseudo-spin order along c in the other layers. In this light, $\text{K}_3\text{Er}(\text{VO}_4)_2$ thus appears to be one of the clearest examples in which pseudo-spin order results in zero dipole moments. Inelastic neutron scattering studies of $\text{K}_3\text{Er}(\text{VO}_4)_2$ could help to validate this model, and could also reveal the inferred low lying CEF level. Furthermore, the measurement of the g -tensor via Electron Paramagnetic Resonance could help to confirm our proposed model. Further studies of other rare earth glaserites, particularly in their trigonal structural polymorphs, would be intriguing, as they could be promising materials for discovering new quantum magnetic phases due to their pseudo-spin- $\frac{1}{2}$ angular momentum and strong frustration.

2.4 Supplemental material

Sample preparation

Table 2.2: Crystallographic data of $K_3Er(VO_4)_2$ determined by single crystal X-ray diffraction.

Empirical formula	$K_3Er(VO_4)_2$
Formula weight (g/mol)	514.44
Crystal system	monoclinic
Crystal dimensions, mm	0.10 x 0.02 x 0.02
space group, Z	$C2/c$ (no.15), 4
T, K	298
a, Å	10.1956(4)
b, Å	5.8650(2)
c, Å	15.2050(6)
β , °	90.12(1)
Volume, Å ³	909.21(6)
D(calc), g/cm ³	3.758
μ (Mo K α), mm ⁻¹	12.543
F(000)	940
T _{max} , T _{min}	1.0000, 0.8169
2 θ range	2.679 – 24.990
reflections collected	10581
data/restraints/parameters	781/0/67
final R [$I > 2\sigma(I)$] R ₁ , R _{w2}	0.0372, 0.1144
final R (all data) R ₁ , R _{w2}	0.0374, 0.1144
GoF	1.086
largest diff. peak/hole, e/ Å ³	1.760/ – 1.155

Crystallographic data for monoclinic $K_3Er(VO_4)_2$ was determined using single crystal x-ray diffraction, the details of which are outlined in the main text, and the results are shown in Table 2.2. A large number of single crystals of $K_3Er(VO_4)_2$ were ground into a powder for neutron diffraction using a mortar and pestle. Due to the large number of crystals necessary to achieve a substantial mass for neutron scattering, the crystals were ground in three batches, which were x-rayed separately and then again after the batches were combined. Powder X-ray diffraction was performed on a Bruker D8 Discover Davinci diffractometer from $10^\circ < 2\theta < 60^\circ$ for approximately 1 second per 0.02° . The PXRD pattern was fit using TOPAS Reitveld refinement, and

was found to be in agreement with the single crystal XRD, as well as no preferred orientation or peak broadening were found, indicating the crystals were ground sufficiently. Impurity peaks were unable to be matched with any of the expected by-products (ErVO_4 , Er_3O_2 , etc), and are likely to be from by-products introduced during the hydrothermal synthesis. The powder was then shipped to ORNL where it was placed into a copper sample can. The sample can contains a piece of indium within the He filling line to allow the can to be filled with 10 atm of He gas and then crimped at the indium, thereby containing the gas.

Low-temperature nuclear structure

Neutron powder diffraction data was performed at 10 K, which was used to determine the low temperature lattice parameters. The neutron data corroborates the monoclinic space group best describes the crystal structure (Figure 2.6). As expected, we find small impurity peaks in the nuclear data, denoted by stars, and do not find any evidence of preferred orientation. Upon decreasing the temperature to 400 mK, *magnetic* impurities were found, specifically evidenced by a peak at $|Q| = 1.06 \text{ \AA}$ that increases in intensity between 10 K and 400 mK, and does not increase intensity further upon cooling to 50 mK (Figure 2.5 (b)). Due to the different onset temperature and no signatures of a transition between 10 K and 400 mK in the heat capacity data, this is not believed to be a secondary phase of $\text{K}_3\text{Er}(\text{VO}_4)_2$. To remove this unknown impurity, we subtracted the 400 mK data from the 50 mK data, leaving only the magnetic scattering signal to be analyzed.

Quasi-2D simulation

The first magnetic peak, (100), did not have the expected pseudo-Voigt peak shape and instead follows more of Warren line-shape for random 2D layer lattices. The Warren line-shape comes from rods of scattering in reciprocal space, centered at (hk) . Initially, we attempted to fit the (100) peak with a Warren function [139, 145], but the Warren fit over-estimated the high Q tail (Figure 2.7 (a)). In addition, if the 2D layers were random with no correlations along the c -axis, only $(hk0)$ peaks would have a non-zero structure factor in contrast to (hkl) peaks which

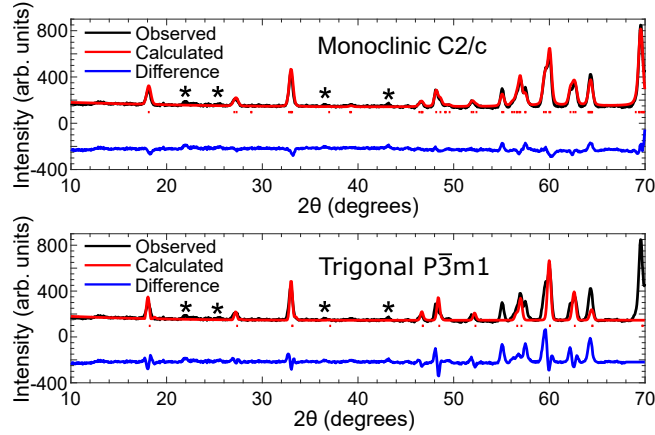


Figure 2.6: Nuclear structure of $\text{K}_3\text{Er}(\text{VO}_4)_2$ found with neutron scattering at 10 K. The trigonal structure clearly does not describe the crystal structure in contrast to the monoclinic structure. The impurity is also seen in small peaks unable to be fit by either structure, denoted by stars.

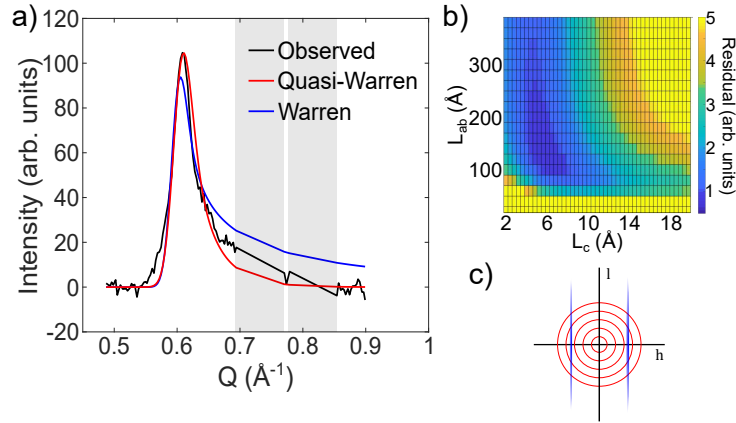


Figure 2.7: a) Warren fit and quasi-Warren simulation compared with the 50 mK data (not background subtracted). The (hkl) and nuclear peaks were masked (grey boxes). The Warren fit overestimates the high- Q side of the asymmetric peak. b) Residual plot for varying combinations of correlation lengths along the ab and c directions. c) 2D visualization of simulation in the $h0l$ plane, where blue ellipses are the scattering intensities and the red circles are the integrated areas simulating the powder diffraction.

would have zero intensity. This suggests that the layers could have some short-range correlations along c , thus would be *quasi*-random. Quasi-random 2D layers would still possess asymmetrical $(hk0)$ peaks, while (hkl) peaks would be suppressed and broadened but non-zero. We used a numerical simulation to estimate the in-plane and out-of-plane correlations and fit the (100) asymmetric peak, which shows that this is *not* the case, as discussed next. Thus we infer that the magnetic correlations are a possibly inhomogeneous mixture of 2D and 3D order.

The numerical simulation was performed by creating a 3D Gaussian ellipse (instead of rods) at zone centers in reciprocal space using the unit cell parameters found from the 10 K neutron diffraction (Figure 2.7 (c)). The variables of this ellipse were the standard deviations in the ab and c directions which are related to the correlations in the ab plane, L_{ab} , and the correlations between planes, L_c , respectively by the equation $L = \sqrt{2 \ln 2} / \sigma$. A radial integral was performed to simulate the powder averaged neutron diffraction pattern, the result of which was then scaled by a Lorentz factor (geometrical correction) and the magnetic form factor. This was then convolved with the instrument resolution, estimated by the FWHM of a nearby nuclear peak. The peak height was scaled to match the data since the intensity is arbitrary. The results compared with the Warren fit are shown in Figure 2.7 (a).

The simulation finds a range of correlation lengths fit the data well (Figure 2.7 (b)), but a best fit estimates correlation lengths along the c axis $L_c \approx 6 \text{ \AA}$ (approximately half a unit cell), while correlations in the ab plane $L_{ab} \approx 120 \text{ \AA}$ (more than 20 unit cells). When these correlation lengths are applied to an (hkl) peak, we find the peak would be much broader and significantly more suppressed than what we observe. Thus, the 2D and 3D order must be coexisting and onset at the same temperature.

Magnetic structure

We attempted to fit the magnetic structure using a single IR, as it was not clear if the transition found in heat capacity was a first- or second-order transition. Examples of those fits are shown in Figure 2.8. Both fits of individual IR's had peaks which were not seen in the scattering signal, while the accepted fit (combination of ψ_2 from Γ_1 and ψ_5 from Γ_3) does not show any spurious peaks. In the scenario where the magnetic structure is a combination of more than one IR, it follows that the transition must be first-order.

The fit may also be described in terms of magnetic space groups. Using this approach gives two magnetic space groups that are maximally allowed, $Pc21/c$ and $Pc2/c$. As these only have 1 Er site, it is not possible to recreate the magnetic structure only using one magnetic space group, similarly to what we find using the irreducible representation analysis. However, a subgroup of

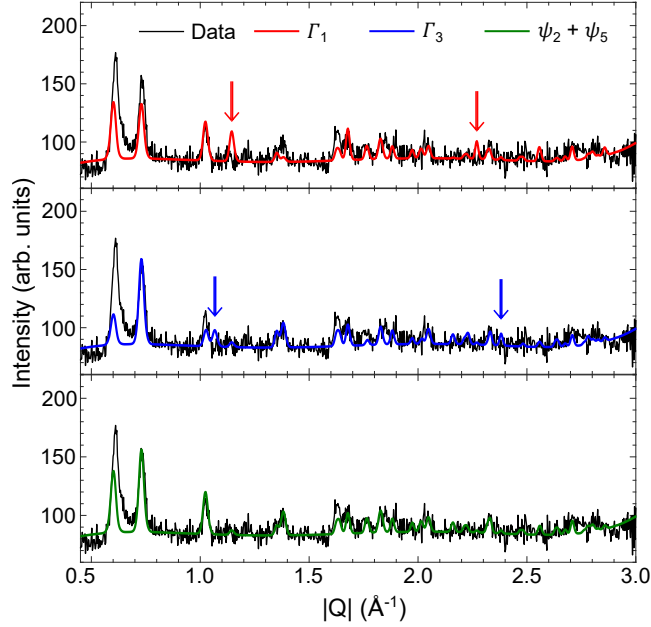


Figure 2.8: Examples of fits using a single irreducible representation. Both Γ_1 and Γ_3 fits give peaks not seen in the data, shown by arrows. Therefore, the best fit comes from a linear combination of Γ_1 and Γ_3 's basis vectors, ψ_2 and ψ_5 respectively.

lower symmetry could be used, namely the magnetic space group $P\bar{1}$ which has 2 inequivalent Er sites and would be able to recreate the found magnetic structure. This would imply some sort of subtle structural distortion beyond the limits of the measurements performed. This is consistent with our observation that two IR's must be mixed to account for the observed Bragg intensity. Such a mixed-IR magnetic structure can only arise if the symmetry is lower than assumed, which could happen at a first order transition.

The data was fit at multiple temperatures and the total moment was able to be extracted as a function of temperature, shown in Figure 2.9 to be approximately $4\mu_B$. Due to the low point density of the total moment as a function of temperature, it is difficult to fit the order parameter equation, but we have included a guide to the eye. The total moment found is lower than the saturated moment of $6.2\mu_B$ found from magnetization, but we know the saturated moment will be increased by the field-induced mixing of the low lying crystal field level.

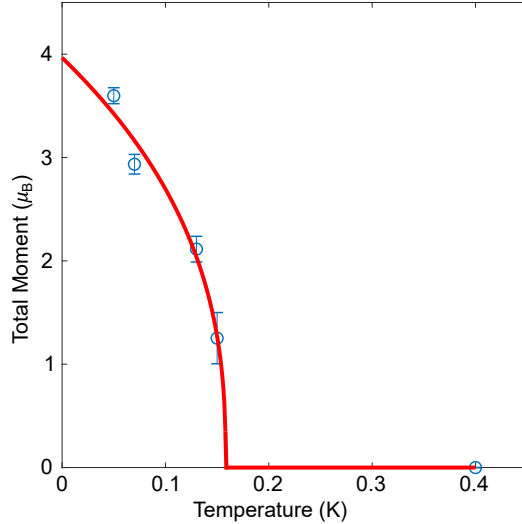


Figure 2.9: Total moment as a function of temperature. Red line serves as an order parameter guide to the eye, note this is not a fit.

Paper acknowledgements

We thank Gang Chen and Ovidiu Garlea for useful discussions. This research used resources at the High Flux Isotope Reactor, a DOE Office of Science User Facility operated by the Oak Ridge National Laboratory. Work performed on synthesis, crystal growth, and x-ray diffraction at Clemson University was funded by DOE BES Grant No. DE-SC0014271. DRY, KAR, and JWK acknowledge funding from the Department of Energy award DE-SC0020071 during the preparation of this manuscript.

2.5 Ongoing work

The goal of our ongoing work is find evidence of our claim that $g_z \approx 0$, confirming the the possible origin of the unique magnetic structure. Typically, we could perform electron paramagnetic resonance (EPR) measurements to extract the g-tensor, however, this is not easily accomplished in this instance due to the low-lying crystal field doublet. This type of measurement would require ultra-low temperatures (sub 1 K), which we do not have access to with our EPR system. Therefore, we explore this using alternative techniques, namely rotation

magnetization, CEF measurements through inelastic neutron scattering, and local magnetization measurements using half-polarized neutron diffraction.

Rotation magnetization

From the magnetization and susceptibility data presented in the preceding sections, the anisotropy is unclear due to the ambiguity of applied field direction for $M_{\perp c}$. For this reason, we took on a rotation magnetization measurement using a Quantum Design MPMS3 with a horizontal rotator. Single crystals were aligned using the standard and thin film mount to probe the ab- and ac-planes respectively. A schematic of this alignment is shown in Figure 2.10. The ab-plane was mounted such that the flat (c-axis) side of the crystal was affixed to the mount with GE-varnish, and the crystal was aligned to the a-axis (such that the a-axis starts perpendicular to the field). The ac-plane was mounted on a quartz plate using GE-varnish with the c-axis perpendicular to the plane of the plate. This plate was then attached to the standard mount, and the crystal was aligned to the c-axis (such that the c-axis starts perpendicular to the field). The crystal was rotated a full 360° and back with 5° steps (Note, due to slip of the mount, the forward and backward rotations are shifted. For this reason, we have excluded the backwards rotation.).

The results of the rotation magnetization measurements with an applied field of 5 T are shown in Figure 2.10 c). The first feature to note is the hump that occurs approximately every 90° in the ab-plane and only at 90° and 270° in the ac-direction. The cause of this signal is unknown, but similar features have been found in unrelated compounds using the same instrument, so it is unlikely to be intrinsic to $\text{K}_3\text{Er}(\text{VO}_4)_2$. Because of this feature, we have included a guide-to-the-eye for the ab-direction. We can compare these results to our previously measured magnetization (Figure 2.3) at 5 T, and this is shown by the horizontal lines in Figure 2.10 c). We find good agreement between the ab-plane rotation and $M_{\perp c}$, as expected since the $M_{\perp c}$ was some average of the ab-plane. The data shows that there is only a slightly larger moment in the b-direction than the a-direction, and thus the single-ion anisotropy is likely not the only

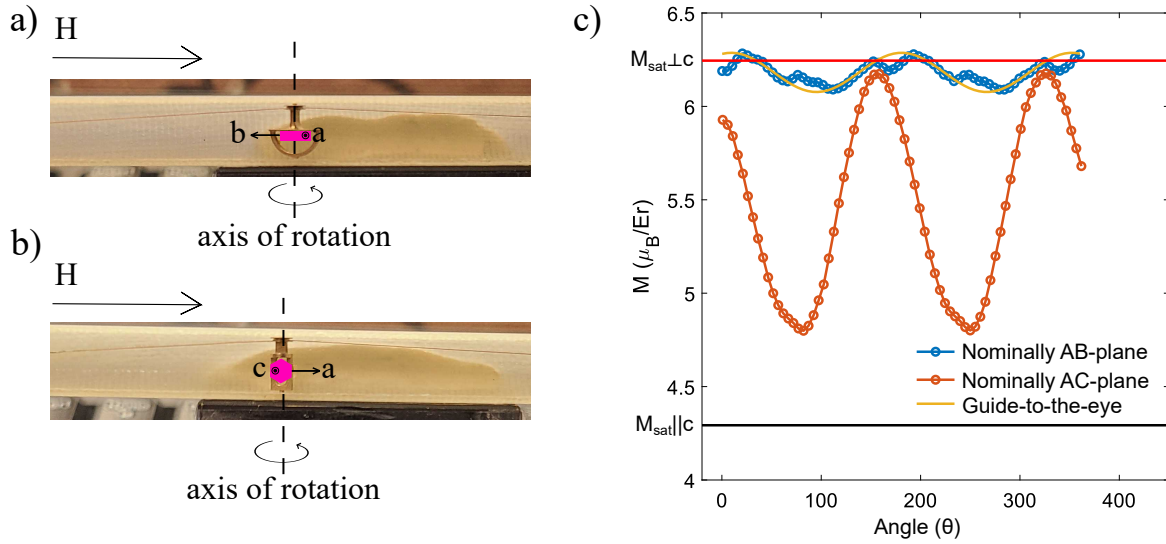


Figure 2.10: Crystal orientation for rotation magnetization measurements using a) a thin film mount to probe the magnetization within the ab-plane and b) a standard mount to probe the ac-plane. c) Rotation magnetization results, including a guide-to-the-eye for the ab-plane results due to a signal of unknown origin. We have also included the saturation magnetization values at 5 T found previously (Figure 2.3 b).

cause of the b-aligned ordered moment layers and points instead to the underlying cause to be due to exchange anisotropy.

In contrast, we do *not* find a good agreement between the ab- and ac-planes, as we expect these curves to be equal at $M_{||a}$ at the peak of the ac-plane measurement and the trough of the ab-plane measurement. Additionally the ac-plane c-axis measurement and $M_{||c}$ (from Figure 2.3 b) are not in agreement. It is likely that the samples torqued during the measurement, as the initial magnetization is unequal to the following peak. In future measurements, the samples will be affixed with a stronger adhesive (ex: CrystalbondTM) in between flat quartz plates. In the meantime, while we cannot fully corroborate our previous magnetization data, the general trend that the c-axis moment (and thus g-value) is smaller than the a-axis still holds true.

Crystal field measurements

To understand the magnetic single-ion anisotropy in $K_3Er(VO_4)_2$, it is necessary to explore the CEF interactions from the surrounding crystalline environment. CEF measurements were carried out on approximately 2 g of powder $K_3Er(VO_4)_2$ utilizing the SEQUOIA beamline, located at the SNS in Oak Ridge National Laboratory. Point charge (PC) calculations, using only

the surrounding O^{2-} environment, suggested that all eight (including the ground state) crystal field levels would be below 50 meV. Therefore, data was collected with incident neutron energies $E_i = 200, 80, 60, 20, 11, 8,$ and 4 meV (elastic energy resolution of 5.8, 2.5, 1.8, 0.5, 0.3, 0.2, and 0.055 meV, respectively) in high resolution mode, at temperatures $T = 5, 20, 50, 100,$ and 200 K. The measurements were repeated with the empty can for background subtraction. Low energy measurements were taken to reveal the low-lying CEF level expected near 2 meV from PC calculations and heat capacity measurements. Due to this low-lying CEF level, the temperature dependence is necessary to allow us to discern excitations from the ground state, which will decrease in intensity with increasing temperature, from excitations from an excited level, which will increase in intensity as the excited level begins to populate. The 200 meV measurement serves to catch any unexpected high-energy levels, as well as to look for higher multiplet transitions. All spectra were processed with the Mslice program [146], and fits to the CEF Hamiltonian utilized the PyCrystalField python code [21].

The $E_i = 20$ and 80 meV spectra at 5 K are shown in Figure 2.11 a) and c), with temperature dependent cuts along Q (intensity vs. energy) shown in Figure 2.11 b) and d) (Q -space integration range denoted by red box). Clear CEF levels can be seen around 1.5, 7, 11, and 12 meV, shifted to slightly lower energies than predicted by the PC model. In contrast, we do not see evidence of high energy CEF levels, expected in the region of 30 – 50 meV. It is not clear if this absence is due to an absence of CEF levels or if the intensity is overshadowed by the apparent phonon contributions identified by the increase in intensity proportional to Q^2 . We performed cuts over various energy integration windows to find evidence of the intensity decreasing with Q before the phonon modes, but this was not elucidating. Future work could aim to model the phonon background in order to explore these high energy levels, however, for the present work and modeling, we moved forward by making no assumptions about the location of these "missing" levels.

The triclinic point group symmetry of $K_3Er(VO_4)_2$ makes it difficult to find a unique fit to the 15 Steven's parameters of the CEF Hamiltonian, Eqn. (1.9), as the system is significantly

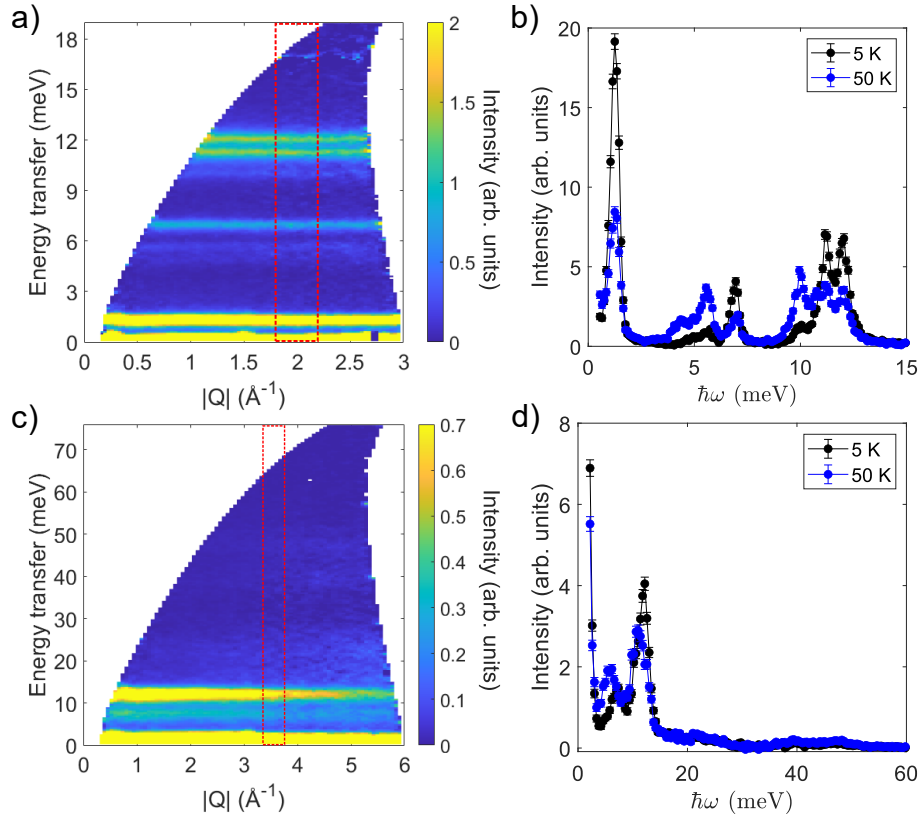


Figure 2.11: a) Powder neutron spectrum with an incident energy of 20 meV at 5 K. Crystal field excitations are clearly visible, including a low-lying level near 1.5 meV. b) Temperature dependent cut of INS data, with integration range shown in a) by the red box. c) Powder neutron spectrum with an incident energy of 80 meV at 5 K. No CEF transitions in the 40 meV range are seen. d) Temperature dependent cut of INS data, with integration range shown in c).

underconstrained. However, as is shown in Figure 2.12 c), the structure of the single ion Er-O in the monoclinic polymorph is similar to that of the trigonal polymorph (with trigonal D_{3d} point group symmetry), with a continuous symmetry measure of approximately 0.09. In the case of trigonal symmetry, the CEF Hamiltonian has only 6 unique B_l^m Steven's parameter values to fit, and thus we can start our fits by approximating the symmetry to be trigonal. Within our fit, we defined a residual function to match both the intensity vs. energy plot at $E_i = 20$ meV and the eigenvalues found by fitting the data with Gaussian peaks (making no assumption about the order of eigenvalues). These fits were able to reproduce the locations of the peaks (and therefore CEF levels), but were unable to accurately reproduce the relative intensities of said

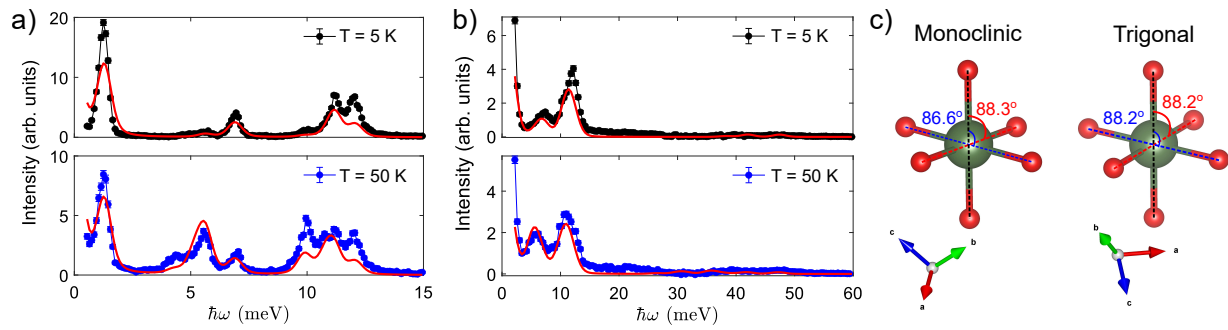


Figure 2.12: Energy vs. intensity cuts from a) 20 meV and b) 50 meV incident energy measurements. The red line indicates the CEF fit with the trigonal simplification. c) The difference in the oxygen cage around the Er^{3+} ion in the monoclinic and trigonal space groups that motivates the point group simplification.

peaks. However, we can use this as a starting point to estimate the g -tensor, which gives $g_{xy} \sim 8.4\mu_B$ and $g_z \sim 3.3\mu_B$.

Chapter 3

Understanding reentrance in frustrated magnets: the case of the $\text{Er}_2\text{Sn}_2\text{O}_7$ pyrochlore

3.1 Context

This chapter consists of the paper *Understanding Reentrance in Frustrated Magnets: The Case of the $\text{Er}_2\text{Sn}_2\text{O}_7$ Pyrochlore*, which was published in Physical Review Letters in 2021. The full reference is:

D. R. Yahne, D. Pereira, L. D. C. Jaubert, L. D. Sanjeewa, M. Powell, J. W. Kolis, Guangyong Xu, M. Enjalran, M. J. P. Gingras, and K. A. Ross, Phys. Rev. Lett. **127**, 277206 (2021)⁴.

The supplemental information and ongoing (unpublished) work are shown in sections 3.4 and 3.5 respectively. In this work, we explored the phase diagram of $\text{Er}_2\text{Sn}_2\text{O}_7$ through a variety of theoretical techniques and exposed the underlying mechanisms of reentrance in this material.

Contributions

Single crystal samples were synthesized by L. D. Sanjeewa, M. Powell and J. W. Kolis. All heat capacity measurements were performed by D. R. Yahne under the supervision of K.A. Ross. D. R. Yahne and K. A. Ross measured the powder neutron diffraction pattern with assistance from beamline scientist G. Xu. Monte Carlo simulations were performed by L. D. C. Jaubert, and mean-field theory calculations were performed by D. Pereira and M. J. P. Gingras, with assistance from M. Enjalran. The paper was written and edited by D. R. Yahne, D. Pereira, L. D. C. Jaubert, M. Enjalran, M. J. P. Gingras, and K. A. Ross.

⁴Copyright by 2021 American Physical Society

3.2 Paper abstract

Reentrance, the return of a system from an ordered phase to a previously encountered less-ordered one as a controlled parameter is continuously varied, is a recurring theme found in disparate physical systems, yet its microscopic cause is often not investigated thoroughly. Here, through detailed characterization and theoretical modeling, we uncover the microscopic mechanism behind reentrance in the strongly frustrated pyrochlore antiferromagnet $\text{Er}_2\text{Sn}_2\text{O}_7$. We use single crystal heat capacity measurements to expose that $\text{Er}_2\text{Sn}_2\text{O}_7$ exhibits multiple instances of reentrance in its magnetic field B vs temperature T phase diagram for magnetic fields along three cubic high symmetry directions. Through classical Monte Carlo simulations, mean field theory and classical linear spin-wave expansions, we argue that the origins of the multiple occurrences of reentrance observed in $\text{Er}_2\text{Sn}_2\text{O}_7$ are linked to soft modes. These soft modes arise from phase competition and enhance thermal fluctuations that entropically stabilize a specific ordered phase, resulting in an increased transition temperature for certain field values and thus the reentrant behavior. Our work represents a detailed examination into the mechanisms responsible for reentrance in a frustrated magnet and may serve as a template for the interpretation of reentrant phenomena in other physical systems.

3.3 Research article

Within the field of magnetism, frustration refers to a system's inability to simultaneously satisfy all of its energetic preferences. Strong frustration can result in a variety of exotic phenomena such as spin liquids, spin ice, emergent quasiparticles, topological phases and order-by-disorder [2, 33, 101, 147, 148, 149, 150]. Most of the research focus in this area over the past thirty years has been devoted to investigating the physics near zero temperature, considering finite temperatures as a necessary *modus operandi* to search for signatures of the low-energy properties. However, even when subject to high frustration, a majority of frustrated magnetic materials ultimately develop long-range order or display spin-glass freezing at a nonzero critical temperature T_c , albeit often at a very low one compared to the spin-spin interactions. In this context, it

therefore seems natural to ask what behavior near T_c may be a witness of the zero-temperature ground state physics. This is particularly important when T_c is just above the experimental baseline temperature, so that temperatures which are low relative to T_c cannot be reached. Here we precisely consider such a situation, as arises in the $\text{Er}_2\text{Sn}_2\text{O}_7$ pyrochlore antiferromagnet, and which provides an opportunity to study a recurrent aspect of frustrated magnetic systems observed at nonzero temperature: reentrance [113, 151, 152, 153, 154, 155, 156, 157, 158].

Reentrance occurs when a system, after having developed an ordered phase of some sort, returns to its original less-ordered (e.g. paramagnetic) state as some parameter (e.g. temperature, field, pressure, stoichiometry) is continuously varied. Reentrance has been found in spin glasses [159, 160], liquid mixtures [161, 162], protein thermodynamics [163], liquid crystals [164, 165], bilayer graphene [166], superconductors [167], modulated phases [168, 169] and even in black hole thermodynamics [170]. Despite its ubiquity, reentrance is typically unexpected and its explanation in terms of entropic contributions to the free-energy from the underlying microscopic degrees of freedom is usually subtle. In this context, while frequently observed in frustrated magnets, the microscopic mechanism leading to reentrance often remains obscure [113, 151, 152, 153, 154, 155, 156, 157]. Two mechanisms have commonly been invoked: a field-dependent suppression of quantum fluctuations [68, 171, 172] and the partial disorder of an intervening phase [160, 173, 174, 175]. Here, we present an alternative scenario of a generic nature which illustrates how the observation of reentrance may be used as a fingerprint of the frustration at play in the ground state.

In this Letter, we show that $\text{Er}_2\text{Sn}_2\text{O}_7$ represents a tractable material example where the intricate microscopic mechanisms responsible for reentrance in frustrated magnets can be rigorously studied experimentally and theoretically. $\text{Er}_2\text{Sn}_2\text{O}_7$ holds a special place among rare earth pyrochlores [2, 26]: it is well characterized, has a suppressed critical temperature and is one of the few materials with a simple Palmer-Chalker (PC) antiferromagnetic ground state [12, 16, 38] [Fig. 3.1(a)]. Its estimated exchange and single-ion susceptibility parameters are highly anisotropic and theory suggests a proximity to another competing antiferromagnetic

phase [1, 16, 38] known as Γ_5 [1, 2, 33] [Figs. 3.1(b) and 3.1(c)]. Because of this anisotropy, the response of $\text{Er}_2\text{Sn}_2\text{O}_7$ to an applied field is expected to differ with field direction, as has been poignantly illustrated with the experimental exploration of rare earth pyrochlore titanates [2, 26, 33, 153, 154]. As such, the present study critically relies on the recently gained, and notoriously challenging, ability to synthesize pyrochlore stannate single crystals [176], including $\text{Er}_2\text{Sn}_2\text{O}_7$.

We report herein the discovery of five occurrences of reentrance in the B - T phase diagram of $\text{Er}_2\text{Sn}_2\text{O}_7$ for fields along the [100], [110] and [111] cubic directions using heat capacity measurements. By thoroughly investigating this experimental phase diagram using mean field theory, classical linear spin-wave expansions and Monte Carlo simulations, we have uncovered the various, and distinct, microscopic origins of reentrance in this system. In short, we find that multiphase competitions at $T = 0$ result in enhanced thermal fluctuations at specific field values. These fluctuations *entropically* stabilize the corresponding *ordered* phase over the disordered phase, and thus increase $T_c(B)$ over a certain B field range. This produces $T_c(B)$ reentrant phase boundaries whose maximal temperature extent corresponds approximately to the zero-temperature field-driven phase transitions [see Figs. 3.2(a)-3.2(c)]. This multiphase competition is in some cases a direct consequence of the competition of the field-evolved PC states while in others it is inherent to $\text{Er}_2\text{Sn}_2\text{O}_7$'s zero-field ground state being in close proximity to the phase boundary between the PC and Γ_5 phases. See the Appendix for technical details on the experiments, simulations and analytics.

Heat capacity (C_p) measurements were performed on single crystal samples, grown via the hydrothermal method described in Ref. [176], down to 50 mK with varying magnetic fields, \mathbf{B} , oriented in the [111], [110], and [100] directions, using a dilution refrigerator insert in a Quantum Design Physical Properties Measurement System. Two measurement techniques were used: the conventional quasiadiabatic thermal relaxation method (called “short pulses” hereafter), as well as “long pulses”, both of which are described in detail in Ref. [77]. The long pulse technique allows faster and higher point-density measurements across phase transitions, enabling

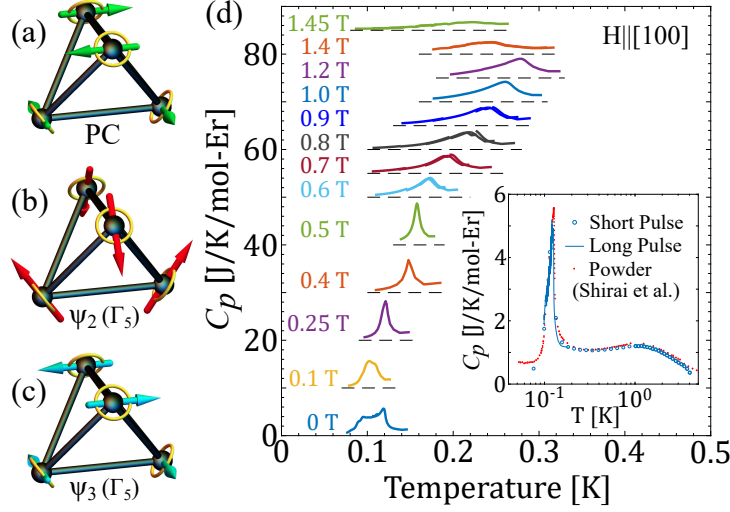


Figure 3.1: Example of sixfold degenerate states: (a) Palmer-Chalker [12] and (b) ψ_2 and (c) ψ_3 basis states of Γ_5 [13]. The ψ_2 and ψ_3 states are connected by a rotation of the spins by an angle ϕ within their local easy planes (yellow circles): $\phi \equiv n\pi/3 (+\pi/6)$ for $n = 0, \dots, 5$ correspond to ψ_2 (ψ_3) [14]. Panels (b) and (c) are for $\phi = 0$ and $\pi/2$, respectively. The manifold with $U(1)$ degeneracy, $\phi \in [0, 2\pi]$, forms the so-called Γ_5 states that appear in the [111] phase diagram. (d) Heat capacity, $C_p(T)$, vs temperature, T , of $\text{Er}_2\text{Sn}_2\text{O}_7$ with the magnetic field along [100], showing the reentrant nature of the transition. Curves at different fields are offset vertically for clarity. Similar data for the [110] and [111] field directions are included in the Appendix. (Inset) $C_p(T)$ $\text{Er}_2\text{Sn}_2\text{O}_7$ in zero field, with short and long pulse measurements on crystal samples overlaid. Powder data from Shirai *et al.* [15] is also overlaid to demonstrate agreement between sample types.

an accurate mapping of a phase diagram by measuring the field dependence of the transition temperature, $T_c(B)$ [Fig. 3.1 (d)].

In the zero-field heat capacity [Fig. 3.1 (d) inset], we find a sharp lambdalike anomaly indicative of a phase transition at $T_c = 118 \pm 5$ mK, which is consistent with previous measurements on powder samples reported in Ref. [15] [130 mK, from heat capacity, data shown in Fig. 3.1 (d) inset] and Ref. [16] [108 ± 5 mK, from DC magnetic susceptibility]. The extremely high point density of the long pulse measurements allows for the observation of subtle features in the peak shape, which are typically not resolved by conventional short pulse measurements. This reveals a low temperature shoulder of the C_p peak in the zero-field data at 97 ± 5 mK [177]. We performed elastic neutron scattering measurements to determine the magnetic structure between the sharp high temperature peak and the low temperature shoulder to check for an intermediate magnetic phase [177]. We found that the magnetic structure is of Palmer-Chalker type at all

measured temperatures throughout the transition range with no sign of other magnetic phases. It is not clear what causes this structure in the heat capacity anomaly, but we note that similar (though not identical) broadening is observed in all five crystals we have measured as well as in published data on a powder sample [15, 177] [Fig. 3.1 (d) inset]. Thus, it seems to be a feature of all $\text{Er}_2\text{Sn}_2\text{O}_7$ samples, but is likely due to (or influenced by) slight inhomogeneities rather than being purely intrinsic in origin. Although it may be worth future investigation, its presence does not affect any of the conclusions of this work.

To model $\text{Er}_2\text{Sn}_2\text{O}_7$, we use the generic nearest-neighbor Hamiltonian on the pyrochlore lattice [1, 37],

$$\mathcal{H} = \sum_{\langle i,j \rangle} J_{ij}^{\alpha\beta} S_i^\alpha S_j^\beta - \mu_B \sum_i g_i^{\alpha\beta} B^\alpha S_i^\beta. \quad (3.1)$$

$\mathbf{S}_i = (S_i^x, S_i^y, S_i^z)$ is a three-component pseudospin of length $|\mathbf{S}_i| = 1/2$ and \mathbf{B} is the external magnetic field. The g tensor represents the single-ion anisotropy, with local easy-plane g_\perp and easy-axis g_\parallel components at lattice site i . Given the symmetries of the pyrochlore lattice, the anisotropic exchange matrix $J_{ij}^{\alpha\beta}$ is parameterized by four independent coupling constants: (J_1, J_2, J_3, J_4) [36, 37]. $\text{Er}_2\text{Sn}_2\text{O}_7$ has been previously parameterized using inelastic neutron scattering on powder samples [16, 38]. Here we choose to remain within the error bars of Ref. [16], selecting a set of coupling parameters where simulations find $T_c \sim 180$ mK at 0.4 T for a [111] field to match the experimental result ⁵: $(J_1, J_2, J_3, J_4) = (+0.079, +0.066, -0.111, +0.032)$ meV and $g_\perp = 7.52, g_\parallel = 0.054$. Note that the nearest-neighbor part of dipolar interactions is included in the $J_{ij}^{\alpha\beta}$ couplings of the Hamiltonian (3.1).

To proceed, we first analyze this model using classical Monte Carlo simulations, with the results summarized in the B - T phase diagrams of Fig. 3.2. Most importantly, with $T_c(B=0.4\text{ T})$ fitted (for \mathbf{B} along the [111] direction), the simulations reproduce the number of reentrant ‘‘lobes’’

⁵Now that single crystals are available, fine-tuning these parameters by exploring the entire Q -space with neutron scattering would be a worthwhile endeavor for future work, albeit challenging due to the small mass of each crystal.

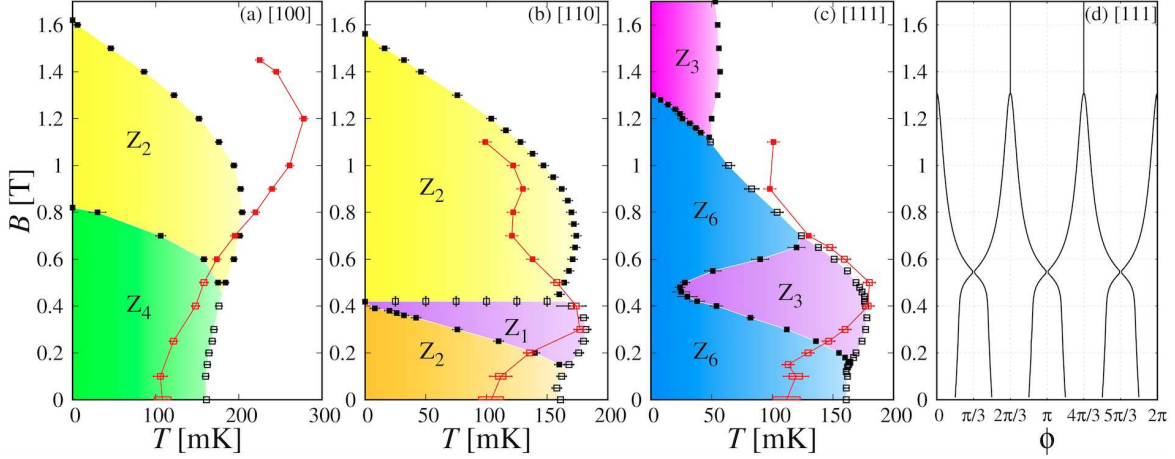


Figure 3.2: B - T phase diagrams of $\text{Er}_2\text{Sn}_2\text{O}_7$ in the (a) [100], (b) [110] and (c) [111] field directions, comparing experimental data with sharp (\square) and smooth (\blacksquare) heat-capacity peaks [Fig. 3.1(d)], to Monte Carlo results with first (\square) and second (\blacksquare) order transitions. Experiments and simulations are notably similar, showing the same (multiple) reentrance. The degeneracy Z_n found in simulations is given for each phase. The width of the red rectangles at 0 and 0.1 T represents the position of the double peaks. (d) In a [111] field, each of the six FEPC ground states has a Γ_5 contribution described by an angle ϕ [Figs. 3.1(b) and 3.1(c)], that can be computed exactly by minimizing the energy of one tetrahedron as a function of B .

for each field direction (e.g. one and two for a [100] and [110] field, respectively), as well as, at each lobe, the rough magnitude of the increase of T_c at the corresponding value of B . Moreover, simulations find that the transition always evolves from discontinuous to continuous when increasing the field. This is consistent with the shape of the experimental heat capacity peaks, evolving from sharp to smooth, and a further hint that simulations are capturing the proper physics displayed by the experiments. We suspect that a fine-tuning of the $J_{ij}^{\alpha\beta}$ coupling parameters and incorporating quantum fluctuations, as well as perhaps dipolar interactions beyond nearest neighbors, should account for the quantitative disagreements. Nevertheless, the semi-quantitative match between experiments and simulations confirms the validity of Eq. (3.1) as a minimal model for $\text{Er}_2\text{Sn}_2\text{O}_7$, suggesting that simulations robustly encapsulate the key physics behind the experimentally observed multiple occurrences of reentrance.

The results in Figs. 3.2(a)-3.2(c) raise multiple questions. Why are there multiple instances of reentrance and why are they so strongly dependent on the field direction? More fundamentally, why does $\text{Er}_2\text{Sn}_2\text{O}_7$ demonstrate reentrance in the first place? As a set of clues, simulations

bring to light a variety of phases that vie for ordering. In the rest of this Letter, we explain how soft modes induced by this multiphase competition are linked to reentrance, using a combination of mean field theory and classical linear spin-wave expansions.

The zero-field ground state of $\text{Er}_2\text{Sn}_2\text{O}_7$ is the sixfold-degenerate PC phase. However, the ground states naturally deform and evolve under the application of a magnetic field. For sufficiently large fields, some of these field-evolved PC (FEPC) states may become partially polarized into the *same* spin configuration. We therefore label the resulting phase according to the number of FEPC states that minimize the free energy but have *distinct* spin configurations (e.g. Z_6 at $B = T = 0$, for the six degenerate PC states, and Z_1 at sufficiently large B for the trivial field-polarized paramagnet). Phase transitions then occur whenever distinct FEPC states “merge” into the same spin configuration at a given field value B_c .

First, consider the [100] field phase diagram in Fig. 3.2(a). At $T = 0$, the FEPC states merge at $B_c = 0.82$ T, giving rise to the yellow Z_2 region. Figure 3.3 displays the classical spin-wave dispersions $\kappa_\nu(\mathbf{q})$ for a number of field values below and above B_c , calculated from the corresponding $T = 0$ FEPC ground states. As the merger transition is approached at $B_c = 0.82$ T, the bottom of the dispersive bands drop below the energy scale set by $T_c(B = 0) \approx 160$ mK, becoming soft and gapless at $B = B_c$. This decrease indicates a propensity for stronger thermal fluctuations at B_c than at other field values. More precisely, since $s = -\frac{1}{8N_q} \sum_{\mathbf{q}} \sum_{\nu=1}^8 \ln(\kappa_\nu(\mathbf{q}))$ quantifies the entropy contribution from classical spin waves, the decrease in $\kappa_\nu(\mathbf{q})$ on approaching B_c from above or below (as shown in Fig. 3.3) corresponds to an *increase* in entropy within the ordered phase. As a consequence, the gapless soft modes at B_c stabilize the yellow Z_2 region of Fig. 3.2 at finite temperature, both over the green Z_4 region as well as the disordered paramagnet.

At first sight, the above discussion may remind the reader of order-by-disorder, but the two mechanisms are in general different. Specifically, the Z_2 selection for $B \geq B_c$ is energetic and *not* entropic. As opposed to order-by-disorder, soft modes do not select the Z_2 states among a degenerate manifold, but rather enhance their entropic stability at a specific field, B_c , compared

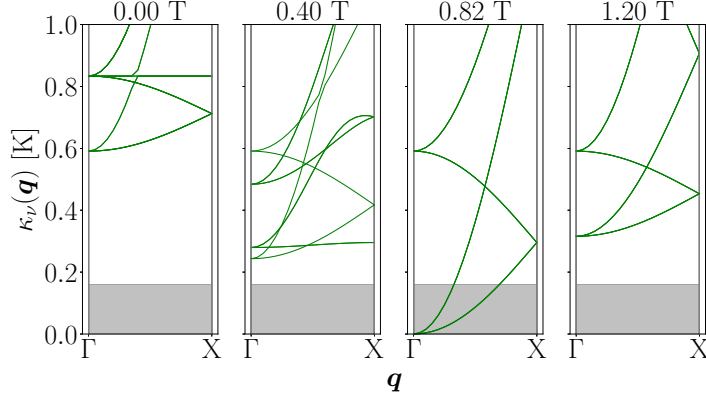


Figure 3.3: Classical spin-wave dispersions for $B = 0, 0.40, 0.82,$ and 1.20 T along the $[100]$ direction, for a path in the FCC Brillouin zone. Note that $B_c = 0.82$ T is a critical field at $T = 0$, as shown in Fig. 3.2. The grey boxes indicate energy scales below $T_c(B = 0 \text{ T}) \approx 160$ mK from Monte Carlo simulations; when modes occur within this region they are considered “soft”. Note that the dispersions for *all* Palmer-Chalker states are plotted, but may overlap at high-symmetry points or due to their degeneracies in a field.

to higher and lower fields. This pushes the transition temperature upwards around B_c , inducing reentrance.

The microscopic physics at play is different in a $[111]$ field; simulations reveal a reentrant lobe around a field value (~ 0.4 T) for which no corresponding $T = 0$ FEPC merger is found in the calculations. To understand this reentrance, it is important to note that the long-range order of $\text{Er}_2\text{Sn}_2\text{O}_7$ in a $[111]$ field is not described by a single irreducible representation (irrep) [1]. Instead, it is described by the naturally field-induced ferromagnetic irrep as well as the Γ_5 irrep [Fig. 3.1(b) and 3.1(c)] due to the proximity of the Γ_5 ground state to the PC phase in zero field [1]. The Γ_5 states bear an accidental $U(1)$ degeneracy parameterized by an angle ϕ [1, 14, 123, 178, 179], which is lifted by a magnetic field [180] with discrete values of ϕ being selected, as shown in Fig. 3.2(d). While the six FEPC states remain distinct in this region, their Γ_5 components merge at $B \approx 0.55$ T into three $\phi = \{\pi/3, \pi, 5\pi/3\}$ corresponding to three of the six ψ_2 states [Fig. 3.1(b), Ref. [177]]. This ψ_2 selection is associated with a flat low-energy soft mode in the spin-wave expansion at $B \approx 0.5$ T and simulations confirm the presence of partial ψ_2 order in the reentrant lobe, shown by the violet Z_3 phase in Fig. 3.2(c). These results make a strong case unraveling the mechanism of reentrance; the intervening Z_3 phase, which is *not*

part of the ground states, is entropically stabilized by low-energy soft modes arising from the PC and $\Gamma_5(\psi_2)$ phase competition.

Closing the [111] case, one should mention the FEPC merger transition at $B_c = 1.31$ T and $T = 0$ is naturally accompanied by a merging of the ϕ values [here also corresponding to ψ_2 states, see Fig. 3.2(d)] and by a small reentrant lobe [Fig. 3.2(c)], as expected from the discussion for the [100] field case. Our experimental data point towards the onset of this high-field lobe as well (see Fig. 3.2(c) for $B = 0.9$ T and 1.1 T). However, it was not possible to explore this high-field region experimentally because the sample did not easily equilibrate above 0.7 T. Interestingly, simulations also suffer from difficulties thermalizing between 0.7 and 1.2 T.

Finally, the mechanisms behind reentrance for a [110] field are reminiscent of the other two field directions [Fig. 3.2(b)]. Below $B \lesssim 0.1$ T, simulations are difficult to thermalize (see Appendix), but above $B \gtrsim 0.1$ T, we find two FEPC ground states that merge at $B_c = 0.42$ T. This merging gives rise to gapless soft modes, the subsequent violet Z_1 phase, and reentrance at finite temperatures. It is the same mechanism as in a [100] field. However, as opposed to the [100] scenario, this newly merged ground state vanishes immediately once $B > B_c$ (i.e. it becomes an excited state). The system is then found in two *other* ground states (corresponding to the yellow Z_2 phase). The vanishing of the merged state corresponds to the Z_1 phase abruptly disappearing above B_c and the removal of the aforementioned gapless soft modes. This causes the rapid collapse of the reentrant lobe at $B \sim 0.42$ T. The fact that Z_1 order is only stable at one point at $T = 0$ is reminiscent of the triangular Heisenberg antiferromagnet in a field, where an intervening $1/3$ plateau also spreads at finite temperature and gives rise to reentrance [151, 155, 181] – a mechanism that might be at play in $\text{Ba}_3\text{CoSb}_2\text{O}_9$ [182]. However, the reentrance phenomenon in our system at 0.42 T differs from this case in that it does not require the extensive degeneracy of a magnetization plateau, but simply the more generic presence of soft modes about a long-range ordered nondegenerate spin configuration.

At higher [110] field, another reentrant dome appears ($B \sim 0.7$ T), however, there are no ground state FEPC mergers involved. Similarly to the reentrant behavior at low [111] field,

spin-wave theory shows a *minimum (non-zero) gap* that entropically favors the ordered phase around 0.7 T (see Section S5 in the Appendix). These low-energy gapped modes, along with the collapse at $B_c = 0.42$ T, give the higher field reentrant lobe at ~ 0.7 T.

In summary, we have presented the first exploration of the field-direction dependence of the thermodynamics of stannate pyrochlores, which, despite decades of effort, were not available as single crystals until very recently [176]. Access to these crystals has proven to be crucial since the phase diagram of $\text{Er}_2\text{Sn}_2\text{O}_7$ is highly sensitive to the field direction, and exhibits several reentrant lobes with sundry underlying mechanisms. These features result from the competition of several orders, especially the zero-field Palmer-Chalker, the field-induced ferromagnetic and the neighboring Γ_5 states. In particular, most instances of reentrance in the phase diagram can be traced to zero-temperature field-induced merging of ground states. This energetic selection is accompanied by soft modes which entropically enhance the transition temperatures, and this mechanism is thus distinct from the one of order-by-disorder. In this light, reentrance is a useful and experimentally accessible fingerprint at the critical temperature of an underlying zero-temperature phase transition.

Given that multiphase competition is a common feature of frustrated magnetism, we expect the mechanisms we have uncovered to be widespread among magnetic systems displaying reentrance; especially since it does not require the accidental presence of an exotic partially disordered phase [160, 174, 183, 184, 185] or a phase with extensive entropy, such as in a magnetization plateau state [151, 155, 181, 182]. In semiclassical and quantum systems, our mechanism may work together with the field-induced suppression of quantum fluctuations [171] to produce even larger reentrant lobes. We hope our work will motivate others to pursue a microscopic interpretation of future observations of reentrance (and possibly to revisit old ones [113, 151, 152, 153, 154, 155, 156, 157, 158]) in light of zero-temperature transitions. Since magnetic systems often afford us with minimal models to understand other areas of physics, our results raise a more general question: If reentrance is observed by varying a

given parameter, when is it actually due to a nearby transition in a broader, and perhaps not even physically accessible, parameter space?

3.4 Supplemental material

Definition of Palmer-Chalker states

There are six Palmer-Chalker states in zero field [Fig. 3.4]; the spin configurations for three of these (on the four sublattices of a tetrahedron) are outlined in Table 3.1. The remaining three, denoted as $\langle \bar{x}y \rangle$, $\langle \bar{x}z \rangle$, and $\langle \bar{y}z \rangle$, can be obtained from the listed three by reversal of the spins.

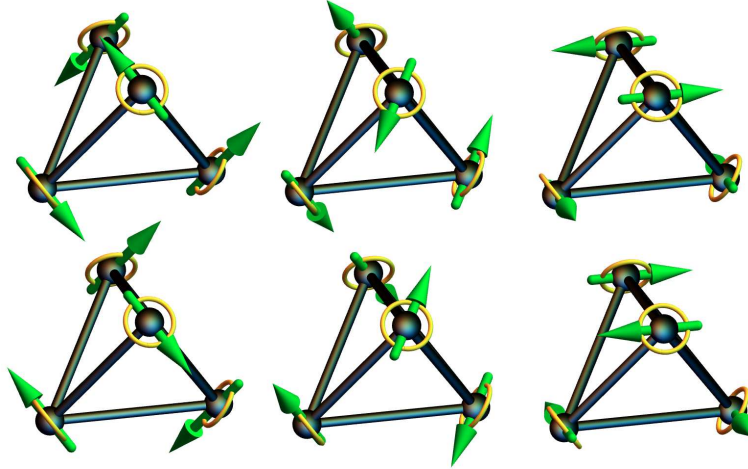


Figure 3.4: The six Palmer-Chalker states, labeled from left to right $\langle xz \rangle$, $\langle yz \rangle$, $\langle xy \rangle$ (first row) and $\langle \bar{x}z \rangle$, $\langle \bar{y}z \rangle$, $\langle \bar{x}y \rangle$ (second row).

Table 3.1: Spin configurations for three of the six Palmer-Chalker states on the four sublattices $i = 0, 1, 2, 3$ of a tetrahedron. Each state lies within a plane in the global frame of reference (e.g. $\langle xy \rangle$ lies in the xy -plane). The remaining three Palmer-Chalker states are obtained by spin reversal. The convention for labeling the sublattices follows the one from Ref. [1].

$\langle xy \rangle$	$\langle xz \rangle$	$\langle yz \rangle$
$\mathbf{m}_0 = \frac{1}{\sqrt{2}}(1, -1, 0)$	$\mathbf{m}_0 = \frac{1}{\sqrt{2}}(1, 0, -1)$	$\mathbf{m}_0 = \frac{1}{\sqrt{2}}(0, 1, -1)$
$\mathbf{m}_1 = \frac{1}{\sqrt{2}}(-1, -1, 0)$	$\mathbf{m}_1 = \frac{1}{\sqrt{2}}(-1, 0, -1)$	$\mathbf{m}_1 = \frac{1}{\sqrt{2}}(0, -1, 1)$
$\mathbf{m}_2 = \frac{1}{\sqrt{2}}(1, 1, 0)$	$\mathbf{m}_2 = \frac{1}{\sqrt{2}}(-1, 0, 1)$	$\mathbf{m}_2 = \frac{1}{\sqrt{2}}(0, -1, -1)$
$\mathbf{m}_3 = \frac{1}{\sqrt{2}}(-1, 1, 0)$	$\mathbf{m}_3 = \frac{1}{\sqrt{2}}(1, 0, 1)$	$\mathbf{m}_3 = \frac{1}{\sqrt{2}}(0, 1, 1)$

Additional heat capacity data

Figure 3.5 shows the raw zero-field long pulse heat capacity data for three different single crystals polished in the three high symmetry directions. As discussed in the main text, we find a sharp peak at 118 ± 5 mK with a low-temperature shoulder around 97 ± 5 mK. A similar broad feature can be seen in polycrystalline measurements by Ref. [15], but the broadness of the peak is not discussed therein. The heat capacity measurements in field are shown in Figure 3.6 for fields applied along the three cubic directions, the transition temperatures of which are included in Figure 3.2 in the main text.

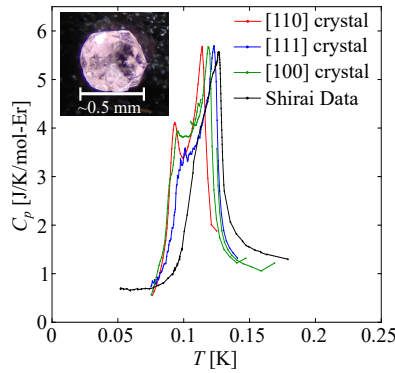


Figure 3.5: Raw zero field heat capacity data for the three crystals polished in each of the high symmetry directions. We find that all samples show a low temperature shoulder, but the pronouncement of the shoulder varies between samples. (Inset) Example of a typical crystal that was used in heat capacity measurements.

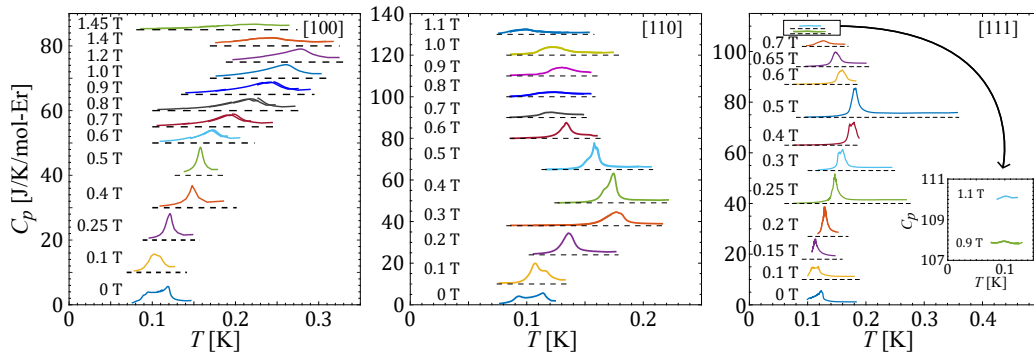


Figure 3.6: Raw long pulse heat capacity data for fields along the three cubic high symmetry directions, leading to the phase diagram shown in the main text. Note, all data at nonzero field have been shifted vertically for clarity.

Neutron scattering experimental details and results

Elastic neutron scattering measurements were performed at the NIST Center for Neutron Research using the SPINS triple axis spectrometer. Approximately 4 g of crystals were ground into a fine powder and placed in a copper cigar-type foil construction that was inside the sample can, which was subsequently filled with 10 atm of He gas at room temperature. We collected elastic scattering scans at 50 mK, 110 mK, and 8 K on the (111), (002), (220), (113) and (222) Bragg peaks using $E = 5$ meV neutrons with an energy resolution of approximately 0.25 meV. The collimation settings were guide-open-80'-open, with Be filters placed before and after the sample.

The 50 mK data was taken to corroborate the Palmer-Chalker ground state found from powder samples by Ref. [16], as it should be well into the ordered phase. Data at 110 mK was taken as it lies in between the high temperature and low temperature peaks we find in the heat capacity curve (118 and 97 mK respectively), as discussed in the main text, and could possibly show evidence for an intermediate phase. We find that the correlations are Palmer-Chalker throughout the broad transition, as evidenced by the $Q = (111), (002)$ and (220) Bragg peaks. In particular, there was no hint of Γ_5 order, which may have been a likely intermediate phase candidate due

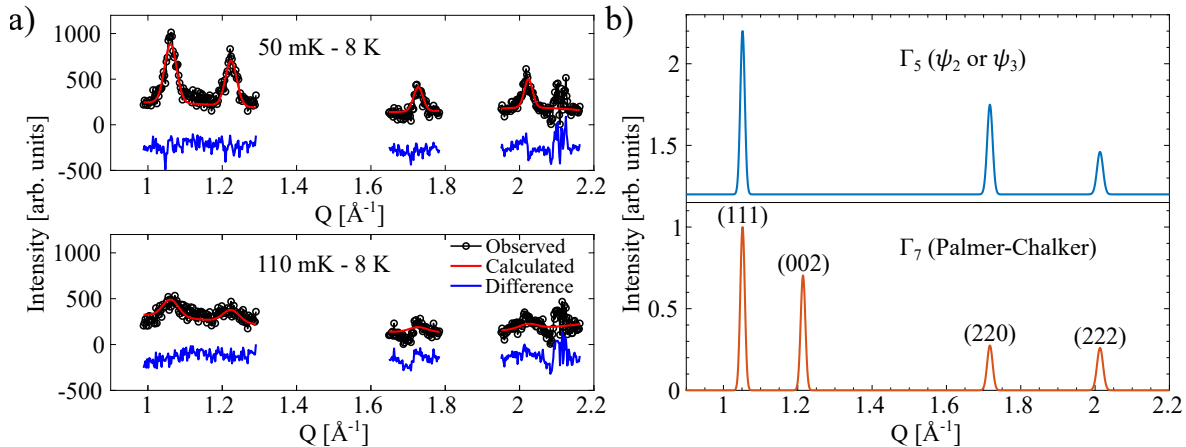


Figure 3.7: (a) Elastic neutron scattering data (black) on SPINS. Data was taken at 50 mK, 110 mK, and 8 K, with 8 K data used for background subtraction. The fit to the PC phase is shown (red), as well as the difference between the data and fit (blue). (b) Calculated magnetic diffraction patterns for the Γ_5 and PC (Γ_7) configurations (nuclear contributions not shown). The Γ_5 pattern has been shifted vertically for clarity.

to the material's proposed proximity to the phase boundary between PC and Γ_5 [16, 38]. No (002) intensity is expected for the Γ_5 phase [Fig 3.7 (b)], and we do not see any evidence of an enhanced (111) nor (220) peak that could indicate coexistence of the Γ_5 and PC (Γ_7) phase. The fit to the Palmer-Chalker structure is shown in Fig 3.7 (a) and is in agreement with the Ref. [16] powder diffraction data. We note that only intermediate phases with ordering wave vector $\mathbf{q} = 0$ were investigated, and it is still possible that a $\mathbf{q} \neq 0$ intermediate phase could exist.

Variational mean field theory and the Palmer-Chalker merger transitions

The following derivation of variational mean field theory for a spin system on the pyrochlore lattice, with an exchange Hamiltonian and an applied magnetic field, follows Refs. [186, 187, 188]. The exchange Hamiltonian can be written as

$$\mathcal{H}_0 = \frac{1}{2} \sum_{a,b} \sum_{i,j} \sum_{\mu,\nu} J_{ia,jb}^{\mu\nu} S_{ia}^\mu S_{jb}^\nu, \quad (3.2)$$

where a and b denote the chosen tetrahedra, i and j denote the sublattices chosen within those tetrahedra, and μ and ν denote the components of the (classical) spin vectors. The exchange matrix $J_{ia,jb}^{\mu\nu}$ is completely general in this form. In this work, we have predominantly only taken into account the global-frame nearest-neighbor exchange parameters that are defined for rare-earth pyrochlore systems with a Kramers ground state doublet [1]. However, this general form can also include the dipole-dipole interaction (as will be discussed at the end of this section). With an applied magnetic field, this Hamiltonian becomes

$$\mathcal{H} = \frac{1}{2} \sum_{a,b} \sum_{i,j} \sum_{\mu,\nu} J_{ia,jb}^{\mu\nu} S_{ia}^\mu S_{jb}^\nu - \sum_{i,a} \mathbf{h}_{ia} \cdot \mathbf{S}_{ia}. \quad (3.3)$$

The scaled magnetic field for a given applied magnetic field B^ν is given by

$$h_{ia}^\mu = \mu_B g_{ia}^{\mu\nu} B^\nu, \quad (3.4)$$

where $g_{ia}^{\mu\nu}$ is the g -tensor of the ion at the given sublattice i , expressed in the global frame of Ref. [1] and μ_B is the Bohr magneton. This g -tensor is independent of the tetrahedron a and only depends on which sublattice i is considered [1]. Henceforth, all physical quantities with energy dimension are measured in K (Kelvin) units and, as such, we correspondingly set the Boltzmann constant $k_B = 1$.

The mean field free energy is given by

$$F_\rho = \text{Tr}\{\rho \mathcal{H}\} + T \text{Tr}\{\rho \ln \rho\}, \quad (3.5)$$

where ρ is the many-body density matrix and the trace is computed over all spin configurations. The variational mean field approximation assumes $\rho(\{\mathbf{S}_{ia}\}) = \prod_{i,a} \rho_{ia}(\mathbf{S}_{ia})$, where ρ_{ia} is the density matrix for a single site's spin. These single-site density matrices are then treated as variational parameters, subject to the constraints of normalization ($\text{Tr}\{\rho_{ia}\} = 1$) and the order parameter definition ($\text{Tr}\{\rho_{ia} \mathbf{S}_{ia}\} = \mathbf{m}_{ia}$). Enforcing these constraints using the sets of Lagrange multipliers $\{\xi_{ia}\}$ and $\{\mathbf{A}_{ia}\}$ yields

$$\begin{aligned} F(\{\rho_{ia}\}, \{\xi_{ia}\}, \{\mathbf{A}_{ia}\}) = & \text{Tr}\{\rho \mathcal{H}\} + T \text{Tr}\{\rho \ln \rho\} - T \text{Tr} \left\{ \sum_{i,a} \xi_{ia} (\rho_{ia} - 1) \right\} \\ & - T \text{Tr} \left\{ \sum_{i,a} (\rho_{ia} \mathbf{S}_{ia} - \mathbf{m}_{ia}) \cdot \mathbf{A}_{ia} \right\}. \end{aligned} \quad (3.6)$$

Minimizing the free energy with respect to the variational parameters, the single-site density matrices are found to be $\rho_{ia} = \frac{1}{Z_{ia}} e^{A_{ia} \cdot \mathbf{S}_{ia}}$. The partition function Z_{ia} is computed by integrating over all spin configurations in spherical coordinates, given that the spins are treated classically (that is, as continuous vectors); this yields $Z_{ia} = \frac{4\pi}{A_{ia}} \sinh(A_{ia})$, where $A_{ia} = |\mathbf{A}_{ia}|$. Using the above relations and computing the traces in Eqn. (3.6), the free energy simplifies to

$$F = \frac{1}{2} \sum_{a,b} \sum_{i,j} \sum_{\mu,\nu} J_{ia,jb}^{\mu\nu} m_{ia}^\mu m_{jb}^\nu - \sum_{i,a} \mathbf{h}_{ia} \cdot \mathbf{m}_{ia} + \sum_{i,a} (\mathbf{H}_{ia} \cdot \mathbf{m}_{ia} - \frac{1}{\beta} \ln(Z_{ia})), \quad (3.7)$$

where $\mathbf{H}_{ia} \equiv \frac{A_{ia}}{\beta}$ can be considered as a local field. Explicitly, by minimizing the free energy with respect to the order parameters \mathbf{m}_{ia} , $\frac{\partial F}{\partial m_{ia}^\mu} = 0$, it can be shown that

$$H_{ia}^\mu = - \sum_{j,b,\nu} J_{ia,jb}^{\mu\nu} m_{jb}^\nu + h_{ia}^\mu. \quad (3.8)$$

Using this expression for H_{ia}^μ , the free energy, f , averaged over all N sites of the lattice is

$$f = \frac{F}{N} = \frac{X(m)}{N} - \frac{1}{N\beta} \sum_{i,a} \ln(Z_{ia}), \quad (3.9)$$

where

$$X(m) \equiv -\frac{1}{2} \sum_{a,b} \sum_{i,j} \sum_{\mu,\nu} J_{ia,jb}^{\mu\nu} m_{ia}^\mu m_{jb}^\nu. \quad (3.10)$$

Lastly, using the identity $\frac{\partial f}{\partial H_{ia}^\mu} = -m_{ia}^\mu$ for the order parameter at each site, one finds

$$\mathbf{m}_{ia} = \frac{\mathbf{H}_{ia}}{|\mathbf{H}_{ia}|} \left[\coth(\beta|\mathbf{H}_{ia}|) - \frac{1}{\beta|\mathbf{H}_{ia}|} \right]. \quad (3.11)$$

This equation relates the local field \mathbf{H}_{ia} with the order parameter \mathbf{m}_{ia} at each site, which can be calculated self-consistently.

The evolution of a chosen Palmer-Chalker state (e.g. $\langle xy \rangle$) in the presence of an applied magnetic field, \mathbf{B} , is accomplished within variational mean field theory as follows: For a given magnitude and direction of the field (at zero temperature), the tetrahedra of the pyrochlore lattice are initiated with an initial spin configuration. At zero field, this initial spin configuration is that of the chosen Palmer-Chalker state. At finite field, this initial spin configuration is the mean field solution from the previous field magnitude. For example, if the mean field calculation is done for B values incremented by 0.01 T, the initial configuration used for $B = 0.11$ T is the mean field solution from $B = 0.10$ T. In this way, the evolution of the chosen zero-field Palmer-Chalker state can be tracked as a function of B . The self-consistency equation Eq. (3.11) is then solved iteratively for zero temperature until convergence is attained. The resulting spin configuration

is denoted with a subscript h (e.g. $\langle xy \rangle_h$) to represent that it is the field-evolved configuration of the originally-chosen Palmer-Chalker state. This field-evolved Palmer-Chalker (FEPC) state for a given B can then be used to tile the pyrochlore lattice and solve the self-consistency equation for *finite* temperatures for the same B value, showing how the chosen Palmer-Chalker state evolves with temperature as well. This process is followed for *each* of the six parent $B = 0$ Palmer-Chalker states, in order to track their field and temperature evolution individually.

The mean field calculations are performed for a pyrochlore lattice of size $L = 2$ (in terms of cubic unit cells) for a total of $16L^3 = 128$ sites. At all fields and temperatures, the spin configuration is always found to be $\mathbf{q} = 0$ ordering wave vectors. The phases can be labelled by (i) how many of the six FEPC states minimize the free energy (which may be less than six), and (ii) how many of these degenerate FEPC states have distinct spin configurations. If there are n distinct spin configurations out of all degenerate FEPC states, that phase is labelled as a \mathbb{Z}_n phase, reflecting the order of the discrete degeneracy. Phase transitions are then indicated by a reduction in this discrete symmetry as the field increases, referred to as “merger” transitions. The mean field phase diagram for the [100], [111], and [110] field directions, as well as a pictorial representation of the merger transitions at zero temperature, are illustrated in Fig. 3.8.

Variational mean field theory including dipolar interactions has also been performed by use of the Ewald summation method [179, 187, 189]. When including the dipolar interactions, the g -tensor must be properly incorporated to map the interaction (between dipoles) onto the pseudospin $S = \frac{1}{2}$ representation. It should also be noted that the nearest-neighbor part of the dipolar interaction is already included in the nearest-neighbor exchange couplings (J_1, J_2, J_3, J_4). With the inclusion of dipolar interactions, the critical temperatures and fields are reduced relative to Fig. 3.8, but the $\mathbf{q} = 0$ orders, \mathbb{Z}_n phases, and overall topology of the phase diagrams remain unchanged.

Classical spin-wave expansion

A classical spin-wave expansion for $\mathbf{q} = 0$ spin ordering on the pyrochlore lattice and without an applied field is detailed in Ref. [1] and is similar to the derivation below for a classical

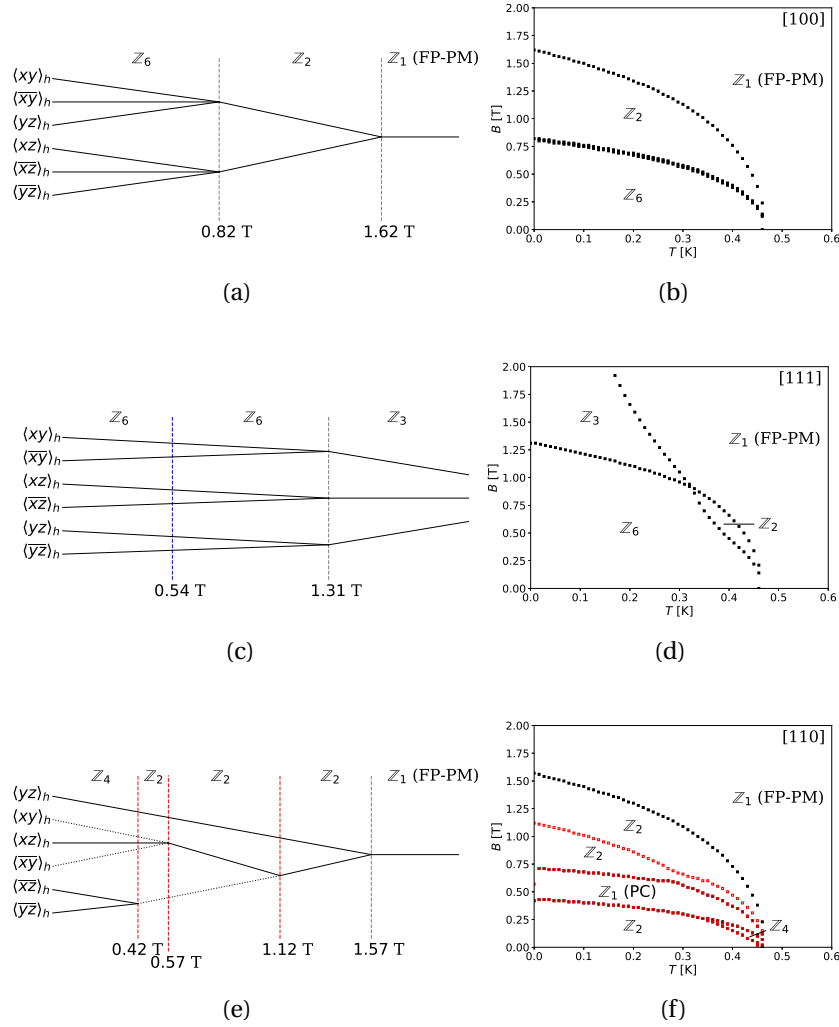


Figure 3.8: Zero temperature representations of field-evolved Palmer-Chalker (FEPC) mergers ((a), (c), and (e)) and mean field B - T phase diagrams ((b), (d), and (f)) for the [100], [111], and [110] field directions, respectively. In the FEPC merger diagrams, vertical grey lines represent critical fields of the merging transitions; the vertical blue line represents field-induced selection of the ψ_2 phase out of the accidentally-degenerate Γ_5 manifold; vertical red lines represent changes in the set of degenerate FEPC states. Solid lines denote the FEPC states that are degenerate and minimize the energy; dotted lines represent FEPC states that are excited and do not minimize the energy. In the mean field phase diagrams, filled black squares represent a phase transition to a phase of different discrete symmetry due to merging; open red squares represent a change in the set of degenerate FEPC states. In both sets of diagrams, Z_n denotes the discrete symmetry of the phase, which has n distinct spin configurations out of the degenerate FEPC states. FP-PM denotes the field-polarized paramagnetic phase; PC denotes Palmer-Chalker order. Note that the zero temperature phases in the [110] field direction differ from the finite temperature phases due to entropic effects, for reasons discussed further in Section 3.4. Note also that Z_n labels for the mean-field phase diagrams may differ from those of the Monte Carlo phase diagrams shown in Fig. 2 of the main text due to thermal order-by-disorder selection (e.g. the low-field Z_6 region of the mean-field [100] phase diagram, versus the low-field Z_4 region of the Monte Carlo [100] phase diagram).

spin-wave expansion in a finite field. Informed by the mean field results at zero temperature, $\mathbf{q} = 0$ ordering is assumed and dipolar interactions, which do not change the topology of the phase diagram, are excluded. Under these assumptions, the Hamiltonian is

$$\mathcal{H} = \frac{1}{2} \sum_a \sum_{ij} J_{ij}^{\mu\nu} S_{ia}^\mu S_{ja}^\nu - \mu_B \sum_a \sum_i g_i^{\mu\nu} S_{ia}^\mu B^\nu, \quad (3.12)$$

where $J_{ij}^{\mu\nu}$ is now restricted to only nearest neighbors, and the tetrahedra indices are suppressed because of the $\mathbf{q} = 0$ assumption.

Starting with the classically-ordered ground state spin configuration on a single tetrahedron at $T = 0$, we define the local coordinate system at each sublattice with $\{\mathbf{u}_i, \mathbf{v}_i, \mathbf{w}_i\}$, where the classical spin vector is of length S and points along \mathbf{w}_i . The other two local unit vectors are defined arbitrarily, so long as mutual orthogonality is satisfied. The fluctuations about this ordered spin vector, on sublattice i and tetrahedron a , can then be expressed as

$$\mathbf{S}_{ia} = \begin{bmatrix} \sqrt{S} \delta u_{ia} \\ \sqrt{S} \delta v_{ia} \\ \sqrt{S^2 - S \delta u_{ia}^2 - S \delta v_{ia}^2} \end{bmatrix} \approx \begin{bmatrix} \sqrt{S} \delta u_{ia} \\ \sqrt{S} \delta v_{ia} \\ S - \frac{1}{2} \delta u_{ia}^2 - \frac{1}{2} \delta v_{ia}^2 \end{bmatrix}. \quad (3.13)$$

Substituting this perturbed spin into the original Hamiltonian and expanding to quadratic order in the fluctuations yields

$$\begin{aligned} \mathcal{H} = & \frac{1}{2} N_t \sum_{ij} S^2 (\mathbf{w}_i \cdot \vec{\mathbf{J}}_{ij} \cdot \mathbf{w}_j) - \mu_B S N_t \sum_i (\mathbf{w}_i \cdot \vec{\mathbf{g}}_i \cdot \mathbf{B}) + \frac{S}{2} \sum_a \sum_{ij} \delta u_{ia} \delta u_{ja} (\mathbf{u}_i \cdot \vec{\mathbf{J}}_{ij} \cdot \mathbf{u}_j) \\ & + \delta u_{ia} \delta v_{ja} (\mathbf{u}_i \cdot \vec{\mathbf{J}}_{ij} \cdot \mathbf{v}_j) + \delta v_{ia} \delta u_{ja} (\mathbf{v}_i \cdot \vec{\mathbf{J}}_{ij} \cdot \mathbf{u}_j) + \delta v_{ia} \delta v_{ja} (\mathbf{v}_i \cdot \vec{\mathbf{J}}_{ij} \cdot \mathbf{v}_j) \\ & - \frac{1}{2} (\delta u_{ia}^2 + \delta v_{ia}^2 + \delta u_{ja}^2 + \delta v_{ja}^2) (\mathbf{w}_i \cdot \vec{\mathbf{J}}_{ij} \cdot \mathbf{w}_j) + \frac{1}{2} \mu_B \sum_a \sum_{ij} (\delta u_{ia}^2 + \delta v_{ia}^2) (\mathbf{w}_i \cdot \vec{\mathbf{g}}_i \cdot \mathbf{B}). \end{aligned} \quad (3.14)$$

The first two terms represent the ground state energy, ε_0 , where N_t is the number of tetrahedra in the system ($N_t = \frac{N}{4}$, where N is the number of spins in the system). The rest of the expression encapsulates the effect of fluctuations from exchange and Zeeman interactions.

Performing a Fourier transform over the reciprocal lattice vectors \mathbf{q} of the FCC lattice and defining $\mathbf{u}(\mathbf{q}) \equiv (\delta u_1(\mathbf{q}), \delta u_2(\mathbf{q}), \delta u_3(\mathbf{q}), \delta u_4(\mathbf{q}), \delta v_1(\mathbf{q}), \delta v_2(\mathbf{q}), \delta v_3(\mathbf{q}), \delta v_4(\mathbf{q}))$, the fluctuation contribution to the Hamiltonian can be written as:

$$\mathcal{H} = \varepsilon_0 + \frac{1}{2} \sum_{\mathbf{q}} \mathbf{u}(-\mathbf{q}) \left(\vec{\mathbf{M}}(\mathbf{q}) + \vec{\mathbf{N}}(\mathbf{q}) \right) \mathbf{u}(\mathbf{q}). \quad (3.15)$$

The matrices $\vec{\mathbf{M}}(\mathbf{q})$ and $\vec{\mathbf{N}}(\mathbf{q})$ can be written in block matrix form, composed of four separate 4×4 blocks. They are:

$$\vec{\mathbf{M}} = 2S \begin{bmatrix} \vec{\mathbf{M}}^{11}(\mathbf{q}) & \vec{\mathbf{M}}^{12}(\mathbf{q}) \\ \vec{\mathbf{M}}^{21}(\mathbf{q}) & \vec{\mathbf{M}}^{22}(\mathbf{q}) \end{bmatrix} \quad (3.16)$$

$$M_{ij}^{11} = \cos(\mathbf{q} \cdot \mathbf{r}_{ij}) (\mathbf{u}_i \cdot \vec{\mathbf{J}}_{ij} \cdot \mathbf{u}_j - \delta_{ij} \sum_l \mathbf{w}_l \cdot \vec{\mathbf{J}}_{lj} \cdot \mathbf{w}_j)$$

$$M_{ij}^{12} = \cos(\mathbf{q} \cdot \mathbf{r}_{ij}) (\mathbf{u}_i \cdot \vec{\mathbf{J}}_{ij} \cdot \mathbf{v}_j)$$

$$M_{ij}^{21} = \cos(\mathbf{q} \cdot \mathbf{r}_{ij}) (\mathbf{v}_i \cdot \vec{\mathbf{J}}_{ij} \cdot \mathbf{u}_j)$$

$$M_{ij}^{22} = \cos(\mathbf{q} \cdot \mathbf{r}_{ij}) (\mathbf{v}_i \cdot \vec{\mathbf{J}}_{ij} \cdot \mathbf{v}_j - \delta_{ij} \sum_l \mathbf{w}_l \cdot \vec{\mathbf{J}}_{lj} \cdot \mathbf{w}_j)$$

$$\vec{\mathbf{N}} = \mu_B \begin{bmatrix} \vec{\mathbf{N}}^{11}(\mathbf{q}) & 0 \\ 0 & \vec{\mathbf{N}}^{22}(\mathbf{q}) \end{bmatrix} \quad (3.17)$$

$$N_{ij}^{11} = N_{ij}^{22} = \delta_{ij} \mathbf{w}_i \cdot \vec{\mathbf{g}}_i \cdot \mathbf{B}.$$

Diagonalizing this harmonic spin-wave Hamiltonian yields the classical spin-wave dispersions $\kappa_\nu(\mathbf{q})$ as a function of the wavevector \mathbf{q} . Since the classical spin-wave Hamiltonian is quadratic, the partition function and free energy of the classical spin waves can be calculated exactly. Assuming the above diagonalization has been performed to find the normal modes, $\phi_\nu(\mathbf{q})$, and

dispersions, $\kappa_\nu(\mathbf{q})$, the partition function and free energy are given by

$$Z = \int \left[\prod_{\mathbf{q}} \prod_{\nu=1}^8 d\phi_\nu(\mathbf{q}) \right] e^{-\frac{1}{T}(\varepsilon_0 + \frac{1}{2} \sum_{\mathbf{q}} \sum_{\nu=1}^8 \kappa_\nu(\mathbf{q}) \phi_\nu(\mathbf{q}) \phi_\nu(-\mathbf{q}))} \quad (3.18)$$

$$= e^{-\frac{\varepsilon_0}{T}} \prod_{\mathbf{q}} \prod_{\nu=1}^8 \sqrt{\frac{2\pi T}{\kappa_\nu(\mathbf{q})}} \quad (3.19)$$

$$\Rightarrow F = \varepsilon_0 + \frac{T}{2} \sum_{\mathbf{q}} \sum_{\nu=1}^8 \ln(\kappa_\nu(\mathbf{q})) - NT \ln(2\pi T). \quad (3.20)$$

If there are $N_q = \frac{N}{4}$ wavevectors in the sum, then the free energy per spin is

$$f = \frac{\varepsilon_0}{N} + \frac{T}{8N_q} \sum_{\mathbf{q}} \sum_{\nu=1}^8 \ln(\kappa_\nu(\mathbf{q})) - T \ln(2\pi T). \quad (3.21)$$

Note that the entropy per spin, s , can be calculated using $s = -\frac{\partial f}{\partial T}$. Computing this, but keeping only the terms that depend on the spin-wave dispersions $\kappa_\nu(\mathbf{q})$, yields

$$s = -\frac{1}{8N_q} \sum_{\mathbf{q}} \sum_{\nu=1}^8 \ln(\kappa_\nu(\mathbf{q})). \quad (3.22)$$

The dispersions $\kappa_\nu(\mathbf{q})$ for each of the FEPC states are shown in Fig. 3.9 at various relevant choices of the applied field (e.g. at the merger transitions).

Monte Carlo simulations and parameters

Monte Carlo simulations are performed on systems of classical Heisenberg spins with $N = 16L^3$ sites, where L^3 is the number of cubic unit cells. The spin length is $|S| = 1/2$. Several update algorithms are used together: the heatbath method, over-relaxation and parallel tempering. Parallel tempering is done every 100 Monte Carlo steps (MCS) and overrelaxation is done at every MCS. Thermalization is made in two steps: first a slow annealing from high temperature to the temperature of measurement T during t_e MCS followed by t_e MCS at temperature T . After thermalization, measurements are done every 10 MCS during $t_m = 10 t_e$ MCS.

The characteristics of our simulations are typically:

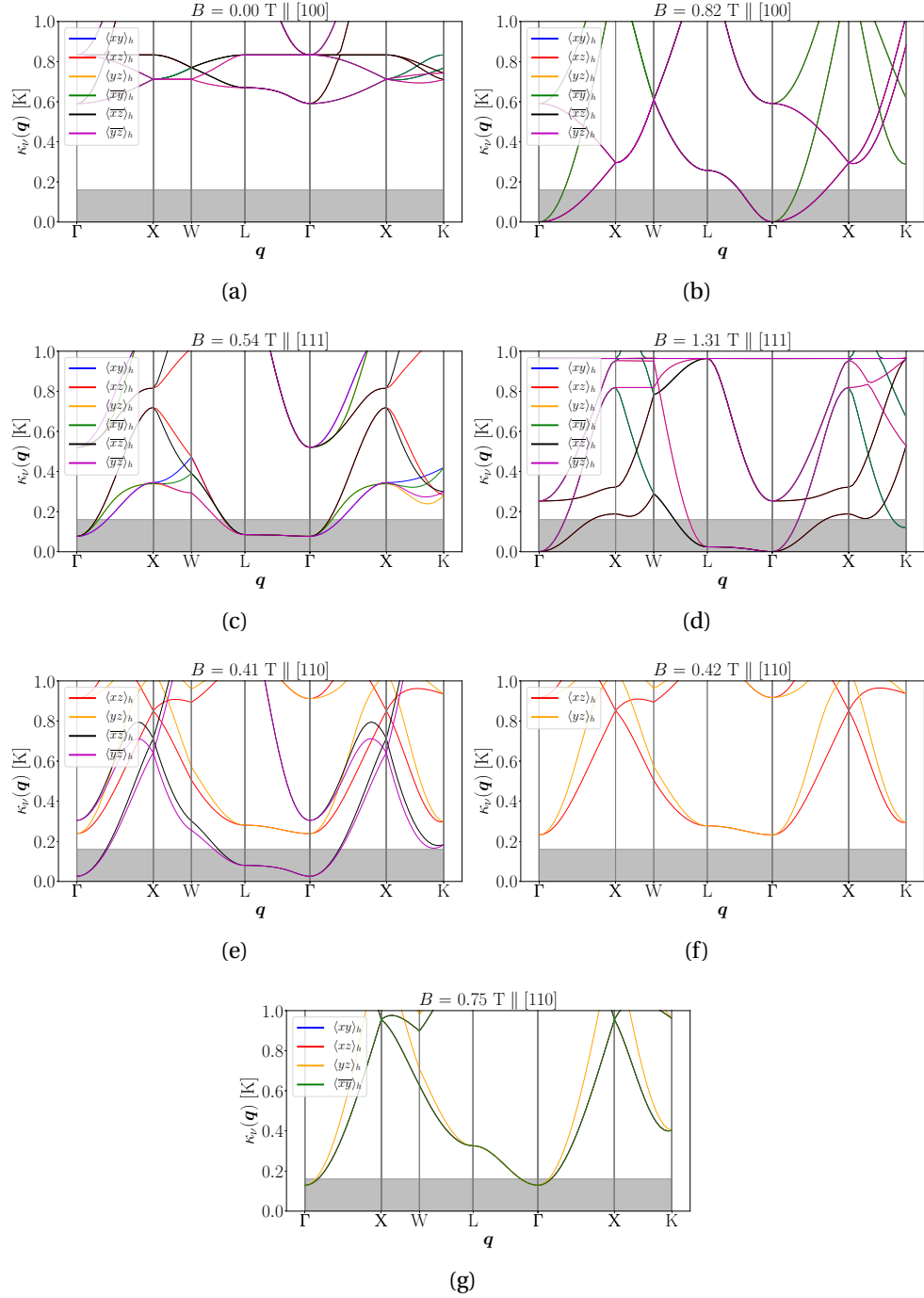


Figure 3.9: Classical spin-wave dispersions for all Palmer-Chalker states that are degenerate in their energy, for a given field direction and magnitude. The shaded grey box represents energy scales below the zero-field Monte Carlo critical temperature of $T_c \approx 160$ mK. The chosen wavevectors are taken from the Brillouin zone of the FCC lattice. Note that some curves may overlap at high-symmetry points or due to their degeneracies in a field (e.g. $\langle xy \rangle_h$ and $\langle \bar{x}\bar{y} \rangle_h$ for $B \geq 0.82$ T along the [100] direction).

- $4 < L < 10$,
- $10^6 \leq t_m \leq 5.10^7$ MCS,
- 100 different temperatures (regularly spaced) between 0 and 200 mK for parallel tempering.

Please note that different exchange parameters for $\text{Er}_2\text{Sn}_2\text{O}_7$ have been investigated, within the error bars of Ref. [16]. In particular, a systematic search in the [111] direction has shown a consistent increase of the transition temperature between 0 and 0.4 T, confirming the robustness of the reentrance in this exchange-parameter region.

Analysis of the [110] results

Here we discuss the Monte Carlo phase diagram in a [110] field [Fig. 3.2(b) of the main text]. There are two occurrences of reentrance, as well as a pronounced dip in T_c that occurs between them. As with the [100] and [111] phase diagrams, these three features can also be understood as originating from soft modes that arise at the merging of $T = 0$ FEPC states. In this field and at $T = 0$, the six FEPC states do not all minimize the energy (for reasons discussed later on in this section). Therefore, when determining the merging of FEPC states, we primarily consider those ground states which simultaneously minimize the energy [as shown in Fig. 3.8(e)], since these are the states the system can be found in. Hence, as B is increased from 0 and approaches a merging transition (between $\langle \bar{xz} \rangle_h$ and $\langle \bar{yz} \rangle_h$) around $B \approx 0.4$ T, soft modes arise [see Fig. 3.9(e)] and increase the thermal fluctuations within the ordered phase, producing the first (lower) reentrance. As B continues to increase to and above $B \approx 0.42$ T, however, the merging FEPC states that provided these soft modes (namely, $\langle \bar{xz} \rangle_h$ and $\langle \bar{yz} \rangle_h$) are no longer energetically preferred [see Fig. 3.8(e) and Fig. 3.9(f)]. These soft modes are therefore removed from the system, taking away their entropic support and producing a dip in T_c . As B is increased further and enters the region $0.57 \text{ T} < B < 1.12 \text{ T}$, soft modes still arise [Fig. 3.9(g)], although there are no merger transitions between FEPC ground states, only between ground and excited

states [Fig. 3.8(e)]. These soft modes give rise to the second (upper) reentrance. Since they are sustained for a range of B , the upper reentrant lobe is broad in the B direction.

Although the mechanisms of reentrance are similar to the other two directions, the mean field theory results for the [110] field direction do stand out among the three field directions we studied, given that the zero temperature phases differ from those at finite temperature. The objective of the remainder of this section is to clarify this difference.

Consider very low temperatures $T = \epsilon$ where $\epsilon \rightarrow 0^+$. When $T = 0$ exactly, Eq. (3.9) reduces to just the energy, whereas Eq. (3.11) implies that $\mathbf{m}_{ia} = \frac{\mathbf{H}_{ia}}{|\mathbf{H}_{ia}|}$. For $T = \epsilon$, $\mathbf{m}_{ia} \approx \frac{\mathbf{H}_{ia}}{|\mathbf{H}_{ia}|}$. As well, the free energy now gains a contribution from the entropy, namely $-\frac{1}{N\beta} \sum_{i,a} \ln(Z_{ia})$. Using $A_{ia} = \beta|\mathbf{H}_{ia}|$ in the partition function:

$$\begin{aligned} -\frac{1}{N\beta} \sum_{i,a} \ln(Z_{ia}) &= -\frac{1}{N\beta} \sum_{i,a} \ln\left(\frac{4\pi}{\beta|\mathbf{H}_{ia}|} \sinh(\beta|\mathbf{H}_{ia}|)\right) \\ &= -\frac{\epsilon}{N} \sum_{i,a} \ln\left(\frac{4\pi\epsilon}{|\mathbf{H}_{ia}|}\right) + \ln\left(\sinh\left(\frac{|\mathbf{H}_{ia}|}{\epsilon}\right)\right). \end{aligned}$$

As $\epsilon \rightarrow 0^+$, $\epsilon \ln(\epsilon) \rightarrow 0$ as well. Hence, the first term in the above summation is not an important contribution to the entropy at $T = 0^+$. On the other hand, $\sinh\left(\frac{|\mathbf{H}_{ia}|}{\epsilon}\right)$ scales roughly as $e^{\frac{|\mathbf{H}_{ia}|}{\epsilon}}$ for $\epsilon \rightarrow 0^+$, and hence,

$$-\frac{1}{N\beta} \sum_{i,a} \ln(Z_{ia}) \approx -\frac{\epsilon}{N} \sum_{i,a} \ln\left(e^{\frac{|\mathbf{H}_{ia}|}{\epsilon}}\right) \approx -\frac{1}{N} \sum_{i,a} |\mathbf{H}_{ia}|. \quad (3.23)$$

When temperature becomes finite, the entropic contribution is therefore related to the average magnitude of the local fields.

As shown in Eq. (3.8), there are two contributions to this local field: the local field resulting from the exchange between moments, and the local field resulting from the Zeeman coupling to the applied field \mathbf{B} . When $\mathbf{B} = 0$, only the first contribution is active. For the exchange parameters used here, the exchange couplings create local fields that move the spins into their Palmer-Chalker states, hence making these the ground state configurations. When B is turned

on, we must consider the second contribution, given by Eq. (3.4). Assuming a pure easy-plane anisotropy on each sublattice, there are four g -tensors to consider [1]:

$$\begin{aligned} \vec{g}_0 &= \frac{g_\perp}{3} \begin{pmatrix} 2 & -1 & -1 \\ -1 & 2 & -1 \\ -1 & -1 & 2 \end{pmatrix}, \vec{g}_1 = \frac{g_\perp}{3} \begin{pmatrix} 2 & 1 & 1 \\ 1 & 2 & -1 \\ 1 & -1 & 2 \end{pmatrix}, \\ \vec{g}_2 &= \frac{g_\perp}{3} \begin{pmatrix} 2 & 1 & -1 \\ 1 & 2 & 1 \\ -1 & 1 & 2 \end{pmatrix}, \vec{g}_3 = \frac{g_\perp}{3} \begin{pmatrix} 2 & -1 & 1 \\ -1 & 2 & 1 \\ 1 & 1 & 2 \end{pmatrix}. \end{aligned}$$

For a [110] field, a remarkable coincidence occurs: the Zeeman contribution $\mu_B g_{ia}^{\mu\nu} B^\nu$ for two sublattices (namely, sublattices 1 and 2) lie within the xy plane, exactly parallel to the spin configuration of the $\langle xy \rangle$ and $\langle \overline{xy} \rangle$ Palmer-Chalker states in Table 3.1. As such, for low fields in the [110] direction, these spins *do not* cant out of their original positions; the local fields from the exchange and Zeeman contributions add in parallel. Returning to Eq. (3.23), this lack of canting is the origin of the slight entropy difference between the Palmer-Chalker states that lie in the xy -plane (where the two contributions add in parallel) and out of the xy -plane (where the two contributions are not parallel). A similar discrepancy should be expected at $T = 0$: $\mathbf{m}_{ia} = \frac{\mathbf{H}_{ia}}{|\mathbf{H}_{ia}|}$ at $T = 0$, so this lack of canting will discriminate between the xy -planar and non- xy -planar states. This effect is therefore the origin of the difference between the $T = 0$ and $T = 0^+$ phases. It should be noted that this is *not* an order-by-disorder effect. The \mathbb{Z}_2 symmetry found at low fields and at $T = 0^+$ is not a subset of the original \mathbb{Z}_4 symmetry found at low fields and at $T = 0$. Rather, the \mathbb{Z}_2 symmetry corresponds to the two xy -planar Palmer-Chalker states, whereas the \mathbb{Z}_4 symmetry corresponds to the *other* four Palmer-Chalker states.

Lastly, Fig. 3.10 shows the multiplicity of the FEPC spin configurations *without* considering the free energy degeneracies. As such, it is not a true phase diagram of the system, but it reveals how the FEPC are changing as the field and temperature are varied, without considering which states actually minimize the free energy. It demonstrates that there *is* a merging of FEPC

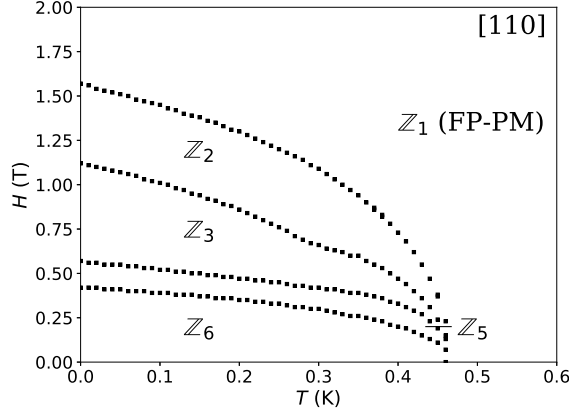


Figure 3.10: Diagram denoting the discrete symmetry of each phase as a function of field H and temperature T within mean field theory, for the $[110]$ field direction. Note that the free energies of each FEPC state is not considered here. Hence this is not a true phase diagram but merely represents the degeneracy and merging of FEPC spin configurations.

states occurring in the system, in agreement with Fig. 3.8(e). Whether or not these merging FEPC states have soft modes that influence the system depends on whether these FEPC states minimize the free energy and hence are actually selected within simulations, as explained in the main text. Nevertheless, even if free energy considerations complicate which FEPC states are merging and which soft modes are active, Fig. 3.10 shows that mergers are still the origin of soft modes in the $[110]$ field.

Monte Carlo simulations at low field in the $[110]$ direction

At low field in the $[110]$ direction, there are four FEPC ground states $\{\langle xz \rangle_h, \langle yz \rangle_h, \langle \overline{xz} \rangle_h, \langle \overline{yz} \rangle_h\}$ and two FEPC excited states $\{\langle xy \rangle_h, \langle \overline{xy} \rangle_h\}$ [see Fig. 3.8]. The very small energy gap between them means that it is not obvious which order is stabilised at finite temperature.

The easiest way to differentiate between the ground and excited states in Monte Carlo simulations is via the z -component of the Palmer-Chalker order parameter, m_{PCz} [see Fig. 3.11(a,b,c) panels]. m_{PCz} is finite for the two excited states, while it is zero for the four ground states. We show that as the system size is increased, m_{PCz} vanishes for $B = 0.1$ and 0.15 T, which means the FEPC excited states are not stable for $B \gtrsim 0.1$ T. For $B = 0.05$ T on the other hand, simulations are difficult to thermalize and the evolution with system size is not monotonic. Hence,

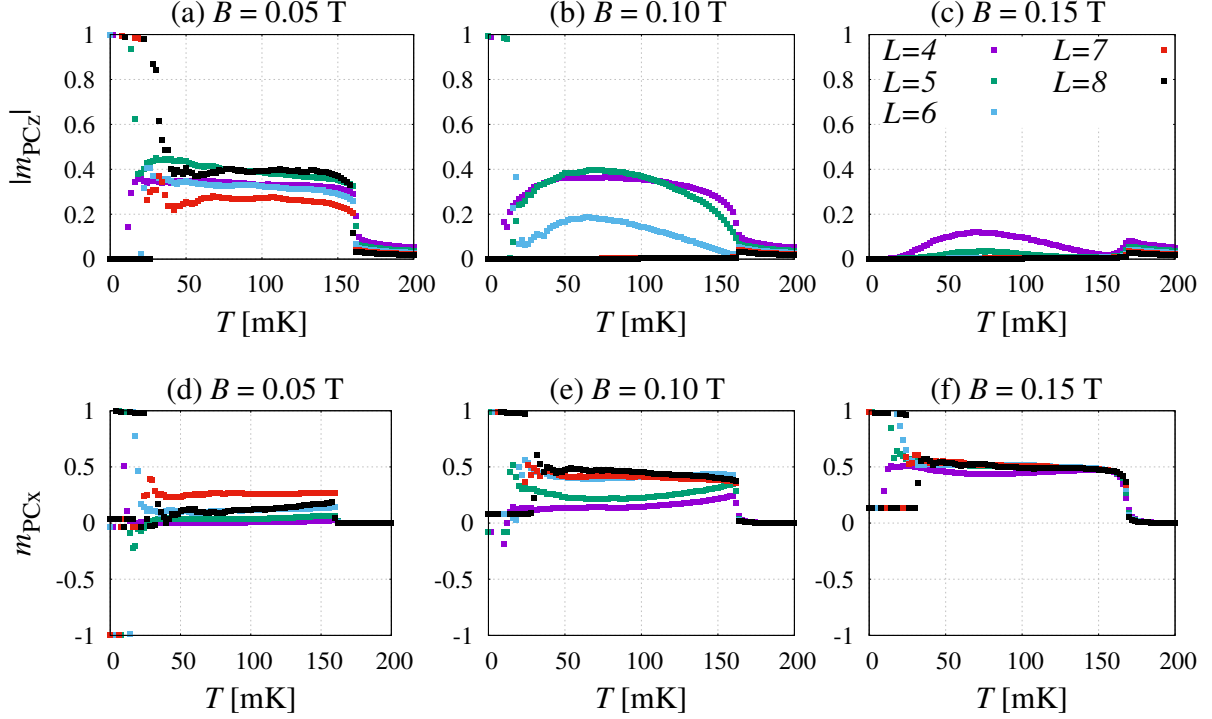


Figure 3.11: Differentiation between the ground and excited states in Monte Carlo simulations via the z -component of the Palmer-Chalker order parameter, $m_{\text{PC}z}$ (a,b,c). $m_{\text{PC}z}$ is finite for the two excited states, while it is zero for the four ground states. Here we show that as the system size is increased, $m_{\text{PC}z}$ vanishes for $B = 0.1$ and 0.15 T, which means the FEPC excited states are not stable for $B \gtrsim 0.1$ T. For $B = 0.05$ T on the other hand, simulations are difficult to thermalize and the evolution with system size is not monotonic. As for the four FEPC ground states, they can be divided into two pairs. For $\langle \bar{x}\bar{z} \rangle_h$ and $\langle \bar{y}\bar{z} \rangle_h$, the x -component of the Palmer-Chalker order parameter is positive, $m_{\text{PC}x} > 0$. For $\langle xz \rangle_h$ and $\langle yz \rangle_h$, $m_{\text{PC}x} < 0$. As shown in panels (d,e,f), $m_{\text{PC}x}$ always gets more positive for large system sizes, which means that the Z_2 states at low [110] field are $\langle \bar{x}\bar{z} \rangle_h$ and $\langle \bar{y}\bar{z} \rangle_h$. At very low temperatures, $T < 40$ mK, the data split into two groups because of the broken ergodicity in simulations between $\langle \bar{x}\bar{z} \rangle_h$ and $\langle \bar{y}\bar{z} \rangle_h$. All of these simulations were done for $t_m = 5.10^7$ Monte-Carlo steps.

we cannot rule out the presence of the FEPC excited states at finite temperature, as predicted by mean field theory in the previous section. That being said, this possible co-existence would only arise at very low field, $B \lesssim 0.1$ T, and thus not affect the mechanism for reentrance.

As for the four FEPC ground states, they can be divided into two pairs. For $\langle \bar{x}\bar{z} \rangle_h$ and $\langle \bar{y}\bar{z} \rangle_h$, the x -component of the Palmer-Chalker order parameter is positive, $m_{\text{PC}x} > 0$. For $\langle xz \rangle_h$ and $\langle yz \rangle_h$, $m_{\text{PC}x} < 0$. As shown in panels (d,e,f), $m_{\text{PC}x}$ always gets more and more positive for large system sizes, which means that the Z_2 states at low [110] field are $\langle \bar{x}\bar{z} \rangle_h$ and $\langle \bar{y}\bar{z} \rangle_h$. At very low temperatures, $T < 40$ mK, the data split into two groups because of the broken ergodicity

in simulations between $\langle \overline{xz} \rangle_h$ and $\langle \overline{yz} \rangle_h$. Please note, all of these simulations were done for $t_m = 5.10^7$ Monte-Carlo steps.

Monte Carlo simulations in the [111] direction

In Figure 3.12, we reproduce the phase diagrams in a [111] field as signalled via the Palmer-Chalker and Γ_5 order parameters, as well as the quantity $m_{6\phi}$ (defined below) to differentiate between ψ_2 and ψ_3 states. The contour of the phase diagram is clearly visible in panels (a) and (b). However, as explained in the main text, in order to understand the reentrance at $B \sim 0.5$ T, we need to consider the evolution of the angle ϕ . The ψ_2 (ψ_3) states are characterized by $\phi \equiv n\pi/3 (+\pi/6)$ for $n = 0, \dots, 5$. Hence, the quantity $m_{6\phi} \equiv m_{\Gamma_5} \cos(6\phi)$ is equal to +1 (-1) for ψ_2 (ψ_3) states. The yellow region at finite temperature for $B \sim 0.5$ T thus indicates the dominance of ψ_2 order in this region, as discussed in the main text. All of these simulations were done for $L = 6$ and $t_m = 5.10^7$ Monte-Carlo steps.

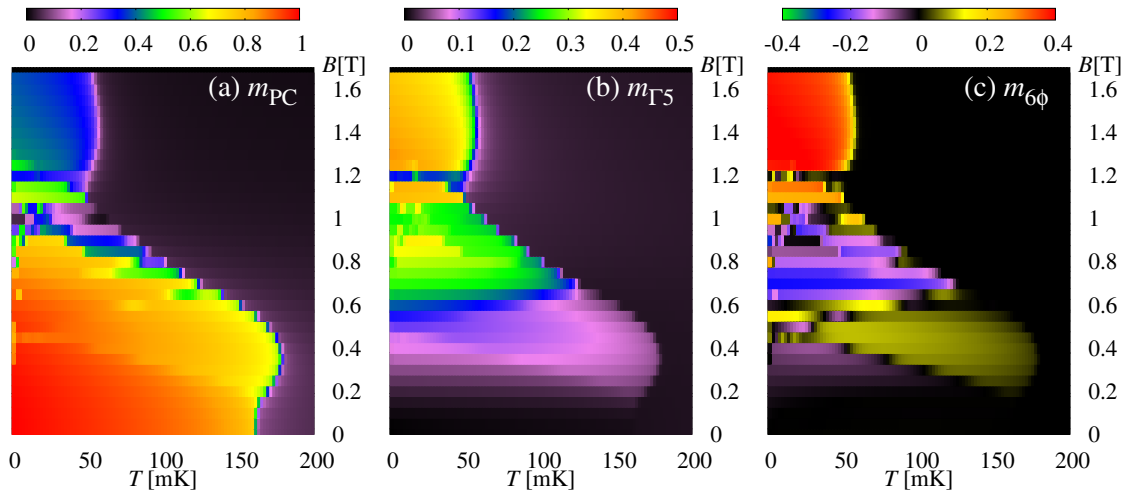


Figure 3.12: Here we reproduce the phase diagrams in a [111] field as signalled via the (a) Palmer-Chalker and (b) Γ_5 order parameters, as well as the quantity (c) $m_{6\phi}$ (defined above) to differentiate between ψ_2 and ψ_3 states.

Paper acknowledgements

We acknowledge Natalia Perkins for useful discussions and Rob Mann for comments on reentrance in black holes. We thank Allen Scheie and Tom Hogan for their help with analyzing the long pulse measurements, and acknowledge the use of the LongHCPulse program for this analysis. We acknowledge the support of the National Institute of Standards and Technology, U.S. Department of Commerce, in providing the neutron research facilities used in this work. This research was partially supported by CIFAR. DRY, KAR, and JWK acknowledge funding from the Department of Energy award DE-SC0020071 during the preparation of this manuscript. The work at the University of Waterloo was supported by the Natural Sciences and Engineering Research Council (NSERC) and by the Canada Research Chairs Program (MJPG, Tier 1). LDCJ acknowledges financial support from CNRS (PICS No. 228338) and from the French “Agence Nationale de la Recherche” under Grant No. ANR-18-CE30-0011-01. We thank I. Zivkovic and R. Freitas for providing us their C_p data previously published in Ref.[15].

3.5 Ongoing work

The purpose of continuing this work is twofold: First, we would like to accurately determine the exchange parameters of the relative Hamiltonian in order to quantitatively compare our phase diagram to theoretical models. Second, we need to find evidence of the spin-wave mode softening related to the reentrant feature to corroborate our theory of reentrance. We have explored both of these through inelastic neutron scattering at the Cold Neutron Chopper Spectrometer (CNCS) at Oak Ridge National Laboratory, the details of which are described below.

Determination of relative exchange parameters

As introduced in Ref. [37], we can determine the interaction parameters of the pyrochlore Hamiltonian (Eqn. (3.1)) from field polarized paramagnetic neutron scattering using linear spin wave theory (LSWT). For this reason, we performed INS measurements on co-aligned single

crystals of $\text{Er}_2\text{Sn}_2\text{O}_7$ on the CNCS spectrometer at ORNL using a dilution insert and vertical field magnet. We aligned 22 single crystals (Figure 3.13) such that the field is applied along the $[1\bar{1}0]$ and we probe the HHL scattering plane. A total mass of approximately 50 mg with a mosaic spread of 4° was achieved. Measurements were performed at 0,3 and 7 T at base temperature of 0.05 mK with an incident energy of $E_i = 2.5$ meV (energy resolution at elastic line of 0.07 meV). The sample was rotated 180° with 2° steps about the vertical direction in order to probe a sufficient amount of the HHL plane.

We utilized the MATLAB package SpinW [190] to attempt to fit the four interaction parameters, J_{1-4} (making no assumptions about the strength of the DM interaction, J_4), using fixed g -values previously found from CEF measurements [38], $(g_\perp, g_\parallel) = (7.52, 0.054)$. Unfortunately, due to the large parameter space, a global best fit is not readily achieved. It is possible that $\text{Er}_2\text{Sn}_2\text{O}_7$ is similar to $\text{Yb}_2\text{Ti}_2\text{O}_7$ in that there is a line of best fit [117, 191], and non-linear least squares fits only show shallow minima. We can, however, compare our experimental spin-wave results to the calculated spin-waves expected from the interaction parameters found from polycrystalline INS [16], which are

$$(J_1, J_2, J_3, J_4) = (+0.0696, +0.0753, -0.1064, +0.0372) \text{ meV}. \quad (3.24)$$

We see in Figure 3.13 b) and c) that the spin-wave dispersions associated with these interaction strengths do not accurately represent the single crystal data. This clearly shows that the determination of the actual interaction parameters is not only necessary to quantitatively model $\text{Er}_2\text{Sn}_2\text{O}_7$ and the field dependent phase diagram, but also to accurately place $\text{Er}_2\text{Sn}_2\text{O}_7$ on the ground state phase diagram. We are in the process of using exhaustive least squares fits, as well as non-linear regression alternatives such as Bayesian non-linear regression, to obtain a more accurate fit of the interactions. Additionally, undertaking an EPR measurement would be useful to corroborate the g -values, as the fit is highly susceptible specifically to the exact value of g_\parallel .

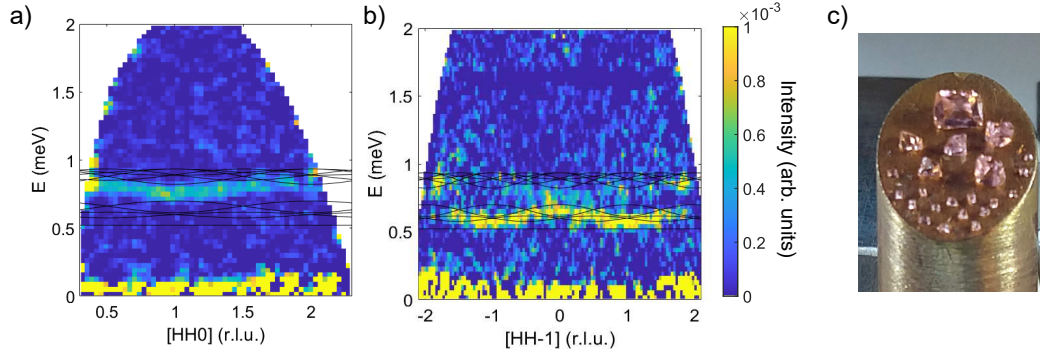


Figure 3.13: Spin-wave scattering of $\text{Er}_2\text{Sn}_2\text{O}_7$ in the field polarized state with an applied field of 3 T (7 T background subtracted) and $T \approx 0.05$ K in the a) HH0 and b) $\text{HH}\bar{1}$ planes. Incident energy was 2 meV and the calculated spin-wave dispersions using the parameters from Ref. [16]. c) Co-aligned single crystals used for this study, with a total mass around 50 mg.

Spin-wave mode softening

The smoking gun to verify our theory that reentrance is linked to soft modes is the detection of the spin-wave mode softening. Therefore, we performed another INS experiment on CNCS using the same co-aligned single crystals as the previous measurement. To see the mode softening, an incident energy of $E_i = 1.55$ meV with energy resolution of 0.02 meV was utilized. From the spin-wave calculations, in a $[1\bar{1}0]$ field we expect to see mode softening up to the dip in the phase diagram, where the soft modes suddenly disappear (Figure 3.9 e-g). For this reason, we measured the spin-waves with an applied field of 0.5, 0.65, and 0.75 T with 5 T used for background subtraction. The sample was rotated through 90° with 2° steps such that the $[111]$ and $[002]$ zone centers were covered.

Importantly, we do find evidence of mode softening as the field is increased from 0.5 T to 0.65 T. This can be seen in the high-field subtracted energy vs. intensity cut shown in Figure 3.14 a) and b). Further analysis, including more cuts around zone centers, careful folding for better statistics, and a more robust background subtraction, are needed to make absolute conclusions about the softening. However, we did not see the disappearance of the soft modes. In addition to the softening, we find an unexpected intervening magnetic order, reminiscent of a $(\frac{1}{2}\frac{1}{2}\frac{1}{2})$ order, as is seen in the elastic slice in Figure 3.14 c) and d) at 0.5 T. This is perhaps another

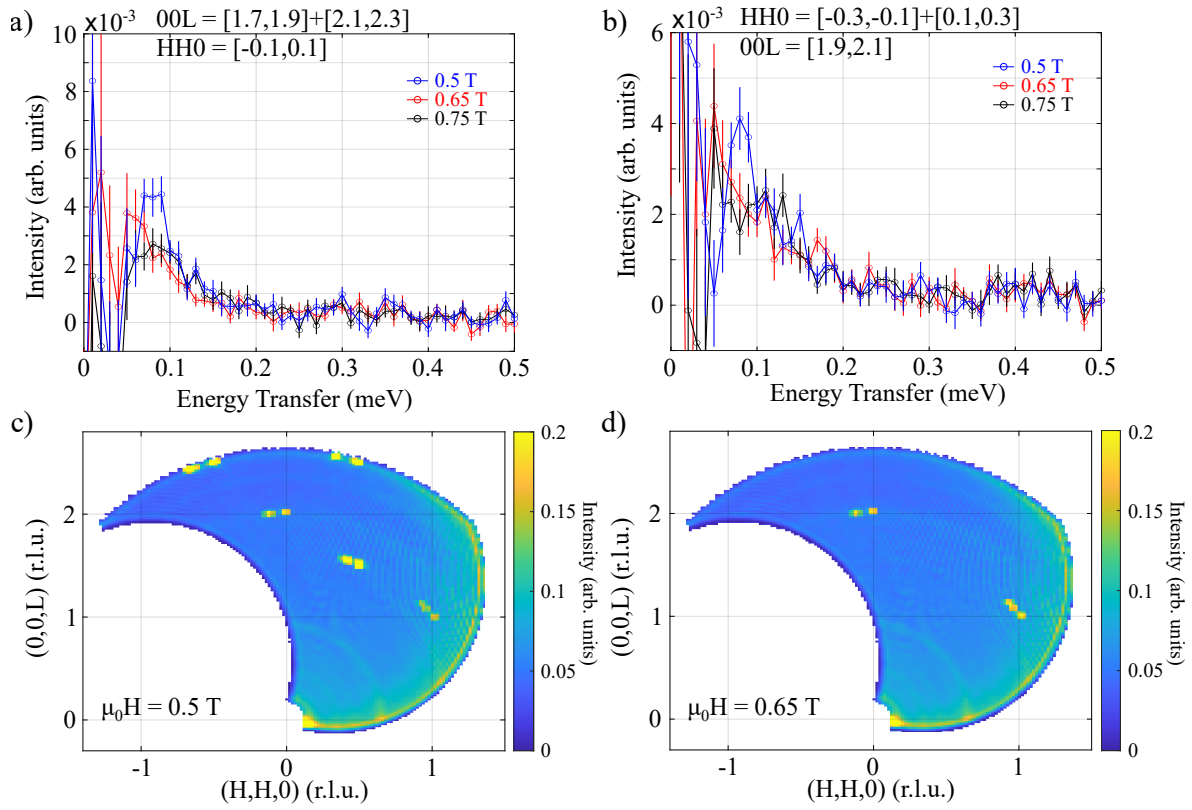


Figure 3.14: Field dependent energy vs. intensity cuts around the [002] zone centers, 5 T background subtracted. a) Cut along $[0, 0, 2 \pm 0.2]$ and b) $[0 \pm 0.2, 0 \pm 0.2, 2]$ showing the spin wave softens above 0.5 T. The elastic line (not background subtracted) at c) 0.5 T and d) 0.65 T shows an intervening $(\frac{1}{2}, \frac{1}{2}, \frac{1}{2})$ phase.

manifestation of phase competition that is linked to reentrance, although further theoretical investigations are necessary.

Chapter 4

Dipolar correlations found in candidate octupolar spin ice $\text{Ce}_2\text{Sn}_2\text{O}_7$

4.1 Context

This chapter consists of a manuscript in preparation for publication on the discovery of diffuse dipolar correlations found from neutron diffraction measurements in the candidate octupolar spin ice material $\text{Ce}_2\text{Sn}_2\text{O}_7$. The full authorship is:

D. R. Yahne, B. Placke, R. Schaefer, O. Benton, M. Powell, J. W. Kolis, C. Pasco, A. F. May, E. M. Smith, B. D. Gaulin, M. D. Frontzek, S. A. Calder and K. A. Ross, [unpublished] (2022).

Contributions

Single crystal samples were synthesized by L. D. Sanjeeva, M. Powell and J. W. Kolis. Polycrystalline samples of $\text{Ce}_2\text{Sn}_2\text{O}_7$ were synthesized by M. Powell and J. W. Kolis, while samples of $\text{Ho}_2\text{Ti}_2\text{O}_7$ were synthesized by D. R. Yahne and T. Wecker. Single crystal heat capacity measurements were performed by D. R. Yahne under the supervision of K.A. Ross. Powder heat capacity measurements were performed by C. Pasco under the supervision of A. F. May. D. R. Yahne measured the powder neutron diffraction pattern with assistance from beamline scientists S. Calder and M. Frontzek. D. R. Yahne also performed a mail-in PDF measurement with assistance from the NOMAD team. RMC calculations were performed by D. R. Yahne with the assistance of J. A. M. Paddison. In progress numerical linked cluster calculations are being carried out by B. Placke, R. Schaefer, and O. Benton. All work performed on sister compound $\text{Ce}_2\text{Zr}_2\text{O}_7$ was undertaken by E. M. Smith and B. D. Gaulin. The paper was written by D. R. Yahne, S. Calder, and K. A. Ross.

4.2 Research Article

Introduction

The rare-earth pyrochlores, $R_2M_2O_7$, where R^{3+} is a rare-earth ion and M^{4+} can be a range of transition metal ions, host a wealth of exotic phenomena due to their canonical frustrated geometry, range of single-ion anisotropy, and the ability to map to a pseudo-spin- $\frac{1}{2}$. The subtle and complex interplay of anisotropic exchange, dipolar interactions, and higher order effects, can stabilize a variety of different ground states from classical spin ice, to the highly entangled quantum spin liquid (QSL) [26, 33, 147, 148]. Even when displaying more conventional ground states, such as long-range order, many of the rare-earth pyrochlores lie on phase boundaries between different ordered phases [1, 16, 191, 192, 193], and the ability to tune across these boundaries through chemical pressure, disorder, or anisotropy, makes the rare-earth pyrochlores a model system for finding unconventional physics.

In the heavy $4f$ rare-earth magnets, the single ion physics dominates over two-ion interactions, with the hierarchy of Coulomb interactions and spin-orbit coupling, followed by crystal field (CEF) effects from the surrounding charged environment. The CEF breaks the degenerate free-ion ground state, and in the case of the pyrochlore oxides of interest, leads to a ground state doublet that can be classified how it transforms under the point group symmetry group and time reversal symmetry [33]. The doublets resulting from non-Kramers' ions (even number of electrons) are described by a pseudo-spin, where one component transforms like a magnetic dipole, and the other two transform as magnetic quadrupoles. For Kramers' ions (odd number of electrons), there are two classes of doublets, one where all components of the pseudo-spin transform as magnetic dipoles and therefore behaves identically to a spin- $\frac{1}{2}$, and the "dipolar-octupolar" (DO) doublet, where two components transform as a magnetic dipole and the other component transforms as a magnetic octupole.

DO pyrochlores, where $R = \text{Ce, Sm, or Nd}$, occur when the single-ion ground state doublet is described by only the $|\frac{3m}{2}\rangle$ states ($m = 1, 3, 5, \dots$). The low energy physics of the DO pyrochlores can be described by a simple XYZ Hamiltonian [33, 34],

$$H_{XYZ} = \sum_{\langle i,j \rangle} \left[J_{\tilde{x}} S_i^{\tilde{x}} S_j^{\tilde{x}} + J_{\tilde{y}} S_i^{\tilde{y}} S_j^{\tilde{y}} + J_{\tilde{z}} S_i^{\tilde{z}} S_j^{\tilde{z}} \right] - g_z \mu_B \sum_i \mathbf{h} \cdot \hat{\mathbf{z}}_i (S_i^{\tilde{z}} \cos \theta + S_i^{\tilde{x}} \sin \theta), \quad (4.1)$$

where $S^{\tilde{\alpha}}$ are the pseudospin components in the local $\tilde{\alpha} = \tilde{x}, \tilde{y}, \tilde{z}$ coordinate frame (related to the local x, y, z coordinate frame by a rotation of θ about the y axis), g_z is the g-factor, \mathbf{h} is the magnetic field, and $\hat{\mathbf{z}}_i$ is the local anisotropy axis. The resulting zero field ground state phase diagram reveals a large parameter region hosts either an octupolar or dipolar QSL phase [4]. Recently, experimental work has highlighted $\text{Ce}_2\text{Zr}_2\text{O}_7$ and $\text{Ce}_2\text{Sn}_2\text{O}_7$ as QSL candidates [3, 18, 42, 45, 46]. Extensive neutron scattering, heat capacity, and theoretical calculations have constrained $\text{Ce}_2\text{Zr}_2\text{O}_7$ to lie within the $U(1)_\pi$ QSL state at low temperatures, on a boundary between octupolar and dipolar character. Similarly, neutron scattering measurements were performed on $\text{Ce}_2\text{Sn}_2\text{O}_7$ and revealed broad diffuse scattering at high scattering vectors, a signal attributed to an octupolar spin ice or higher order multipoles [18, 194]. This difference in ground states is surprising given the chemical similarities between $\text{Ce}_2\text{Zr}_2\text{O}_7$ and $\text{Ce}_2\text{Sn}_2\text{O}_7$, and perhaps points to a method of phase boundary tuning.

Along the same vein, many pyrochlores are sensitive to disorder effects, which can result in vastly different ground states of nominally the same system, the most famous example being that of $\text{Yb}_2\text{Ti}_2\text{O}_7$ [195, 196, 197, 198, 199]. Ce-based pyrochlores are likely no exception to this, as the non-magnetic Ce^{4+} oxidation state is stable and are thus potentially more prone to oxidation effects than other pyrochlore systems. Therefore, great care must be taken during the synthesis and analysis of Ce-based pyrochlores to accurately assess the physics at hand.

Experimental Methods and Results

Single crystal and powder samples of $\text{Ce}_2\text{Sn}_2\text{O}_7$ were grown via a hydrothermal synthesis method [176]. The benefit of hydrothermal synthesis is that it requires significantly lower temperature and can therefore avoid the effects of the volatile tin oxide. Approximately 13 grams of the pyrochlore stannate was prepared using a mixture of 30–50% SnO (Sn^{4+}) and 70–50% SnO_2 (Sn^{2+}) in order to reduce any residual Ce^{4+} to Ce^{3+} , thus minimizing the external impurities. We

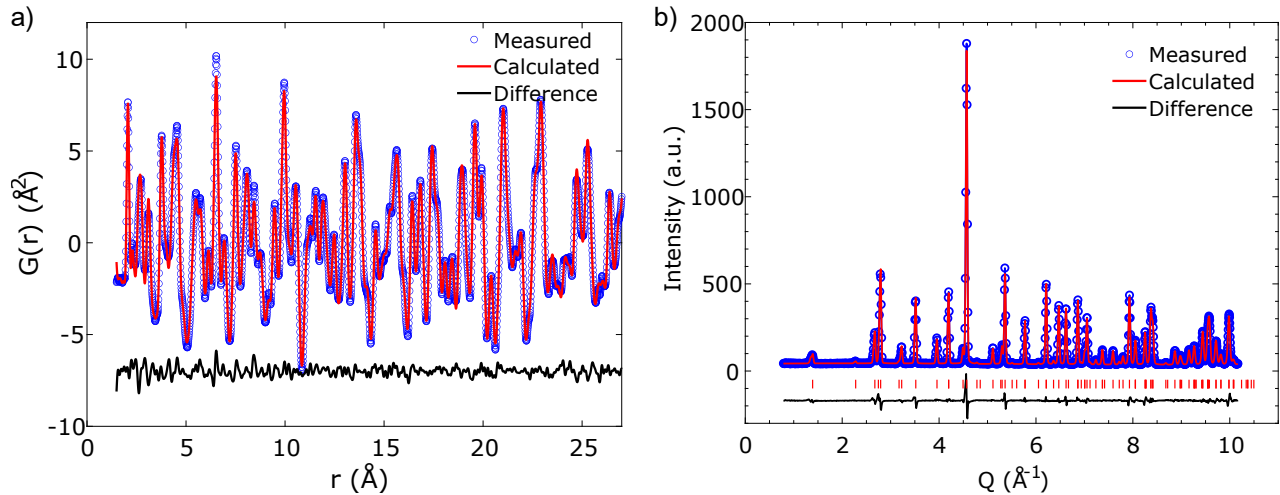


Figure 4.1: a) PDF analysis of $\text{Ce}_2\text{Sn}_2\text{O}_7$ from total neutron scattering data taken on the NOMAD beamline at room temperature. The Fourier transform and background subtraction was performed using the PDFgetN3 program, and Rietveld refinement utilized the PDFgui software. The fitted curve (red) shows good agreement with the data, indicating no local distortions in the sample. The slight disagreement at small neighbor distances is due to the asymmetric peak shape on NOMAD [17]. b) Room temperature powder neutron diffraction on beamline HB-2A, and refined parameters can be found in Table 4.1.

expect there to be negligible stuffing of the A-site Ce^{3+} on the B-site Sn^{4+} due to the large size difference (1.01 vs. 0.69), unlike Yb and Ti, (0.87 vs. 0.61) in $\text{Yb}_2\text{Ti}_2\text{O}_7$. Additionally, such stuffing would create a corresponding defect in the oxide lattice, leading to a noticeable change in color. Our powders are bright yellow with a green tint (Fig. 4.3 d), showing no evidence of oxidation effects while in air, in stark contrast to the sister compound $\text{Ce}_2\text{Zr}_2\text{O}_7$ which turns black on the order of hours. Furthermore, we have collected temperature dependent full-sphere single crystal x-ray data sets at 100, 200, and 300 K. We refined the oxygen atoms on lower symmetry sites and see no flattening or movement of the thermal ADP's, suggesting little to no evidence of defects in the oxide lattice to any measurable concentration. The refined lattice parameter of $10.6464(4) \text{\AA}$, within 0.01\AA of that found in Ref. [44] and Ref. [18], also suggests minimal oxidation has occurred. The remaining question is whether there is evidence of Ce^{4+} stuffing on Sn^{4+} sites, which is possible given the comparable ionic radii (0.87 vs. 0.69). Our x-ray refinement places an upper bound of 3% or less Ce^{4+} on the B-site, but the x-ray sensitivity precludes us from determining the exact percentage of stuffing.

Room temperature powder neutron diffraction (PND) measurements were performed on beamlines HB-2A at the High Flux Isotope Reactor (HFIR) and NOMAD at the Spallation Neutron Source (SNS) at Oak Ridge National Laboratory (ORNL). Room temperature PND on HB-2A (Figure 4.1 b) utilized the Ge(115) monochromator for an incident wavelength of 1.54 Å, and the resulting diffraction pattern was refined using the Fullprof software suite which implements the Reitveld refinement method [138]. We find a lattice parameter of 10.64542(5) Å, in agreement with our single crystal x-ray diffraction. A small non-magnetic impurity of CeO₂ is present, and makes up ~ 3% of the material by weight. The total scattering measurement on NOMAD, with a $Q_{\max} = 40 \text{ \AA}^{-1}$, allows an atomic pair distribution function (PDF) analysis to be performed to further constrain the local structure of our sample (Figure 4.1 a). The PDF gives an atom by atom histogram of all of the pair-pair correlations in a material as a function of real-space distance r . We utilized PDFgetN3 and PDFgui [200, 201] to process the data and perform the PDF refinement, respectively. Through this, we found a similar lattice parameter as HB-2A, and there was no evidence of significant local structure distortions. We note that the poor fit in the low- r region in real space is due to the asymmetry in the NOMAD peak shape in reciprocal space [17], i.e. it is an artifact of the Fourier transform performed during the PDF analysis and is not intrinsic to the sample.

Heat capacity measurements were performed on a single crystal of Ce₂Sn₂O₇ (Fig. 4.2 a) down to 50 mK using a Quantum Design PPMS with dilution insert, and similar measurements on powder were performed down to 1.8 K. Our single crystal results differ from literature, but we note that the entropy, found from extending the data using a power law extrapolation to zero at $T = 0$, plateaus near the expected value of $R \ln(2)$ for a well-isolated Kramers' doublet ground state (Fig. 4.2 b), while Ref. [18] does not. This stark contrast is indeed surprising, as the author's of Ref. [18] took great care in surveying the level of disorder in their sample through atomic PDF and thermogravimetric analysis. Nevertheless, in agreement with Ref. [18], we *do not* find evidence of a transition to long-range order down to 50 mK. We see a broad peak in the heat capacity, the shape of which is similar to that of the sister compound Ce₂Zr₂O₇, although

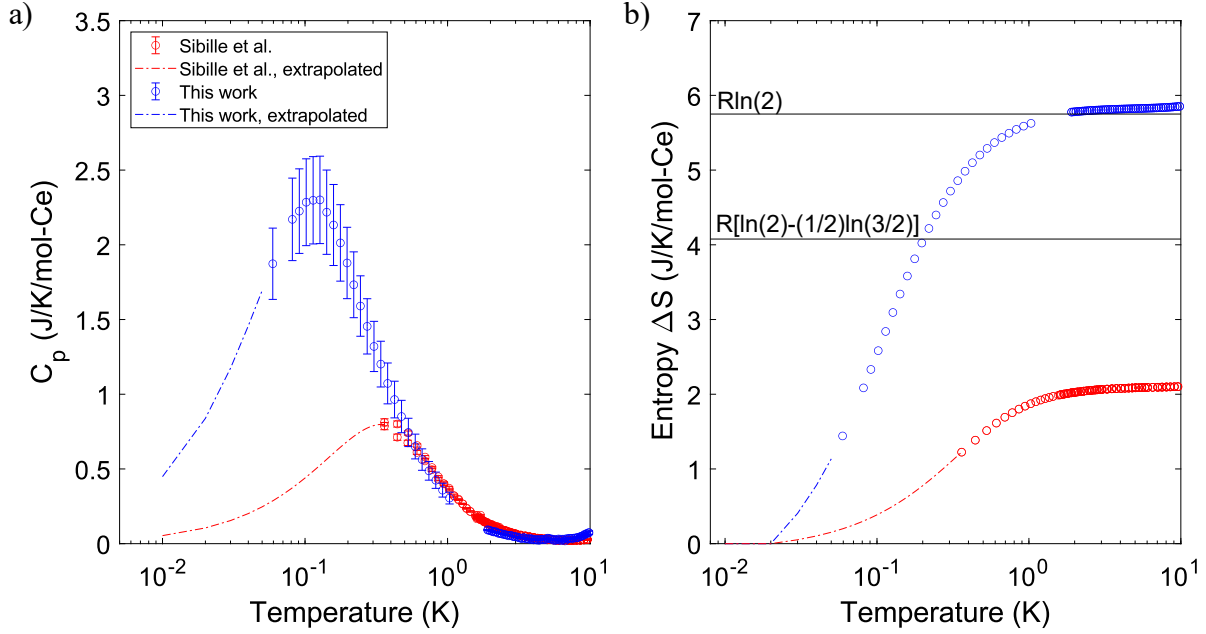


Figure 4.2: a) Single crystal heat capacity compared to previously published polycrystalline data by Ref. [18]. Power law extrapolations down to 0 K were utilized to achieve a reasonable estimate of the entropy. Please note that the data presented here is the total heat capacity (not lattice subtracted), while the Sibille *et. al* data is C_{mag} , however, the phonon contribution at low temperature is expected to be quite low and thus should not affect the conclusions of this work. b) The entropy recovered over the full temperature range, showing our work plateaus at $R \ln(2)$, expected for a well-isolated single-ion doublet. The Pauling spin ice entropy is also shown.

shifted to lower temperature. Polycrystalline measurements were more challenging to obtain because the powder would not readily pelletize since it could not be sintered. Silver powder was added to equal mass of polycrystalline $\text{Ce}_2\text{Sn}_2\text{O}_7$ and pressed to form a pellet. After careful background subtraction, the powder heat capacity data was found to be in good agreement with the single crystal measurements within mass error.

We collected low temperature PND on WAND² using the Ge(113) monochromator, with incident wavelength of 1.488 Å, and a closed-cycle refrigerator with a base temperature of 0.3 K. The high flux and ³He position-sensitive detector makes WAND² an ideal instrument for probing weak, diffuse neutron signals that are expected for octupolar scattering at high- Q . However, we do not find any increase in intensity at high- Q , and instead, we find a diffuse signal at *low* scattering angle, reminiscent of a dipolar spin-ice (Figure 4.3 a). The temperature dependence

in Figure 4.3 b) suggests this low- Q diffuse scattering onsets near 1.5 K where we also see the initial increase in the heat capacity.

Discussion & Conclusions

Due to the apparent similarity of our diffuse signal with a dipolar spin ice, we performed Reverse Monte Carlo (RMC) using SPINVERT [202] to determine the number of tetrahedra that obey the 2-in-2-out ice rule. From simple counting statistics, we expect a lattice of perfectly random Ising spins to have 37.5% of tetrahedra that obey the ice rule, while, experimentally, a classical spin ice, like $\text{Ho}_2\text{Ti}_2\text{O}_7$, should have $\geq 80\%$. The RMC calculations find that $44.4 \pm 1.0\%$ of tetrahedra satisfy the ice rule in $\text{Ce}_2\text{Sn}_2\text{O}_7$, which indicates that there is only a slight favoring of the ice-rule configuration, but $\text{Ce}_2\text{Sn}_2\text{O}_7$ has clearly not ordered into a spin ice. It is likely that this is due to thermal fluctuations from not being cooled far enough in to the spin ice region, as the integrated intensity of the diffuse scattering is not fully saturated at the lowest measured temperature. We expect the diffuse intensity and number of tetrahedra in the spin-ice configuration would increase as the temperature is reduced further. Alternatively (or, perhaps, additionally), quantum fluctuations could be at play, or there may be a mixing (or crossover) between dipolar and octupolar spin ice that is unable to be modeled by the RMC program, both of which would act to decrease the number of tetrahedra that obey the ice rule.

It is surprising that we are unable to reproduce the high- Q diffuse scattering from nominally the same sample. The similarities between our work and that of $\text{Ce}_2\text{Zr}_2\text{O}_7$, however, could point to a dipolar QSL nature in $\text{Ce}_2\text{Sn}_2\text{O}_7$. The contrast of this to the previously discovered octupolar QSL of Ref. [18] corroborates that $\text{Ce}_2\text{Zr}_2\text{O}_7$ (and $\text{Ce}_2\text{Sn}_2\text{O}_7$) likely lies on a boundary between octupolar and dipolar character [3]. We are in the process of undertaking numerical linked cluster calculations to simultaneously fit the heat capacity, magnetic susceptibility, and neutron diffraction to constrain the interaction parameters and ultimate ground state. The sensitivity to disorder effects suggests $\text{Ce}_2\text{Sn}_2\text{O}_7$ could lie in proximity to many phase boundaries. Further studies to quantify the level of disorder in these samples is necessary to fully understand how to tune across these phase boundaries.

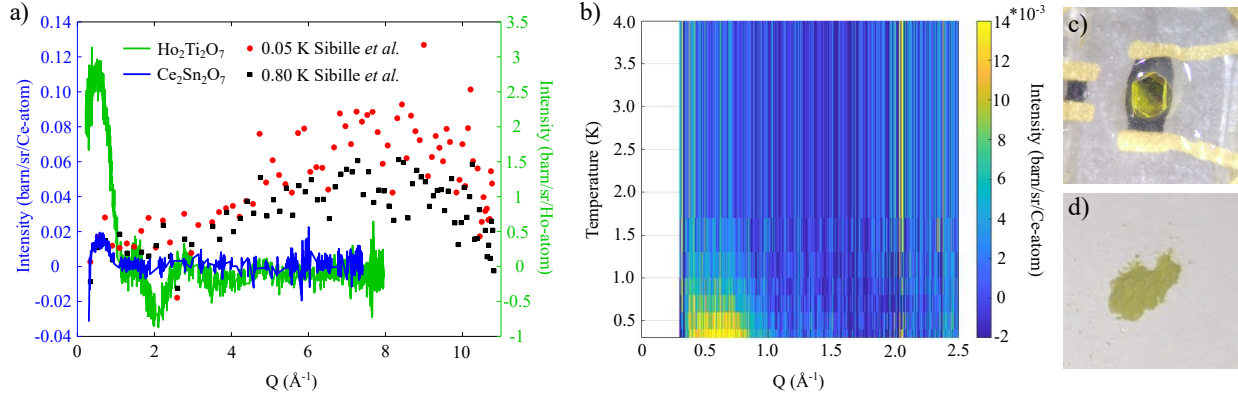


Figure 4.3: a) Diffuse neutron scattering from data taken on WAND² at 300 mK. All data has been converted to absolute units, and high temperature data was used for background subtraction. We compare the Ce₂Sn₂O₇ diffuse scattering to that of known dipolar spin ice material Ho₂Ti₂O₇, as well as the Ce₂Sn₂O₇ high-*Q* diffuse scattering found by Sibille *et al.* [18]. b) High temperature subtracted diffuse scattering as a function of temperature. The intensity increase near $Q = 0.6 \text{ \AA}^{-1}$ is clearly seen and onsets around 1.5 K. c) A single crystal of Ce₂Sn₂O₇ used for heat capacity measurements and d) the polycrystalline sample used for powder heat capacity and neutron diffraction measurements.

In summary, we have found diffuse scattering reminiscent of a *dipolar* spin ice in the *octupolar* spin ice candidate Ce₂Sn₂O₇. While the precise difference in the polycrystalline samples is currently unclear, the difference in ground state points to a strong sensitivity to disorder which needs to be investigated further through PDF or XAFS measurements. Our current understanding suggests that Ce₂Sn₂O₇ may be proximal to many phase boundaries, such as the dipolar/octupolar phase boundary, similar to Ce₂Zr₂O₇. Further investigations of Ce₂Sn₂O₇ and Ce₂Zr₂O₇ could help elucidate the effects of phase competition, as was recently done for the pyrochlore stannate Er₂Sn₂O₇.

Paper acknowledgements

This research used resources at the High Flux Isotope Reactor and the Spallation Neutron Source, DOE Office of Science User Facilities operated by the Oak Ridge National Laboratory. DRY, KAR, MP and JWK acknowledge funding from the Department of Energy award DE-SC0020071.

Table 4.1: Refined room temperature parameters for $\text{Ce}_2\text{Sn}_2\text{O}_7$ from neutron diffraction on HB-2A using the Fullprof Rietveld refinement.

Lattice parameter (\AA): 10.64542(5)				Space group: Fd-3m		Temperature: 300 K			
Atoms	x	y	z	B_{11}	B_{22}	B_{33}	B_{12}	B_{13}	B_{23}
Ce (16d)	0.75	0.75	0.5	0.0005(1)	0.0005(1)	0.0005(1)	-0.0031(10)	0.00031(10)	0.00031(10)
Sn (16c)	0.5	0.75	0.25	0.00019(10)	0.00019(10)	0.00019(10)	-0.00002(9)	-0.00002(9)	0.00002(9)
O (48f)	0.625	0.625	0.3307(1)	0.00089(8)	0.00089(8)	0.00076(10)	0.00047(11)	0	0
O (8b)	0.625	0.625	0.625	0.0009(2)	0.0009(2)	0.0009(2)	0	0	0
Lambda (\AA): 1.54		R_{Bragg} : 2.07		R_f : 1.34					

4.3 Supplemental Material

Neutron Rietveld Refinement Details

Room temperature neutron diffraction was performed on beamline HB-2A with an incident wavelength of $\lambda = 1.54\text{\AA}$ (Figure 4.1 b). Rietveld refinement using the Fullprof software suite was utilized for fitting the lattice parameters and occupancy, and the values of refined errors can be found in Table 4.1. A non-magnetic CeO_2 phase was necessary to account for some spurious peaks, and was found to make up less than 3% of the sample by weight. Refined parameters are found to be in agreement with Ref. [18] PND taken on the HRPT beamline at SINQ, Paul-Scherrer Institute.

Room temperature time-of-flight total scattering was performed on the NOMAD beamline, taking advantage of the mail-in program (Figure 4.1 a). The returned data was carefully background subtracted and given in $S(Q)$ and $G(r)$ for a variety of Q_{max} cut off values. Ideally, an infinite Q -range would be used for the Fourier transform from $S(Q) \rightarrow G(r)$, however this is obviously not possible. The maximum value of Q chosen will effect the real-space resolution (larger Q_{max} corresponds to higher resolution) as well as termination ripples. For this reason, we used a $Q_{\text{max}} = 40 \text{\AA}^{-1}$. The refined pattern and fitted lattice parameter of 10.6476\AA agrees well with the experimental data and therefore we do not have evidence of oxidation.

Chapter 5

Conclusion

This work explored the unique magnetism in three rare-earth based geometrically frustrated magnets, exemplifying the variety of exotic magnetism these systems can host due to the varying single-ion and exchange anisotropy. In Chapter 2, we introduced a quasi-2D isosceles triangular lattice material, $\text{K}_3\text{Er}(\text{VO}_4)_2$, where we find an unusual magnetic structure of alternating AFM layers with zero moment layers. Heat capacity measurements found this transition to long-range order occurs at 155 mK, and a full $R\ln(2)$ entropy is recovered which indicates that the odd magnetic structure is a fully ordered state. Therefore, we hypothesize that the structure is due to the strong XY single-ion anisotropy, suggested from magnetometry measurements, which acts to suppress the *ordered* out-of-plane pseudo-spin-1/2 magnetic moments. From the relation $\mu_i = g_{ii}S_i$, we propose that g_{zz} would be very small, such that neutron scattering does not detect any μ_z . Rotation magnetization and inelastic neutron measurements have been performed to corroborate this, however currently analysis can only confirm that $g_{zz} < g_{xy}$.

In Chapter 3 we used extensive heat capacity measurements and theoretical techniques, including classical Monte Carlo, mean field theory, and spinwave calculations, to elucidate the underlying mechanisms behind reentrance found in the field vs. temperature phase diagram of the effective spin-1/2 rare-earth pyrochlore oxide $\text{Er}_2\text{Sn}_2\text{O}_7$. These results indicate that reentrance is linked to soft modes arising from phase competition. The origin of the phase competition depends on the applied field direction, but stems from either the enhanced competition with the nearby Γ_5 AFM phase or from competing zero temperature field-evolved Palmer-Chalker ground states. In both cases, the soft modes enhance thermal fluctuations which cause the specific ordered phase to be entropically stabilized, thus forming a reentrant phase diagram. This work relied on the use of single crystals to explore the anisotropic nature of the reentrant phase diagram, and we have carried out further inelastic neutron scattering measurements to

both experimentally verify the existence of soft modes as well as to better constrain the ground state model.

Lastly, in Chapter 4, we explored the diffuse scattering of a dipolar-octupolar rare-earth pyrochlore oxide, $\text{Ce}_2\text{Sn}_2\text{O}_7$. We discovered that our neutron diffraction results were not in agreement with previous literature results, which originally placed $\text{Ce}_2\text{Sn}_2\text{O}_7$ within an octupolar quantum spin liquid ground state. After undertaking room temperature neutron diffraction and atomic PDF measurements to determine the sample quality, we find no obvious sample differences or distortions. It is unclear why the scattering from nominally the same material leads to strikingly different results. Nevertheless, our neutron diffraction resulted in a broad, diffuse signal at low scattering vectors, reminiscent of a *dipolar* spin-ice. The similarities to sister compound $\text{Ce}_2\text{Zr}_2\text{O}_7$ suggest that $\text{Ce}_2\text{Sn}_2\text{O}_7$ could lie on a phase boundary that is sensitive to minor disorder.

The study of these frustrated magnetic systems motivates further exploration of other rare-earth based geometrically frustrated magnets. While an experimental realization of a quantum spin liquid state is theoretically possible, higher order interactions often make this challenging. However, the potential for furthering our fundamental understanding of classical and quantum magnetism is readily achievable even when a QSL state is not realized. The zero moment layers of $\text{K}_3\text{Er}(\text{VO}_4)_2$ have allowed us to better understand the effects of single-ion anisotropy in a layered magnetic structure. The discovery of reentrance in $\text{Er}_2\text{Sn}_2\text{O}_7$ has allowed us to learn more about the effects of phase competition. While the origin of differing scattering in $\text{Ce}_2\text{Sn}_2\text{O}_7$ remains unclear, it has the potential to uncover phase boundary tuning, or perhaps even disorder, mechanisms. This work shows the versatile playground of exotic magnetism that can be found through the exploration of rare-earth geometrically frustrated magnets.

Bibliography

- [1] H. Yan, O. Benton, L. Jaubert, and N. Shannon, *Phys. Rev. B* **95**, 094422 (2017).
- [2] A. M. Hallas, J. Gaudet, and B. D. Gaulin, *Annu. Rev. Condens. Matter Phys.* **9**, 105 (2018).
- [3] E. M. Smith, O. Benton, D. R. Yahne, B. Placke, J. Gaudet, J. Dudemaine, A. Fitterman, J. Beare, S. Bhattacharya, T. DeLazzer, et al., pp. 1–17 (2021), 2108.01217.
- [4] O. Benton, *Phys. Rev. B* **102**, 104408 (2020).
- [5] *Physical Property Measurement System Dilution Refrigerator User's Manual*, Quantum Design, San Diego, CA, 6th ed. (2013).
- [6] C. Kittel, *Introduction to Solid State Physics* (John Wiley & Sons, New York, NY, 2005), 8th ed.
- [7] *Magnetic Property Measurement System MPMS3 User's Manual*, Quantum Design, San Diego, CA, 15th ed. (2016).
- [8] V. F. Sears, *Neutron News* **3**, 26 (1992).
- [9] H. Moeini and S. A. Hosseini, *Radiat. Phys. Chem.* **177**, 109092 (2020).
- [10] H. Schober, *Neutron scattering instrumentation* (Springer, 2009), pp. 37–104.
- [11] T. Proffen, S. J. Billinge, T. Egami, and D. Louca, *Z. Krystallog.* **218**, 132 (2003).
- [12] S. E. Palmer and J. T. Chalker, *Phys. Rev. B* **62**, 488 (2000).
- [13] A. Poole, A. S. Wills, and E. Lelièvre-Berna, *J. Phys. Condens. Matter* **19**, 452201 (2007).
- [14] L. Savary, K. A. Ross, B. D. Gaulin, J. P. C. Ruff, and L. Balents, *Phys. Rev. Lett.* **109**, 167201 (2012).

- [15] M. Shirai, R. S. Freitas, J. Lago, S. T. Bramwell, C. Ritter, and I. Živković, *Phys. Rev. B* **96**, 180411(R) (2017).
- [16] S. Petit, E. Lhotel, F. Damay, P. Boutrouille, A. Forget, and D. Colson, *Phys. Rev. Lett.* **119**, 187202 (2017).
- [17] D. Olds, C. N. Saunders, M. Peters, T. Proffen, J. Neufeind, and K. Page, *Acta Crystallogr. A* **74**, 293 (2018).
- [18] R. Sibille, N. Gauthier, E. Lhotel, V. Porée, V. Pomjakushin, R. A. Ewings, T. G. Perring, A. Wildes, D. A. Keen, G. J. Nilsen, et al., *Nat. Phys.* **16**, 546 (2019).
- [19] M. Hutchings, *Point-Charge Calculations of Energy Levels of Magnetic Ions in Crystalline Electric Fields* (Academic Press, 1964), vol. 16, pp. 227–273.
- [20] K. W. H. Stevens, *Proc. Phys. Soc. A* **65**, 209 (1952).
- [21] A. Scheie, *J. Appl. Cryst.* **54**, 356 (2021).
- [22] Z. Dun, X. Bai, M. B. Stone, H. Zhou, and M. Mourigal, *Phys. Rev. Res.* **3**, 023012 (2021).
- [23] K. Lea, M. Leask, and W. Wolf, *J. Phys. Chem. Solids* **23**, 1381 (1962).
- [24] U. Walter, *J. Phys. Chem. Solids* **45**, 401 (1984).
- [25] E. Bauer and M. Rotter, *Magnetism of Complex Metallic Alloys: Crystalline Electric Field Effects* (World Scientific, 2010), pp. 183–248.
- [26] J. S. Gardner, M. J. P. Gingras, and J. E. Greedan, *Rev. Mod. Phys.* **82**, 53 (2010).
- [27] M. A. Subramanian and A. W. Sleight, *Handbook on the Physics and Chemistry of Rare Earths* (Elsevier Science, 1993).
- [28] L. D. Sanjeeva, K. A. Ross, C. L. Sarkis, H. S. Nair, C. D. McMillen, and J. W. Kolis, *Inorg. Chem.* **57**, 12456 (2018).

- [29] C. Wiebe and A. Hallas, *APL Mater.* **3**, 041519 (2015).
- [30] R. Shannon and A. Sleight, *Inorg. Chem.* **7**, 1649 (1968).
- [31] M. Antlauf, T. Taniguchi, J. Wagler, M. R. Schwarz, and E. Kroke, *Cryst. Growth Des.* **19**, 5538 (2019).
- [32] U. Becker and J. Felsche, *J. Less Common Met.* **128**, 269 (1987).
- [33] J. G. Rau and M. J. Gingras, *Annu. Rev. Condens. Matter Phys.* **10**, 357 (2019).
- [34] Y.-P. Huang, G. Chen, and M. Hermele, *Phys. Rev. Lett.* **112**, 167203 (2014).
- [35] S. Lee, S. Onoda, and L. Balents, *Phys. Rev. B* **86**, 104412 (2012).
- [36] S. H. Curnoe, *Phys. Rev. B* **75**, 212404 (2007).
- [37] K. A. Ross, L. Savary, B. D. Gaulin, and L. Balents, *Phys. Rev. X* **1**, 021002 (2011).
- [38] S. Guitteny, S. Petit, E. Lhotel, J. Robert, P. Bonville, A. Forget, and I. Mirebeau, *Phys. Rev. B* **88**, 134408 (2013).
- [39] P. Sarte, H. Silverstein, B. Van Wyk, J. Gardner, Y. Qiu, H. Zhou, and C. Wiebe, *J. Phys. Condens. Matter* **23**, 382201 (2011).
- [40] J. Lago, T. Lancaster, S. Blundell, S. Bramwell, F. Pratt, M. Shirai, and C. Baines, *J. Phys. Condens. Matter* **17**, 979 (2005).
- [41] M. Enjalran and M. J. Gingras (2003), 0307152.
- [42] J. Gaudet, E. M. Smith, J. Dudemaine, J. Beare, C. R. C. Buhariwalla, N. P. Butch, M. B. Stone, A. I. Kolesnikov, G. Xu, D. R. Yahne, et al., *Phys. Rev. Lett.* **122**, 1 (2019).
- [43] H. Otake, A. Nakamura, T. Yamashita, and K. Minato, *J. Phys. Chem. Solids* **66**, 329 (2005).
- [44] B. Tolla, A. Demourgues, M. Pouchard, L. Rabardel, L. Fournès, and A. Wattiaux, *C. R. Acad. Sci. Ser. IIC* **2**, 139 (1999).

- [45] R. Sibille, E. Lhotel, V. Pomjakushin, C. Baines, T. Fennell, and M. Kenzelmann, *Phys. Rev. Lett.* **115**, 097202 (2015).
- [46] B. Gao, T. Chen, D. W. Tam, C.-L. Huang, K. Sasmal, D. T. Adroja, F. Ye, H. Cao, G. Sala, M. B. Stone, et al., *Nat. Phys.* **15**, 1052 (2019).
- [47] P. W. Anderson, *Mater. Res. Bull.* **8**, 153 (1973).
- [48] W. J. Hu, S. S. Gong, W. Zhu, and D. N. Sheng, *Phys. Rev. B* **92**, 140403(R) (2015).
- [49] J. A. Paddison, M. Daum, Z. Dun, G. Ehlers, Y. Liu, M. B. Stone, H. Zhou, and M. Mourigal, *Nat. Phys.* **13**, 117 (2017).
- [50] Y. Li, H. Liao, Z. Zhang, S. Li, F. Jin, L. Ling, L. Zhang, Y. Zou, L. Pi, Z. Yang, et al., *Sci. Rep.* **5**, 1 (2015).
- [51] Y. Shen, Y. D. Li, H. Wo, Y. Li, S. Shen, B. Pan, Q. Wang, H. C. Walker, P. Steffens, M. Boehm, et al., *Nature* **540**, 559 (2016).
- [52] Z. Zhu, P. A. Maksimov, S. R. White, and A. L. Chernyshev, *Phys. Rev. Lett.* **119**, 157201 (2017).
- [53] M. M. Bordelon, C. Liu, L. Posthuma, E. Kenney, M. Graf, N. P. Butch, A. Banerjee, S. Calder, L. Balents, and S. D. Wilson, *Phys. Rev. B* **103**, 014420 (2021).
- [54] M. M. Bordelon, J. D. Bocarsly, L. Posthuma, A. Banerjee, Q. Zhang, and S. D. Wilson, *Phys. Rev. B* **103**, 024430 (2021).
- [55] M. M. Bordelon, C. Liu, L. Posthuma, P. M. Sarte, N. P. Butch, D. M. Pajerowski, A. Banerjee, L. Balents, and S. D. Wilson, *Phys. Rev. B* **101**, 224427 (2020).
- [56] M. Bordelon, E. Kenney, C. Liu, T. Hogan, L. Posthuma, M. Kavand, Y. Lyu, M. Sherwin, N. P. Butch, C. Brown, et al., *Nat. Phys.* **15**, 1058 (2019).

- [57] M. M. Bordelon, X. Wang, D. M. Pajerowski, A. Banerjee, M. Sherwin, C. M. Brown, M. Eldeeb, T. Petersen, L. Hozoi, U. Rößler, et al., *Phys. Rev. B* **104**, 094421 (2021).
- [58] A. A. Kulbakov, S. M. Avdoshenko, I. Puente-Orench, M. Deeb, M. Doerr, P. Schlender, T. Doert, and D. S. Inosov, *J. Phys. Condens. Matter* **33**, 425802 (2021).
- [59] M. Eldeeb, T. Petersen, L. Hozoi, V. Yushankhai, and U. Rößler, *Phys. Rev. Mater.* **4**, 124001 (2020).
- [60] W. Liu, Z. Zhang, D. Yan, J. Li, Z. Zhang, J. Ji, F. Jin, Y. Shi, and Q. Zhang (2021), 2108.09693.
- [61] P.-L. Dai, G. Zhang, Y. Xie, C. Duan, Y. Gao, Z. Zhu, E. Feng, Z. Tao, C.-L. Huang, H. Cao, et al., *Phys. Rev. X* **11**, 021044 (2021).
- [62] Z. Zhang, X. Ma, J. Li, G. Wang, D. Adroja, T. Perring, W. Liu, F. Jin, J. Ji, Y. Wang, et al., *Phys. Rev. B* **103**, 035144 (2021).
- [63] Z. Zhang, J. Li, W. Liu, Z. Zhang, J. Ji, F. Jin, R. Chen, J. Wang, X. Wang, J. Ma, et al., *Phys. Rev. B* **103**, 184419 (2021).
- [64] T. Xie, J. Xing, S. Nikitin, S. Nishimoto, M. Brando, P. Khanenko, J. Sichelschmidt, L. Sanjeeva, A. S. Sefat, and A. Podlesnyak (2021), 2106.12451.
- [65] J. Ma, J. Li, Y. H. Gao, C. Liu, Z. Zhang, Z. Wang, R. Chen, J. Embs, E. Feng, F. Zhu, et al. (2020), 2002.09224.
- [66] A. Scheie, V. O. Garlea, L. D. Sanjeeva, J. Xing, and A. S. Sefat, *Phys. Rev. B* **101**, 144432 (2020).
- [67] K. Ranjith, P. Schlender, T. Doert, and M. Baenitz, in *Proceedings of the International Conference on Strongly Correlated Electron Systems (SCES2019)* (2020), p. 011094.
- [68] K. M. Ranjith, S. Luther, T. Reimann, B. Schmidt, P. Schlender, J. Sichelschmidt, H. Yasuoka, A. M. Strydom, Y. Skourski, J. Wosnitza, et al., *Phys. Rev. B* **100**, 224417 (2019).

- [69] Y.-Y. Pai, C. E. Marvinney, L. Liang, J. Xing, A. Scheie, A. A. Puretzky, G. B. Halász, X. Li, R. Juneja, A. S. Sefat, et al. (2021), 2111.03919.
- [70] J. Xing, L. D. Sanjeewa, A. F. May, and A. S. Sefat, *APL Mater.* **9**, 111104 (2021).
- [71] J. Xing, L. D. Sanjeewa, J. Kim, G. Stewart, A. Podlesnyak, and A. S. Sefat, *Phys. Rev. B* **100**, 220407 (2019).
- [72] J. Xing, K. M. Taddei, L. D. Sanjeewa, R. S. Fishman, M. Daum, M. Mourigal, C. dela Cruz, and A. S. Sefat, *Phys. Rev. B* **103**, 144413 (2021).
- [73] G. Bastien, B. Rubrecht, E. Haeussler, P. Schlender, Z. Zangeneh, S. Avdoshenko, R. Sarkar, A. Alfonsov, S. Luther, Y. A. Onykiienko, et al., *SciPost Phys.* **9**, 041 (2020).
- [74] N. W. Ashcroft and N. D. Mermin, *Solid State Physics* (Harcourt College Publishing, Orlando, FL, 1976).
- [75] M. S. Dresselhaus, *Landau Theory of Phase Transitions* (1999), chap. 24.
- [76] *Physical Property Measurement System Heat Capacity Option User's Manual*, Quantum Design, San Diego, CA, 11th ed. (2004).
- [77] A. Scheie, *J. Low Temp. Phys.* **193**, 60 (2018).
- [78] G. L. Squires, *Introduction to the theory of thermal neutron scattering* (Courier Corporation, 1996).
- [79] S. Haravifard, Z. Yamani, and B. D. Gaulin, *Quantum phase transitions* (Elsevier, 2015), vol. 48, chap. 2, pp. 43–144.
- [80] R. Pynn, *Los Alamos Science* **19**, 1 (1990).
- [81] I. A. Zaliznyak and S.-H. Lee, in *Spin* (2005), vol. 5.
- [82] G. Kostorz and S. Lovesey, in *Neutron Scattering* (Elsevier, 1979), vol. 15 of *Treatise on Materials Science Technology*, pp. 1–67.

- [83] T. Chatterji, *Magnetic neutron scattering* (Elsevier, 2006).
- [84] R. M. White, *Quantum Theory of Magnetism* (Springer, 2007).
- [85] R. E. Newham, *Properties of Materials: Anisotropy, Symmetry, Structure* (Oxford University Press, New York, NY, 2005).
- [86] V. O. Garlea and B. C. Chakoumakos, *Magnetic Structures* (Elsevier, 2015), vol. 48, chap. 4, pp. 203–290.
- [87] B. Souvignier, *IUCr A*, **2** (2016).
- [88] A. S. Wills, *Appl. Phys. A: Mater. Sci. Process.* **74** (2002).
- [89] A. Wills, *J. Phys. IV France* **11**, 133 (2001).
- [90] E. F. Bertaut, *Acta Crystallogr. A* **24**, 217 (1968).
- [91] M. I. Aroyo, J. M. Perez-Mato, D. Orobengoa, E. Tasci, G. de la Flor, and A. Kirov, *Bulg. Chem. Commun.* **43**, 183 (2011).
- [92] M. I. Aroyo, J. M. Perez-Mato, C. Capillas, E. Kroumova, S. Ivantchev, G. Madariaga, A. Kirov, and H. Wondratschek, *Z. Kristallogr. Cryst. Mater.* **221**, 15 (2006).
- [93] M. I. Aroyo, A. Kirov, C. Capillas, J. M. Perez-Mato, and H. Wondratschek, *Acta Crystallogr. A* **62**, 115 (2006).
- [94] J. Perez-Mato, S. Gallego, E. Tasci, L. Elcoro, G. de la Flor, and M. Aroyo, *Annu. Rev. Mater. Res.* **45**, 217 (2015).
- [95] A. S. Wills, *Physica B* **276-278**, 680 (2000).
- [96] G. H. Wannier, *Phys. Rev.* **79**, 357 (1950).
- [97] B. Bernu, C. Lhuillier, and L. Pierre, *Phys. Rev. Lett.* **69**, 2590 (1992).

- [98] L. Capriotti, A. E. Trumper, and S. Sorella, Phys. Rev. Lett. **82**, 3899 (1999).
- [99] S. R. White and A. L. Chernyshev, Phys. Rev. Lett. **99**, 127004 (2007).
- [100] R. Coldea, D. A. Tennant, A. M. Tsvelik, and Z. Tylczynski, Phys. Rev. Lett. **86**, 1335 (2001).
- [101] L. Balents, Nature **464**, 199 (2010).
- [102] J. Iaconis, C. Liu, G. B. Halász, and L. Balents, SciPost Phys. **4**, 003 (2018).
- [103] Z. Zhu, P. A. Maksimov, S. R. White, and A. L. Chernyshev, Phys. Rev. Lett. **120**, 207203 (2018).
- [104] R. Zhong, S. Guo, G. Xu, Z. Xu, and R. J. Cava, Proc. Natl. Acad. Sci. **116**, 14505 (2019).
- [105] A. Abragam and B. Bleaney, *Electron paramagnetic resonance of transition ions* (Oxford University Press, 1970).
- [106] S. Onoda and Y. Tanaka, Phys. Rev. B **83**, 094411 (2011).
- [107] S. Petit, E. Lhotel, S. Guitteny, O. Florea, J. Robert, P. Bonville, I. Mirebeau, J. Ollivier, H. Mutka, E. Ressouche, et al., Phys. Rev. B **94**, 165153 (2016).
- [108] E. Lhotel, S. Petit, S. Guitteny, O. Florea, M. Ciomaga Hatnean, C. Colin, E. Ressouche, M. R. Lees, and G. Balakrishnan, Phys. Rev. Lett. **115**, 197202 (2015).
- [109] Y.-D. Li, X. Wang, and G. Chen, Phys. Rev. B **94**, 201114(R) (2016).
- [110] Y.-D. Li and G. Chen, Phys. Rev. B **95**, 041106 (2017).
- [111] R. Applegate, N. R. Hayre, R. R. P. Singh, T. Lin, A. G. R. Day, and M. J. P. Gingras, Phys. Rev. Lett. **109**, 097205 (2012).
- [112] N. R. Hayre, K. A. Ross, R. Applegate, T. Lin, R. R. P. Singh, B. D. Gaulin, and M. J. P. Gingras, Phys. Rev. B **87**, 184423 (2013).

- [113] A. Scheie, J. Kindervater, S. Säubert, C. Duvinage, C. Pfeleiderer, H. J. Changlani, S. Zhang, L. Harriger, K. Arpino, S. M. Koochpayeh, et al., *Phys. Rev. Lett.* **119**, 127201 (2017).
- [114] L. J. Chang, S. Onoda, Y. Su, Y. J. Kao, K. D. Tsuei, Y. Yasui, K. Kakurai, and M. R. Lees, *Nat. Comm.* **3**, 992 (2012).
- [115] E. Lhotel, S. R. Giblin, M. R. Lees, G. Balakrishnan, L. J. Chang, and Y. Yasui, *Phys. Rev. B* **89**, 224419 (2014).
- [116] J. Gaudet, K. A. Ross, E. Kermarrec, N. P. Butch, G. Ehlers, H. A. Dabkowska, and B. D. Gaulin, *Phys. Rev. B* **93**, 064406 (2016).
- [117] J. Robert, E. Lhotel, G. Remenyi, S. Sahling, I. Mirebeau, C. Decorse, B. Canals, and S. Petit, *Phys. Rev. B* **92**, 064425 (2015).
- [118] J. D. Thompson, P. A. McClarty, D. Prabhakaran, I. Cabrera, T. Guidi, and R. Coldea, *Phys. Rev. Lett.* **119**, 057203 (2017).
- [119] J. G. Rau, R. Moessner, and P. A. McClarty, *Phys. Rev. B* **100**, 104423 (2019).
- [120] Y.-D. Li, Y.-M. Lu, and G. Chen, *Phys. Rev. B* **96**, 054445 (2017).
- [121] I. Kimchi, A. Nahum, and T. Senthil, *Phys. Rev. X* **8**, 031028 (2018).
- [122] W. Steinhardt, Z. Shi, A. Samarakoon, S. Dissanayake, D. Graf, Y. Liu, W. Zhu, C. Marjerrison, C. D. Batista, and S. Haravifard, *Phys. Rev. Res.* **3**, 033050 (2021).
- [123] M. E. Zhitomirsky, M. V. Gvozdikova, P. C. W. Holdsworth, and R. Moessner, *Phys. Rev. Lett.* **109**, 077204 (2012).
- [124] K. A. Ross, Y. Qiu, J. R. D. Copley, H. A. Dabkowska, and B. D. Gaulin, *Phys. Rev. Lett.* **112**, 057201 (2014).
- [125] X. Li, W. M. Li, K. Matsubayashi, Y. Sato, C. Q. Jin, Y. Uwatoko, T. Kawae, A. M. Hallas, C. R. Wiebe, A. M. Arevalo-Lopez, et al., *Phys. Rev. B* **89**, 064409 (2014).

- [126] Z. L. Dun, X. Li, R. S. Freitas, E. Arrighi, C. R. Dela Cruz, M. Lee, E. S. Choi, H. B. Cao, H. J. Silverstein, C. R. Wiebe, et al., *Phys. Rev. B* **92**, 140407 (2015).
- [127] Y. Q. Cai, Q. Cui, X. Li, Z. L. Dun, J. Ma, C. dela Cruz, Y. Y. Jiao, J. Liao, P. J. Sun, Y. Q. Li, et al., *Phys. Rev. B* **93**, 014443 (2016).
- [128] J. G. Rau, S. Petit, and M. J. P. Gingras, *Phys. Rev. B* **93**, 184408 (2016).
- [129] A. M. Hallas, J. Gaudet, N. P. Butch, G. Xu, M. Tachibana, C. R. Wiebe, G. M. Luke, and B. D. Gaulin, *Phys. Rev. Lett.* **119**, 187201 (2017).
- [130] Y. Cai, C. Lygouras, G. Thomas, M. N. Wilson, J. Beare, S. Sharma, C. A. Marjerrison, D. R. Yahne, K. A. Ross, Z. Gong, et al., *Phys. Rev. B* **101**, 094432 (2020).
- [131] Y. Cai, M. N. Wilson, J. Beare, C. Lygouras, G. Thomas, D. R. Yahne, K. Ross, K. M. Taddei, G. Sala, H. A. Dabkowska, et al., *Phys. Rev. B* **100**, 184415 (2019).
- [132] S. V. Ushakov, A. Navrotsky, J. M. Farmer, and L. A. Boatner, *J. Mater. Res.* **19** (2004).
- [133] I. Szczygieł, A. Matraszek, and T. Znamierowska, *J. Therm. Anal. Cal.* **93**, 671 (2008).
- [134] M. M. Kimani, L. Thompson, W. Snider, C. D. McMillen, and J. W. Kolis, *Inorg. Chem.* **51**, 13271 (2012).
- [135] G. M. Sheldrick, *Acta Crystallogr. Sect. C Cryst. Struct. Commun.* pp. 3–8 (2015).
- [136] *Magnetic Properties of Layered Transition Metal Compounds*, vol. 9 (Springer Netherlands, 1990).
- [137] D. H. Ryan and I. P. Swainson, *J. Appl. Cryst.* **42**, 43 (2009).
- [138] J. Rodríguez-Carvajal, *Physica B* **192**, 55 (1993).
- [139] B. E. Warren, *Phys. Rev.* **59**, 693 (1941).
- [140] J. Pappis and S. L. Blum, *J. Am. Ceram. Soc.* **44**, 592 (1961).

- [141] H. Shi, J. N. Reimers, and J. R. Dahn, *J. Appl. Crystallogr.* **26**, 827 (1993).
- [142] H. Fujimoto, *Carbon* **41**, 1585 (2003).
- [143] V. O. Garlea, A. T. Savici, and R. Jin, *Phys. Rev. B* **83**, 172407 (2011).
- [144] V. O. Garlea, M. A. McGuire, L. D. Sanjeeva, D. M. Pajerowski, F. Ye, and J. W. Kolis, *AIP Adv.* **8**, 1 (2018).
- [145] A. S. Wills and A. Harrison, *Phys. Rev. B* **61**, 6156 (2000).
- [146] R. T. Azuah, L. R. Kneller, Y. Qiu, P. L. W. Tregenna-Piggott, C. M. Brown, J. R. D. Copley, and R. M. Dimeo, *J. Res. Natl. Inst. Stan. Technol.* **114**, 341 (2009).
- [147] M. J. P. Gingras and P. A. McClarty, *Rep. Prog. Phys.* **77**, 056501 (2014).
- [148] L. Savary and L. Balents, *Rep. Prog. Phys.* **80**, 016502 (2017).
- [149] M. Hermanns, I. Kimchi, and J. Knolle, *Annu. Rev. Condens. Matter Phys.* **9**, 17 (2018).
- [150] J. Knolle and R. Moessner, *Annu. Rev. Condens. Matter Phys.* **10**, 451 (2019).
- [151] M. V. Gvozdikova, P.-E. Melchy, and M. E. Zhitomirsky, *J. Phys. Condens. Matter* **23**, 164209 (2011).
- [152] R. Rawl, M. Lee, E. S. Choi, G. Li, K. W. Chen, R. Baumbach, C. R. dela Cruz, J. Ma, and H. D. Zhou, *Phys. Rev. B* **95**, 174438 (2017).
- [153] S. Säubert, A. Scheie, C. Duvinage, J. Kindervater, S. Zhang, H. J. Changlani, G. Xu, S. M. Koohpayeh, O. Tchernyshyov, C. L. Broholm, et al., *Phys. Rev. B* **101**, 174434 (2020).
- [154] O. A. Petrenko, M. R. Lees, G. Balakrishnan, and D. M. Paul, *Phys. Rev. B* **70**, 012402 (2004).
- [155] L. Seabra, T. Momoi, P. Sindzingre, and N. Shannon, *Phys. Rev. B* **84**, 214418 (2011).
- [156] L. Seabra, P. Sindzingre, T. Momoi, and N. Shannon, *Phys. Rev. B* **93**, 085132 (2016).

- [157] M. Li, I. Rousochatzakis, and N. B. Perkins, Phys. Rev. Res. **2**, 033328 (2020).
- [158] A. Rousseau, J.-M. Parent, and J. A. Quilliam, Phys. Rev. B **96**, 060411 (2017).
- [159] M. J. P. Gingras and E. S. Sørensen, Phys. Rev. B **57**, 10264 (1998).
- [160] H. T. Diep, *Magnetic Systems with Competing Interactions: Frustrated Spin Systems* (World Scientific Publishing, 1994).
- [161] C. A. Vause and J. S. Walker, Sci. Am. **256**, 98 (1987).
- [162] C. A. Vause and J. S. Walker, Phys. Lett. A **90**, 419 (1982).
- [163] C. L. Dias, T. Ala-Nissila, J. Wong-ekkabut, I. Vattulainen, M. Grant, and M. Karttunen, Cryobiology **60**, 91 (2010).
- [164] S. Singh, Phase Transit. **72**, 183 (2000).
- [165] A. N. Berker and J. S. Walker, Phys. Rev. Lett. **47**, 1469 (1981).
- [166] I. V. Lebedeva and A. M. Popov, Phys. Rev. Lett. **124**, 116101 (2020).
- [167] T. H. Lin, X. Y. Shao, M. K. Wu, P. H. Hor, X. C. Jin, C. W. Chu, N. Evans, and R. Bayuzick, Phys. Rev. B **29**, 1493 (1984).
- [168] A. Mendoza-Coto, L. Nicolao, and R. Díaz-Méndez, Sci. Rep. **9**, 2020 (2019).
- [169] A. Mendoza-Coto, D. E. B. de Oliveira, L. Nicolao, and R. Díaz-Méndez, Phys. Rev. B **101**, 174438 (2020).
- [170] N. Altamirano, D. Kubizňák, and R. B. Mann, Phys. Rev. D **88**, 101502 (2013).
- [171] B. Schmidt and P. Thalmeier, Phys. Rev. B **96**, 214443 (2017).
- [172] M. Skoulatos, F. Rucker, G. J. Nilsen, A. Bertin, E. Pomjakushina, J. Ollivier, A. Schneidewind, R. Georgii, O. Zaharko, L. Keller, et al., Phys. Rev. B **100**, 014405 (2019).

- [173] V. Vaks, A. Larkin, and Y. N. Ovchinnikov, *Sov. Phys. JETP* **22**, 820 (1966).
- [174] P. Azaria, H. T. Diep, and H. Giacomini, *Phys. Rev. Lett.* **59**, 1629 (1987).
- [175] E. H. Boubcheur, R. Quartu, H. T. Diep, and O. Nagai, *Phys. Rev. B* **58**, 400 (1998).
- [176] M. Powell, L. D. Sanjeeva, C. D. McMillen, K. A. Ross, C. L. Sarkis, and J. W. Kolis, *Cryst. Growth Des.* **19**, 4920 (2019).
- [177] See Supplemental Materials for additional technical details and which also includes Refs. [186, 187, 188].
- [178] J. D. M. Champion, M. J. Harris, P. C. W. Holdsworth, A. S. Wills, G. Balakrishnan, S. T. Bramwell, E. Čížmár, T. Fennell, J. S. Gardner, J. Lago, et al., *Phys. Rev. B* **68**, 020401 (2003).
- [179] J. Oitmaa, R. R. P. Singh, B. Javanparast, A. G. R. Day, B. V. Bagheri, and M. J. P. Gingras, *Phys. Rev. B* **88**, 220404 (2013).
- [180] V. S. Maryasin, M. E. Zhitomirsky, and R. Moessner, *Phys. Rev. B* **93**, 100406 (2016).
- [181] S. Miyashita, *Proc. Jpn. Acad., Ser. B* **86**, 643 (2010).
- [182] A. Sera, Y. Kousaka, J. Akimitsu, M. Sera, T. Kawamata, Y. Koike, and K. Inoue, *Phys. Rev. B* **94**, 214408 (2016).
- [183] U. F. P. Seifert and M. Vojta, *Phys. Rev. B* **99**, 155156 (2019).
- [184] M. G. Gonzalez, F. T. Lisandrini, G. G. Blesio, A. E. Trumper, C. J. Gazza, and L. O. Manuel, *Phys. Rev. Lett.* **122**, 017201 (2019).
- [185] Y. Yang, S.-J. Ran, X. Chen, Z.-Z. Sun, S.-S. Gong, Z. Wang, and G. Su, *Phys. Rev. B* **101**, 045133 (2020).
- [186] J. N. Reimers, A. J. Berlinsky, and A.-C. Shi, *Phys. Rev. B* **43**, 865 (1991).
- [187] M. Enjalran and M. J. P. Gingras, *Phys. Rev. B* **70**, 174426 (2004).

- [188] M. Enjalran, A. Del Maestro, and M. J. P. Gingras, *unpublished* (2012).
- [189] P. P. Ewald, *Ann. Phys. (Leipzig)* **64**, 253 (1921).
- [190] S. Toth and B. Lake, *J. Phys. Condens. Matter* **27**, 166002 (2015).
- [191] A. Scheie, J. Kindervater, S. Zhang, H. J. Changlani, G. Sala, G. Ehlers, A. Heinemann, G. S. Tucker, S. M. Koochpayeh, and C. Broholm, *Proc. Natl. Acad. Sci.* **117**, 27245 (2020).
- [192] L. D. C. Jaubert, O. Benton, J. G. Rau, J. Oitmaa, R. R. P. Singh, N. Shannon, and M. J. P. Gingras, *Phys. Rev. Lett.* **115**, 267208 (2015).
- [193] C. L. Sarkis, J. G. Rau, L. D. Sanjeeva, M. Powell, J. Kolis, J. Marbey, S. Hill, J. A. Rodriguez-Rivera, H. S. Nair, D. R. Yahne, et al., *Phys. Rev. B* **102**, 134418 (2020).
- [194] S. Lovesey and G. van der Laan, *Phys. Rev. B* **101**, 144419 (2020).
- [195] K. E. Arpino, B. A. Trump, A. O. Scheie, T. M. McQueen, and S. M. Koochpayeh, *Phys. Rev. B* **95**, 094407 (2017).
- [196] R. M. D’Ortenzio, H. A. Dabkowska, S. R. Dunsiger, B. D. Gaulin, M. J. P. Gingras, T. Goko, J. B. Kycia, L. Liu, T. Medina, T. J. Munsie, et al., *Phys. Rev. B* **88**, 134428 (2013).
- [197] A. Yaouanc, P. Dalmas de Réotier, C. Marin, and V. Glazkov, *Phys. Rev. B* **84**, 172408 (2011).
- [198] A. Mostaed, G. Balakrishnan, M. R. Lees, Y. Yasui, L.-J. Chang, and R. Beanland, *Phys. Rev. B* **95**, 094431 (2017).
- [199] Z. Shafieizadeh, Y. Xin, S. M. Koochpayeh, Q. Huang, and H. Zhou, *Sci. Rep.* **8**, 1 (2018).
- [200] C. L. Farrow, P. Juhas, J. W. Liu, D. Bryndin, E. S. Božin, J. Bloch, T. Proffen, and S. J. L. Billinge, *J. Phys. Condens. Matter* **19**, 335219 (2007).
- [201] P. Juhás, J. N. Louwen, L. van Eijck, E. T. C. Vogt, and S. J. L. Billinge, *J. Appl. Crystallogr.* **51**, 1492 (2018).
- [202] J. A. Paddison, J. Ross Stewart, and A. L. Goodwin, *J. Phys. Condens. Matter* **25**, 1 (2013).